Mars' Energetic Plume Ion Escape Channel

by

Blake C. Johnson

A dissertation submitted in partial fulfillment
of the requirements for the degree of
Doctor of Philosophy
(Atmospheric, Oceanic and Space Sciences)
in the University of Michigan
2018

Doctoral Committee:

Professor Michael W. Liemohn, Chair
Research Professor Stephen W. Bougher
Professor Brian E. Gilchrist
Associate Professor Xianzhe Jia
Assistant Research Scientist Jim M. Raines
Associate Research Scientist Valeriy Tenishev

The Song of life

Once lush and vibrant
Tears flowed from leaden skies
Lines etched deep with time
Shaping ghostly forms
Now barren and dry

Mars
Alone in the sea of space
A world of desolation
Silent and forgotten
Sleeping in ice

Winds whisper silently
Singing the song of life
A tune forged in death
Mournful with remembrance
“Water”
“Water”

-Shawn D. Standfast

Blake C. Johnson

blakecjo@umich.edu

ORCID iD: 0000-0003-3056-8601

Dedication

This dissertation is dedicated to Annareli Morales and Michael Liemohn, whose supportive presence meant that I always had somebody to talk to when I had a problem**.**

Acknowledgements

The author thanks NASA and NSF for supporting this work, particularly under NASA grants NNX11AD80G, NNX13AG26G, and NNX14AH19G, and NSF grant AST-0908311. The ion data is available at the ASPERA-3 website at the Swedish Institute for Space Physics, http://aspera-3.irf.se/thedata, and has been processed using the CCATi software package written in IDL by Markus Fraenz and others. The original draping proxy developed by Dave Brain, as well as the proxies used for subsolar magnetic field strength and for EUV flux, are all available at http://sprg.ssl.berkeley.edu/~brain/proxies.html.

Table of Contents

Abstract

Mars is losing its atmosphere. The planet's small size results in relatively low energy requirements for atmospheric particles to escape into deep space, and its lack of a planetary magnetic field allows the solar wind to directly interact with the upper atmosphere, providing an additional source from which particles may obtain this requisite energy. The escape of particles from Mar's atmosphere over the course of billions of years is not only a story of atmospheric evolution; it is a story of the evolution of a global climate. It is now thought that oceans worth of liquid water may have existed on a warmer ancient Mars, and atmospheric escape of hydrogen and oxygen is one explanation of how such an ocean may have vanished. The research presented here revolves around the examination of one particular "loss channel" for oxygen (and other "heavy" ions) from Mars. This loss channel, known as the "energetic plume," consists of pickup ions, electrically charged planetary particles that, finding themselves in the solar wind flow past Mars, are accelerated in the direction of the solar wind's convective electric field (E_{SW}). In the spatially zoomed out view, the acceleration in this direction is just the initial part of the first gyration of an E_{SW}-cross-B drift in the direction of solar wind flow. Zoomed in closer to Mars, where ion-observing satellites have orbited, a result of the huge gyroradius of these pickup ions is that, in addition to having high energies, energetic plume particles have flight directions distinct from other escaping particles and are observed at locations not reached by other escaping particles. This dissertation introduces the Mars space environment and the problem of atmospheric escape generally before presenting the search for this distinct phase space signature

of the energetic plume in ion data from the Mars Express satellite. It was found that despite the presence of obstacles to observing the energetic plume using the Ion Mass Analyzer (IMA) onboard Mars Express, it is possible to both identify unambiguous instances of energetic plume observations in IMA data and to see signatures of the energetic plume in statistical maps of the Mars space environment made using IMA observations. Furthermore, it was found that accounting for "weathervaning" – the subsolarward bending of magnetic field lines draped around the ionosphere – can be used to improve estimates of the direction of E_{SW}. The resulting more accurate estimate for the direction of E_{SW} improves statistical representations of the energetic plume in IMA data, and significant quantities of energetic plume type ions are observed by IMA ~ 60% more frequently in the newly estimated direction of E_{SW} than in the previously estimated direction of E_{SW}. We conclude that the improved method of estimating the direction of E_{SW} should be used in place of previously existing proxies in studies concerning the variation of energetic plume fluxes for different solar conditions during the time period between Jan. 2004 and Oct. 2006.

Chapter 1: Induced magnetospheres

1.1 A conductor, a plasma, and a $\boldsymbol{dB/dt}$

This is a recipe for an induced magnetosphere: Create a large mass. Take special care to ensure both that it is large enough to hold an atmosphere and that it lacks an internal planetary dynamo. Expose your large-mass-with-atmosphere to two things. First embed it in a magnetized plasma flow. Second, subject the atmosphere to ionizing radiation with fluxes high enough to maintain an ionosphere of non-negligible conductance. This is all that is required for the creation of an induced magnetosphere.

This is the simple recipe that gives rise to the wonderful complexity discussed in the present work. Just as planetary magnetospheres created by intrinsic planetary dipole fields – such as Earth's – divert plasma flow around them, carving out a volume of space within which the particle and wave behavior of plasma populations is determined by the dipole magnetic field and its interaction with the surrounding plasma, an "induced magnetosphere" refers to the region of space carved out of a surrounding plasma by magnetic fields. In the case of induced magnetospheres, these fields are not intrinsic to a planet, but are associated with currents induced in a conductor that is in the path of the surrounding plasma flow (see Figure 1.1). As noted in *Luhmann et al*. [2004], this conductor could be a solid planetary surface or an ocean rather than an ionosphere, but here focus will be placed exclusively on induced magnetospheres arising from the interaction of ionospheres with surrounding plasma. Ionospheres are a distinct and arguably

more complex case than a solid conductor or an ocean due to their compressibility and the dynamic nature of the boundary of the conductor itself.

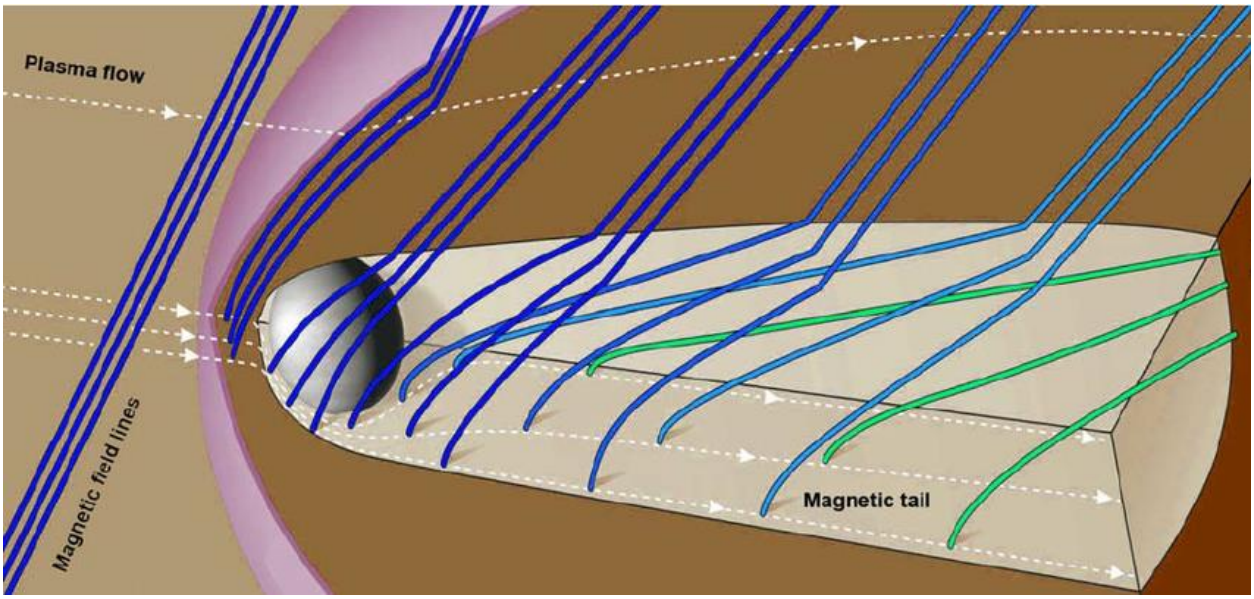

Figure 1.1. This replication of Fig. 1 in *Israelevich and Ershkovich* [2013] shows the configuration of magnetic field lines (blue and green) in an around an induced magnetosphere. The near-white colored region represents the region of space carved out by the induced magnetosphere, in which the plasma environment is dominated the interaction of the conductor with the surround plasma flow.

1.2 Examples of Induced Magnetospheres

Our solar system has provided us with at least four examples of induced magnetospheres: Venus, Mars, Saturn's moon Titan, and comets. Comets are by far the smallest of these celestial objects to have an induced magnetosphere, as they do not have the same requirement of a mass large enough to maintain a stable ionosphere. Near the sun, portions of a comet's icy surface are vaporized, providing a source of charged particles surrounding the comet that can function as an ionosphere of sorts even if these particles are not gravitationally bound (e.g. *Cowan, J. J. and A'Hearn, M. F.*, 1979). Titan's uniqueness arises for other reasons. Titan has a gravitationally bound ionosphere, but whereas the induced magnetospheres of Venus, Mars, and comets exist

within the solar wind, the plasma flow in which Titan is embedded is that of the corotating magnetospheric plasma of Saturn. Only on occasion does Titan's orbit take it outside of Saturn's magnetosphere proper and into the shocked solar wind flow upstream of Saturn (*Ledvina et al.*, 2004). This setting for Titan has the noteworthy feature that the direction of background plasma flow is not always (in fact rarely is) a near-match with the direction from which Titan is hit by the sunlight that produces its ionosphere, the extreme ultraviolet (EUV) part of the spectrum. This is in contrast to the induced magnetospheric systems of Venus and Mars, where the plasma flow is from the same direction as the EUV flux that serves as the primary ionizing agent for their ionospheres. The direction from which the ionizing flux arrives is significant in part because it has long been understood that the density of charged particles in an ionosphere is higher near the source, where ionization occurs (e.g. *Appleton*, 1933). Thus, Titan is a fascinating example of an induced magnetosphere that is pushed on by the pressure of Saturn's magnetospheric plasma sometimes on the dayside where the ionospheric pressure is highest, and sometimes on the nightside, where ionospheric densities and hence plasma pressures are greatly reduced. For detailed discussion of Titan's induced magnetosphere, see for example *Ledvina et. al*. [2004], *Karoly Szego et al.* [2011], and *Ma et al*. [2009].

In this work, particular attention will be given to the Martian system (the primary topic of this dissertation) and to that of Venus, which will repeatedly serve a useful point of comparison. Section 1.3 will describe the system surrounding Venus, with an organizational structure that attempts to begin with the most fundamental processes and progress toward more intricate details. Section 1.4, concerning Mars, has many similarities, and is therefore somewhat shorter. In the discussion on Mars, all repetitions of phenomena already discussed at Venus should be

regarded not as redundancies, but as reminders. As noted by *Karoly Szego et al*. [2011], the fact that the two systems are so similar, despite occupying very different points in parameter space, is worth emphasizing. However, rather than having the discussion on the Mars plasma environment directly mirror the discussion on Venus, the Mars section is designed to allow readers an alternative method of organizing information in a way that may aid retention. It is organized spatially, beginning upstream and progressing toward the magnetotail that extends out behind the planet (away from the sun). For a review of induced magnetospheres more generally, see *Luhmann et al*. [2004].

1.3 Venus' Global Interaction with the Solar Wind

It has been known for a long time that Venus lacks a planetary magnetic field (*Russell*, 1979). In the absence of such a field, it is the ionosphere of Venus that provides an obstacle to the solar wind flow. In their first course on electrodynamics, students are often taught that the magnetic field inside of an ideal conductor will be zero because the free charges on the surface of the conductor arrange themselves into currents that, in the conductor's interior, precisely cancel the external field. Ionospheres with a sufficiently high plasma pressure are no exception to this general rule, with the solar wind's interplanetary magnetic field (IMF) unable to penetrate to altitudes beneath the ionospheric altitudes at which the induced currents flow. As a result, the magnetic obstacle produced by the ionosphere serves as a shield against the background magnetic field itself in addition to the solar wind particles that are diverted around the obstacle. The resulting plasma configuration is depicted in Fig. 1.2. In this image, the IMF upstream of Venus is shown as white Vertical lines. As these field lines come into contact with the induced magnetosphere of Venus, a curvature of the field is seen. This basic shape of an induced

magnetosphere is often described as the background field (the magnetic field of the plasma through which the obstacle moves) draping around the ionosphere rather than penetrating it. This draping can be thought of as the result of the "center" of the magnetic field lines getting caught near the planet while the endpoints of the field line are dragged downstream at solar wind velocity. The physical basis for the idea of the center of these field lines being slowed is conservation of momentum. In a process known as mass-loading, each point along a magnetic flux tube that picks up charged planetary particles will be slowed in agreement with conservation of momentum, causing the portions of a flux tube that most closely approach regions of high ionospheric density to be slowed the most, lagging behind the other portions of the flux tube. Many field lines slip around the "poles" of the planet. Field lines that are convected downward into the collisional atmosphere, on the other hand, where collisions produce some electric resistance, will experience magnetic diffusion, causing the magnetic field to weaken and perhaps eventually disappear altogether, as the currents associated with the maintenance of these fields are obstructed by collisions. It can be noted that if every plasma population within the system were perfectly conducting, no magnetic diffusion would occur at all. Instead, the IMF would be frozen to the solar wind plasma, and all magnetic flux would get past Venus by slipping around the edges of the ionosphere along with the solar wind plasma. The draping of the IMF results in the formation of a two-lobed induced magnetotail in the planet's wake. The length of this tail should be primarily determined by the distance the solar wind moves during the time it takes for field lines to slip past the ionospheric obstacle. Although this "draped" field line description is useful for imprinting a correct three-dimensional image of an induced magnetosphere, a more physical understanding of this curling of the field lines must incorporate Ampere's Law, which relates the curl of a magnetic vector field to the current densities associated with the magnetic

field. In Figure 1.2, the curling of field lines around the ionosphere of Venus correspond largely to currents that are induced in the ionosphere *Luhmann et al.* [2004]. Because the currents associated with this horizontal curved field above the dayside ionosphere are in large part currents carried by planetary ionospheric particles, some scientists object to the practice of referring to these field lines as draped IMF, a practice which can be said to ignore the contribution of the ionosphere and electromagnetic induction. Thus, it is prudent to bear in mind that, as the convenient notion of "draped" interplanetary magnetic field lines is used throughout this dissertation, this terminology is meant to interpreted as a description of the topology of the magnetic field lines (connected to the IMF at both ends) rather than as a description of the currents associated with the local shape of the field line.

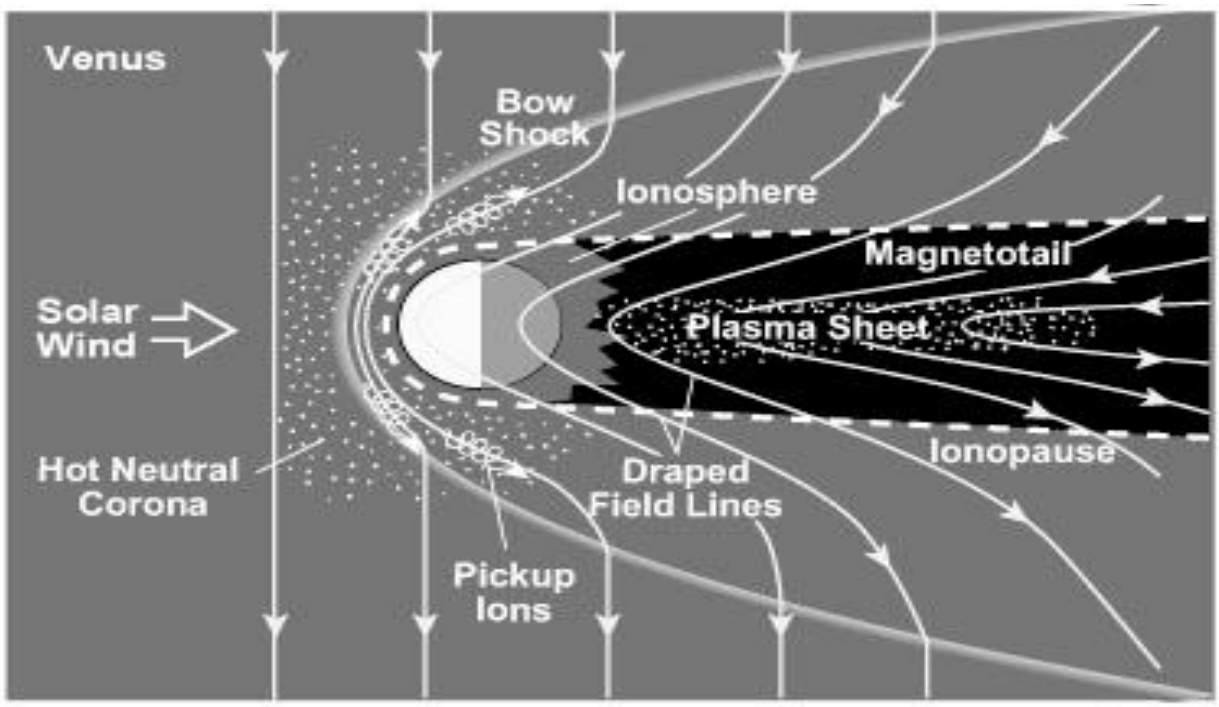

Figure 1.2. The Venus Plasma Environment. Note that this image depicts a purely azimuthal background IMF, whereas in reality the IMF direction at Venus given by the Parker Spiral is more radial from the sun than azimuthal. This image was taken from http://ase.tufts.edu/cosmos/print_images.asp?id=7. Increasing the depicted gyroradius of pickup ions and adding crustal magnetic fields would be sufficient to transform this image into a cartoon of Mars' induced magnetosphere rather than that of Venus.

A review of induced magnetospheres is incomplete without a discussion of the boundaries that separate various plasma regimes. The boundary that separates the solar wind plasma from planetary plasma is well defined at Venus, and has been called the Magnetic Pileup Boundary (MPB), the Induced Magnetosphere Boundary (IMB), the Ion Composition Boundary (ICB), and the Protonopause. The region inside of this boundary, which is dominated by planetary plasma, has been called the Induced Magnetosphere (often referring to everything within the IMB impacted by the solar wind), or the Magnetic Pileup Region (referring to the region of high magnetic field strength inside of the MPB but outside of ionosphere and magnetotail), or the Mantle (used roughly interchangeably with the term Magnetic Pileup Region). From now on this paper will use the term Magnetic Pileup Boundary (MPB) to refer to this boundary. *Bertucci et al*. [2011] summarizes the characteristics of an inward crossing of the MPB of Venus as follows:

- A (sometimes sharp) increase in the magnetic field strength by a factor of 2-3
- Decrease in the magnetic field fluctuations
- Enhancement of the magnetic field draping
- Decrease in the temperature of electrons
- Decrease in the solar wind ion densities

These transitions may not occur at exactly the same place (which is a primary reason for the variety of names for this boundary), but they do occur near enough to each other to allow us to consider them to represent a single boundary or transition region. The other reason for there being a variety of names for this boundary is that the boundary is defined differently depending on context. For example, a data paper based on ion measurements may define the boundary as the point where solar wind protons give way to planetary ions, resulting in the term "ion composition boundary." The authors of a modeling paper, on the other hand, recognizing that the change in ion composition represents a pressure balance between two regimes, may define the boundary to be the point at which the solar wind ram and thermal pressure balance the piled up

magnetic pressure, resulting in the term "magnetic pileup boundary." Whatever we choose to call it, the subsolar location of MPB at Venus is generally around 1.14 Venus radii (R_V) – or 6,900 km – from the center of the planet (*Zhang et al.,* 2008). The decrease in the magnetic field fluctuations and the enhancement of field draping, listed above as two separate effects, are directly linked. When the center of the magnetic field line is caught on the dayside of Venus and begins to lag behind the ends of the field line, which flow with the solar wind, the field line is pulled tight around the ionospheric obstacle. The increase in magnetic tension associated with this increased draping is what prevents large amplitude magnetic field fluctuations.

Two additional boundaries exist in the dayside plasma environment of Venus. Upstream of the MPB is a bow shock that turns the supersonic superalfvenic super-alfvenic solar wind flow (flow that is faster than the speed at which information is transmitted through the fluid) into a shocked flow (slower, hotter, denser according to the Rankine-Huginot jump conditions) that is capable of moving around the obstacle. This region of shocked solar wind between the bow shock and the MPB is called the magnetosheath, and is analogous to the magnetosheaths surrounding the magnetospheres of magnetized planets. Downstream of the MPB the piled up magnetic pressure eventually gives way to the ionospheric pressure. The location at which this occurs will be referred to in this paper as the ionopause. Fig. 1.3 depicts the count rate of electrons, H^+, and O^+ as a function of time as measured by the Aspera 4 instrument suite on board Venus Express (VEX). The times when VEX crossed the bow shock and MPB are labeled as BS and ICB, respectively. For review papers concerning the global plasma environment of Venus, see, for example, *Luhmann*, [1986] or *Donahue and Russell* [1997].

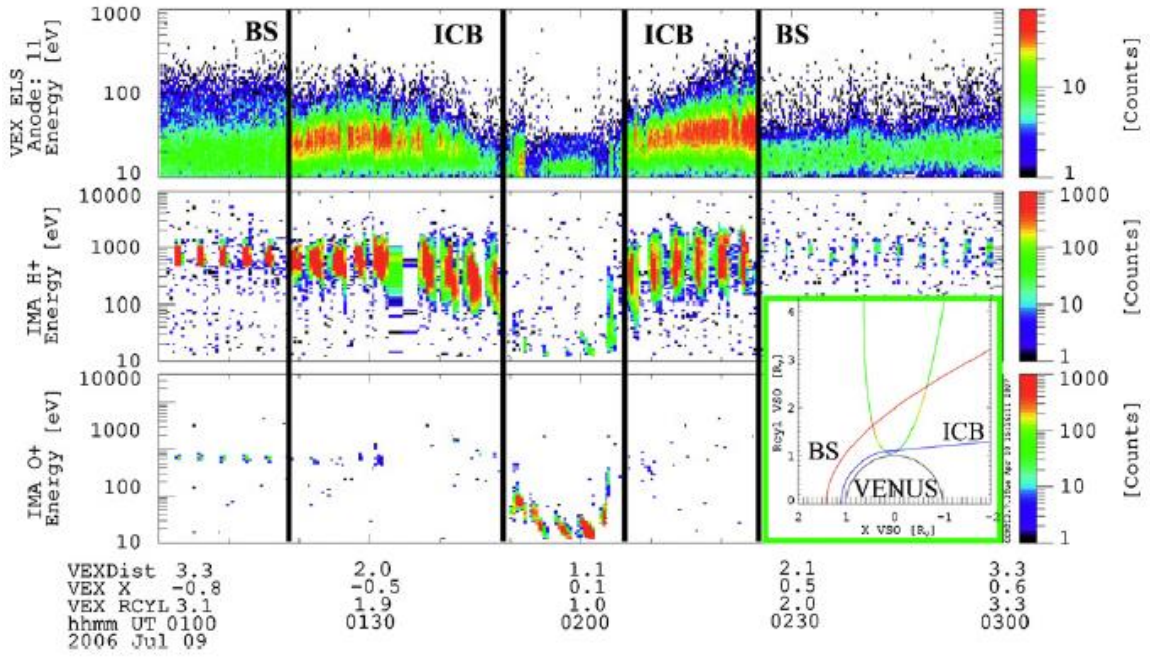

Figure 1.3. Inward and outward crossings of the Bow Shock (BS) and Magnetic Pileup Boundary or Ion Composition Boundary (ICB). Some authors prefer to define an additional boundary, the ionopause, which in this figure would be located on either side of the increased electron density region in the very center of the top panel (the green surrounded by blue). Inset at the bottom right is a plot, in cylindrical coordinates, of the path of the ESA's Venus Express as it took these measurements. This was figure taken from *Martinecz et al*. [2008].

1.4 Mars' Global Interaction with the Solar Wind

After the magnetometer onboard the Phobos-2 spacecraft set upper limits for what a planetary dipole field at Mars must be, it was known that if Mars had a planetary dipole field it must be relatively weak. The arrival of Mars Global Surveyor in near-Mars orbit in the late 1990s further reduced this upper limit to the point of it being vanishingly small (*Acuna et al*., 1998). It was then understood that Mars could be considered to have an induced magnetospheric system. Let's conduct a thought experiment to better understand the Mars induced magnetospheric

environment. Suppose a spacecraft (hopefully equipped with a magnetometer and a full suite of plasma instruments) begins upstream of Mars in the undisturbed solar wind. What should the spacecraft be expected to see as it moves in the antisunward direction toward Mars, then past Mars, and finally down along the magnetotail?

It is likely that the first indications of a disturbance in the solar wind flow will be the appearance of proton cyclotron waves in the magnetometer data. These waves will have a frequency equal to the gyrofrequency of H^+ pickup ions, whose anisotropy (a ring distribution in velocity space) is responsible for the generation of these waves. The presence of these waves implies the presence of the pickup protons, and the presence of the pickup protons implies the presence of a hydrogen exosphere that extends out even beyond the bow shock (*Brain et al.*, 2002). The amplitude of these waves, given by $\frac{\Delta B}{B}$, tends to be higher here at Mars than at Venus because the amplitude is determined in part by the following ratio: the density of pickup H^+ to the solar wind density (*Delva et al*., 2011). The lower density of the solar wind at Mars, together with Mars' smaller mass allowing for a more extended hydrogen exosphere, results in larger amplitude waves.

As the spacecraft continues downstream, it will next encounter the Martian bow shock. In addition to the changes in plasma parameters already noted, the IMF is enhanced on the downstream side of the shock. Specifically, the component of the IMF which is perpendicular the local normal vector of the shock will increase in magnitude while the component of the IMF that is parallel to the shock normal remains unchanged. At the nose of the bow shock, the shock's normal vector is directed nearly radially toward the sun. Assuming the IMF direction is approximated by a Parker Spiral, the angle of the IMF is directed less radially from the sun at greater distances from the sun. It follows that the component of the IMF that is perpendicular to

the normal vector at the nose of the bow shock is larger at greater distances from the sun. Thus, the percentage increase in the magnitude of the magnetic field across the shock can be expected to be greater at Mars than at Venus.

Continuing on past the Martian bow shock, the spacecraft would be located within the magnetosheath for several tenths of a Mars radii (~1000 km) before crossing the MPB. *Bertucci et al*. [2011] summarize the characteristics of an inward crossing of the Martian MPB as follows:

- A sharp increase in the magnetic field strength by a factor of 2-3
- Sharp decrease in the magnetic field fluctuations
- Sharp enhancement of the magnetic field draping
- Decrease in the temperature of electrons
- Increase in the total electron density
- Decrease in the solar wind ion densities

This list is identical to the list characterizing the MPB of Venus with just two exceptions. First, the increase in total electron density observed at Mars has yet to be reported at Venus (although the same feature may exist). Second, the magnetic field changes appear to be more abrupt at Mars than at Venus. Figure 1.4 provides an example of how the magnetic field behaves across these two boundaries at Mars. Figure 1.6 depicts the pressure balances that hold along the Sun-Mars line. The solar wind ram pressure is transformed into solar wind thermal pressure across the bow shock, which then gives way to the magnetic pressure of the draped IMF. This piled up magnetic pressure eventually gives way to ionospheric thermal pressure combined with the pressure of crustal magnetic fields. These crustal fields will be discussed briefly in section four.

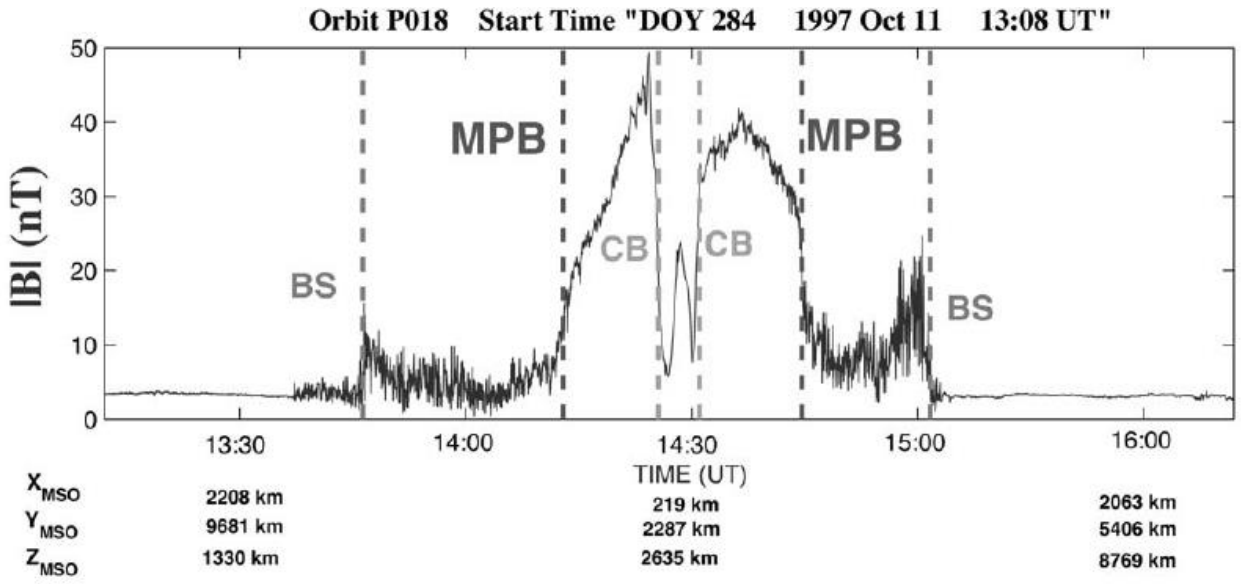

Figure 1.4. Behavior of the magnetic field across the bow shock and MPB of Mars. In addition to the BS and MPB, we see a "cavity boundary" (CB), inside of which the Martian ionospheric pressure prevents the draped IMF from penetrating further. This data was gathered by Mars Global Surveyor's magnetometer. This figure has been taken from *Nagy et al*. [2004].

Let's continue on downstream through the MPB, through the magnetic pileup region, through the limb of the of Mars' atmosphere, and on into the induced magnetotail. The magnetotail is formed by the draped IMF, with one side, or "lobe," containing magnetic field directed toward the planet and the other lobe containing magnetic field directed downstream away from the planet. Separating these regions of oppositely directed field lines is a sheet of current directed cross-tail. Co-located with this current sheet is the plasma sheet that carries the current, a region of increased plasma density composed of ions with a planetary origin. The lobes of the tail surrounding the plasma sheet are of a low density for at least two reasons. First, as the solar wind flow is diverted around Mars, a void is left in the planet's wake. The IMF (and hence the solar wind plasma frozen to these field lines) does not fill in this void until many planetary radii downstream. Second, what few particles do exist in these lobes experience an $E \times B$ drift toward

the plasma sheet. This is analogous to the $E \times B$ drift toward the Earth's plasma sheet in the lobes of the Earth's magnetotail. A key difference is that at Mars the orientation of the electric field, and the orientation of the plasma sheet, is determined by the clock angle of the IMF, which is defined as $\arctan(\frac{B_{IMF_z}}{B_{IMF_y}})$, where B_{IMF_y} is the component of the IMF in the direction opposite the orbital motion of Mars, and B_{IMF_z} is the component of the IMF in the $x \times y$ direction, where the x axis points from Mars toward the sun. When the clock angle of the IMF rotates in the y-z plane, the orientation of the induced magnetosphere rotates as well, after a small lag time. A diagram showing the IMF (B) and the solar wind convective electric field (E) in the plane in which clock angles are defined is provided in Figure 1.5.

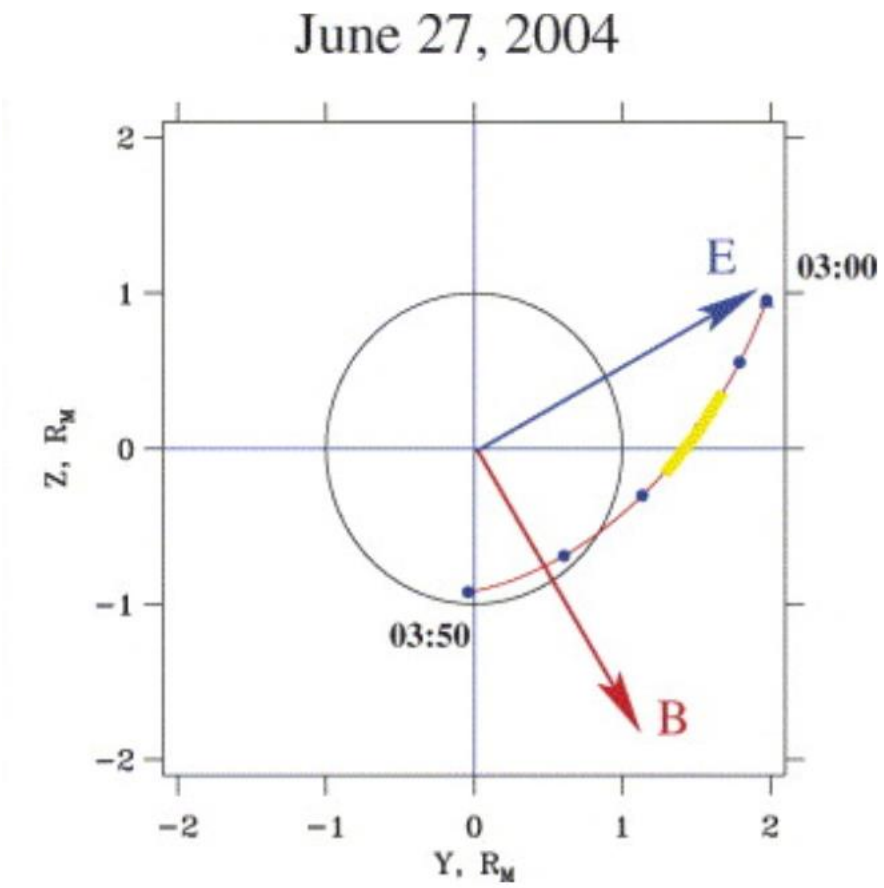

Figure 1.5. Taken from *Fedorov et al*., (2006), this view from the sun shows the y-z plane in which the magnetic field clock angle is defined as $\arctan(\frac{B_{IMF_z}}{B_{IMF_y}})$. As the IMF rotates in this plane, the

Martian current sheet rotates with it, with the plane of the current sheet remaining roughly aligned with the direction of E_{SW} (perpendicular to the plane of the IMF).

A second important difference between the Earth's magnetotail and that of any induced magnetotail arises due to a difference in magnetic connectivity. Whereas particles in the near-Earth plasma sheet, on field lines connected to the planet, experience a JxB force directed back toward the planet, particles in the tail plasma sheet of an induced magnetosphere, where magnetic field lines are most typically connected to downstream IMF, experience a JxB force directed downtail, away from the planet, resulting in less feedback into the inner magnetospheric system than occurs at Earth. For review papers concerning the global plasma environment of Mars, see *Nagy et al*. [2004] or *Bertucci et al*. [2011].

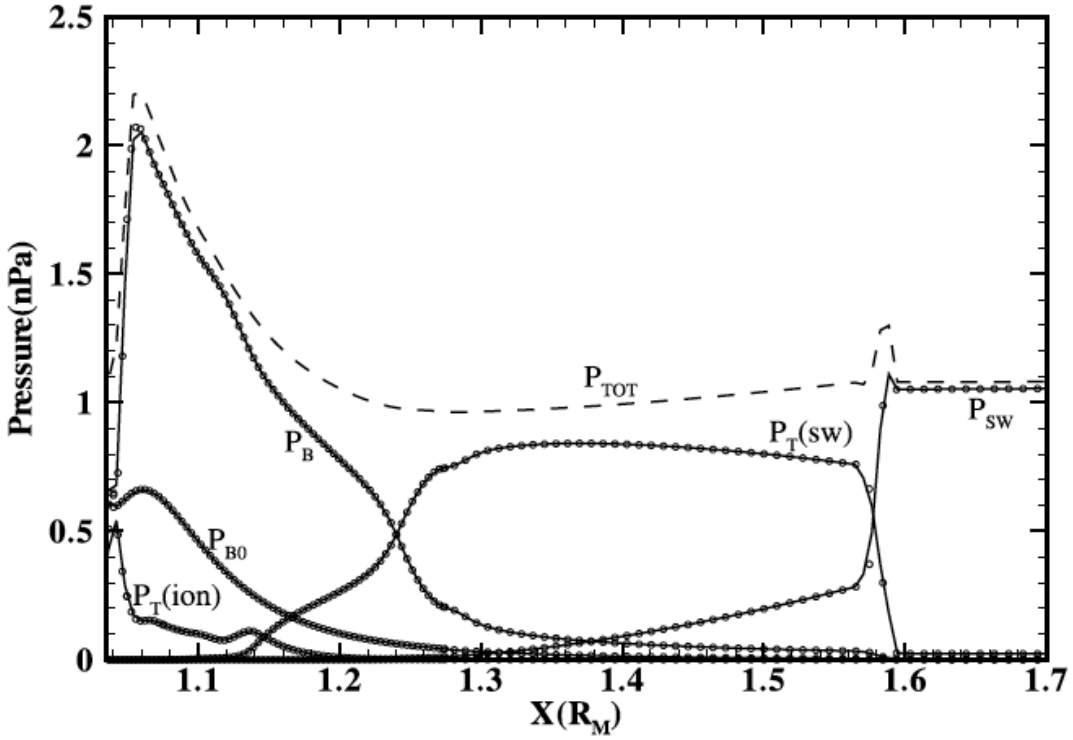

Figure 1.6. Pressure profiles along the Sun-Mars line taken from the multi-species fluid code of *Ma et al.* [2004]. P_{SW} is the solar wind ram pressure. $P_{T(SW)}$ is the solar wind thermal pressure. $P_{T(ion)}$ is the ionospheric thermal pressure. P_{B0} is the magnetic pressure associated with crustal fields. P_B is the total magnetic pressure.

1.5 Magnetic Topologies at Mars

At the end of the previous section, magnetic connectivity was introduced as a means of understanding why the bulk force acting on plasma populations in induced magnetotails (directed downtail) differs from the bulk force acting on the near-Earth plasma sheet (directed Earthward). In addition to its usefulness in helping to understand the direction of cross magnetic field forces and flow, magnetic connectivity is also essential for understanding where observed charged particles that move along field lines can be expected to go and where they might have come from. In short, magnetic topology is crucial for understanding both energy fluxes and particle fluxes.

In addition to the discovery that Mars does not have a significant planetary dipole moment, the arrival of Mars Global Surveyor and its magnetometer at Mars revealed that Mars is home to patches of magnetized rock, or "crustal fields" far stronger than analogous features on the Earth's surface (*Acuna et al.*, 1998). These patchy crustal fields, located predominantly in the southern hemisphere and with the strongest fields at around 180° E longitude, play a role in mediating the interaction of the Martian ionosphere with the incident solar wind, adding a layer of complexity on top of the more "standard" case of an induced magnetosphere seen in Venus. Numerical simulations of Mars' induced magnetosphere have found that inclusion of these

crustal fields can lead to what appears to be a tangled mess of magnetic field lines near the MPB, particularly in the altitude range where draped IMF meets the crustal fields (e.g. *Luhmann et al.*, 2015). This tangled mess also boasts more uncertainty concerning when magnetic reconnection is expected to occur as compared with what is seen at Earth. Whereas dayside reconnection at the Earth's magnetopause is known to occur more rapidly during periods of southward IMF (e.g. *Hoilijoki et al*., 2014), the localized nature of the crustal fields means that different longitudes have different field directions associated with them, yielding a situation in which the rate of reconnection between crustal fields and IMF is expected to vary not only with upstream IMF direction, but also with time of day. Despite these unique complications, it remains possible to group magnetic connectivity at Mars into three fundamental topologies. First, both endpoints of a magnetic field line could be connected to the surface. These are referred to as "closed" field lines. Second, both endpoints may be connected to the solar wind. These are often referred to as "draped" field lines. The third grouping, known as "open" field lines, refers to field lines that are connected to the planet at one end and to the IMF at the other. While it is possible to further distinguish between various topologies in meaningful ways (for example an open field line connected to the upstream bow shock vs. an open field line connected to the downstream flow where no strong shock is present), these three most fundamental categories are useful in helping to determine when and where there is coupling between the solar wind and the ionosphere. Useful explorations of magnetic topologies at induced magnetospheres and the possibilities for reconnection between the various categories of magnetic field lines may be found in *Dubinin et al*. [2013] and *Ulusen et al*. [2016].

One effect of Mars' crustal magnetic fields of particular import for the present work is their mediation of the escape of charged particles from the ionosphere into deep space. It has been found that when the strongest crustal fields are on the dayside of Mars, the rate of ion escape is reduced (e.g. *Fang et al*., 2010; *Brecht and Ledvina*, 2014; *Dong, C. et al*., 2015). There are at least two distinct and complementary means of understanding this effect. One way of explaining this phenomenon is to note that, as is seen Fig. 1.6, moving from one plasma regime to another on the dayside of Mars can be thought of in terms of pressure balances. The magnetic pileup boundary exists where the thermal plasma pressure of the shocked solar wind in the magnetosheath gives way to the "piled up" magnetic field above the dayside ionosphere. Within this framework, the reduction of planetary ion escape when the strongest crustal fields are on the dayside can be thought of simply as the result of the total pressure on the inside of the MPB, now augmented by crustal fields, being stronger and therefore able to stand off the incident solar wind at a higher altitude, thereby reducing the number of atmospheric particles exposed to the solar wind. A second way of explaining the decreased ion escape when the strongest crustal fields are situated on the dayside is a more direct appeal to magnetic connectivity: stronger crustal fields on the dayside means closed loops of magnetic field extending to higher dayside altitudes, thereby reducing the quantity of ionospheric particles connected to the solar wind flow.

Chapter 2: Mars Ion Escape

2.1 Atlantis Inverted

The poem at the beginning of this dissertation is one writer's stylized telling of what amounts to a mystery of global proportions. Fantastic storytellers have for centuries played off of rumors of Atlantis, an entire continent said to have once existed and thrived before being eventually swallowed by the sea. Mars has its own mysterious story of a large-scale disappearance, and though it is lesser known than stories of Atlantis, it is much more solidly grounded in geological fact. At Mars, rather than a once great continent giving way to a great expanse of sea, it is possible that a once great ocean, over the course of billions of years, gave way to the barren landscape that is present-day Mars.

In late 1971, Mariner 9, the first spacecraft to orbit a planet other than Earth, arrived at Mars. Among its observations were images of what appeared to be winding river beds and large outflow patterns consistent with what would be caused by floods (e.g. *McCauley et al.*, 1972; *Baker and Milton*, 1974). Large bodies of water were implicated. Mars' low-lying northern plains were suggested as a basin that may have been home to vast amounts of standing liquid water (e.g. *Lucchitta et al.*, 1986). Locations were identified that exhibited characteristics typically seen where rivers meet oceans (e.g. *Ivanov et al.*, 2001). Such shoreline estimates allow for the estimation of the volume of the basin beneath this shoreline, yielding estimates on the order of 10^7 to 10^8 cubic kilometers of water (e.g. *Carr et al.*, 2003). In 2004, Mars exploration

rover Spirit found hydrated minerals, rocks whose crystal structure is thought to require the presence of liquid water in order to form (e.g. *Squyres et al*., 2004). The orbiter Mars Odyssey carried a Gamma Ray Spectrometer able to detect elemental distributions of potassium in the northern plains that require fractionation "consistent with aqueous activity", providing further support for the idea of large amounts of liquid water flowing into the northern plains (*Dohm et al*., 2009). Repeatedly, shoreline-based estimates for the quantity of water in this possible past ocean were much higher than the amount of water ice estimated to be stored at the poles (*Carr et al*., 2003). If such an ocean did exist, where did all that water go? One explanation is that there exists still today large aquifers beneath the Martian surface. While this as certainly not been ruled out, initial radar soundings found no evidence of such aquifers (*Mustard et al*., 2012). It is also possible that what was in the past liquid water is now stored not beneath but within the Martian crust in the form of hydrated minerals. Observations of the water content of these hydrated minerals – and the hydrated mineral content of the Martian surface – (e.g. *Poulet et al*. [2005] and *Mustard et al*. [2008]) suggest it may be possible that an amount of water comparable to the volume speculated to have existed in an ancient ocean may be stored in these hydrated minerals. A final option – which is a strong motivating force behind the research presented in this dissertation – is that some or even most of the liquid water that once flowed on Mars has escaped to space in the form of hydrogen and oxygen particles accelerated out of Mars' atmosphere.

2.2 Achieving Escape Energy

It takes about 1.99 electron volts (eV) of kinetic energy for one oxygen atom (one water molecule's worth of oxygen) to be traveling at a velocity high enough to escape Mars' gravitational field. An oxygen atom with this much energy or more directed upward will escape to space if it does not collide or get pushed back down by some other force (such as the electromotive force of a closed field line that an O^+ ion would follow right back down into the collisional atmosphere). Hydrogen, water's other constituent particle, has the same escape velocity (and hence a much smaller escape energy) than oxygen, and could easily be the primary subject of a dissertation on Mars atmospheric escape, but here focus in is given to oxygen. Consideration of chains of atmospheric chemical reactions has led to the initial conclusion that the rate of escape of hydrogen from Mars' atmosphere should be constrained to be twice the escape rate of O atoms (*McElroy and Donahue*, 1972; *Liu and Donahue*, 1976). Later papers suggest that this may be a situation that holds only statistically over long periods of time (e.g. *Chaffin et al*., (2014); *Chaffin et al*., (2015); *Jakosky et al*., (2017). The following paragraphs describe various means through which neutral or ionized oxygen atoms in the Mars space environment may obtain the requisite energy to escape.

2.2.1 Jeans Escape

Jeans escape is the name commonly given to the escape of neutral particles that find themselves at or above escape energy simply from the random kinetic energy at the top of the atmosphere. A simple way of estimating the quantity of this type of escape is to assume a Maxwell-Boltzmann

velocity distribution (typically a good approximation despite the consideration that particles in or above the transition region are the ones under consideration), and count the number of particles at the high energy tail of this distribution. In other words, integrate an energy probability distribution from 1.99eV to infinity, and the result is the fraction of particles with enough energy to escape. To perform a first order estimate, simply divide this value in half to get an estimate of the fraction of sufficiently energetic particles that are directed "upward." Multiply the result by the probability of not colliding on the way out to deep space. Integrate that altitude-dependent quantity over all altitudes, and the final result is an estimate of thermal escape, or Jean's escape. Works addressing Jeans escape at Mars include Chassefiere and Leblanc (2004) and Brain et al. (2017).

2.2.2 Dissociative Recombination

Another means by which particles gain escape energy is by liberating the energy of a chemical bond. Dissociative recombination refers to the process of a molecular ion and an electron coming together to neutralize while also splitting the molecule into component parts, liberating energy in the process. The amount of energy turned into kinetic energy in this manner is partitioned among various "branching pathways." The dominant ions in the Martian ionosphere are CO_2^+ and O_2^+, and the dissociative recombination of both of these molecular ions include branching ratios for the resulting neutral O that are in excess of ~2eV escape velocity. Recognized as the primary source of the Mars "hot oxygen corona" (*McElroy*, 1972), dissociative recombination should be thought of not only as resulting directly in escape, but also as the generator of an extremely high altitude source population for other escape mechanisms. Works addressing dissociative

recombination at Mars include *Chassefiere et al*. (2004), *Brain et al*. (2017), and *Lammer et al*. (2009).

2.2.3 Polar Wind

Arguably more a location or a loss channel than one specific acceleration mechanism, polar wind has been used as a catch-all term for charged particles accelerated upward along magnetic field lines (*Dubinin et al*., 2011). The term "polar" makes somewhat less sense for an induced magnetosphere than for the Earth because rather than roughly vertical field lines emerging from the atmosphere near the poles of a dipole field, an induced magnetosphere tends to have field lines with a vertical component exiting the atmosphere at all point on a circle drawn at the exobase in the terminator plane. One acceleration mechanism proposed as a means of accelerating ions to escape energy along such field lines with a vertical component is an ambipolar electric field (e.g. *Liemohn et al*., 2006; *Frahm et al*., 2010; *Brecht and Ledvina*, 2012; *Collinson et al*., 2015). In addition to electron pressure gradients, magnetic field pressure gradients may also supply a portion of the energy required for an ion to escape (*Dubinin et al.*, 2011).

2.2.4 Bulk Escape

Bulk escape, which refers to the scavenging of large amounts of ionospheric particles in a single brief burst, has also been observed (e.g. *Halekas et al*., 2016). At least two distinct mechanisms of this type probably exist, both of which correspond to situations in which ionospheric flux tubes become magnetically connected to the solar wind flow. One way for this to occur is

through magnetic reconnection between crustal fields and draped IMF in a way that sends a portion of the ionospheric contents originally trapped on a closed field line out and downstream with the solar wind flow (see for example *Brain et al*., 2010a). Another means by which bulk quantities of ionosphere may find themselves connected to the solar wind requires no reconnection at all, simply a downward convection of draped IMF on the dayside relatively deep into the atmosphere. Even if we were to assume infinite conductivity, and hence the frozen-in assumption for the relationship between charged particles and magnetic field (an assumption that suggests pre-existing ions would be pushed downward rather than becoming connected to this draped IMF), all newly produced ions in the volume of atmosphere now occupied by this solar wind flux tube will be accelerated downtail by a $J \times B$ force when the flux tube slips past the limb of the planet.

2.2.5 Ion Pickup

Such newly born planetary ions that find themselves on interplanetary magnetic field lines are known as pickup ions. If a pickup ion finding itself magnetically connected to the solar wind is in a region of high velocity flow, the $E = -V \times B$ electric field (a mathematically simplified electric field description which assumes charge neutrality and infinite conductivity) can be extremely large.

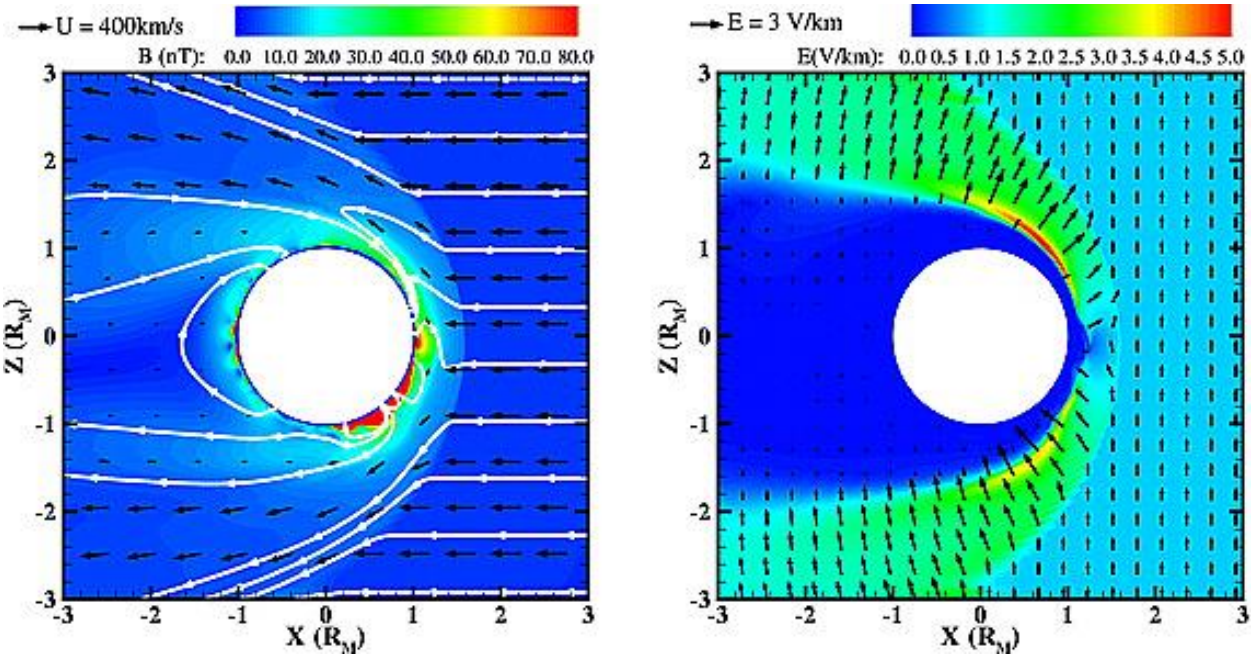

Figure 2.1. This depiction of simulated plasma bulk velocities (left) and electric field strength (right) was created by *Fang et al.* [2008], which used a magnetohydrodynamic code to model the Mars space environment. Focusing on the right: the location at which the color changes from a light blue upstream of Mars to a green is the bow shock. The lower altitude transition, from green to dark blue, is the location of MPB within this simulation.

The right panel of Fig. 2.1 (taken from *Fang et al.*, 2008) shows the magnitude and direction of this convective electric field for specific yet fairly typical upstream solar wind conditions. It is important to note the sharp transition from the high end of the color bar's spectrum (red) to the low end (dark blue) at the induced magnetosphere boundary, or MPB. Consideration of our simple equation, $E = -V \times B$, helps to elucidate the cause of this drastic shift from a relative weak convective electric field inside of the induced magnetosphere to the very large magnitude field that exists outside this boundary. The magnetic field magnitude, as has been discussed, is actually weaker on the outside of this boundary. The stronger electric field, therefore, is due to the other two components of this equation: the bulk velocity and the cross product between the vectors. Bulk velocities are much slower inside of the MPB, as is clearly evident in the left panel of Fig. 2.1. Additionally, the angle between the magnetic field and the flow direction is often

quite small inside the MPB, as the draped magnetic field aligns with the velocity around the planet, causing their cross product to nearly vanish. Pickup ions in the context of Mars ion escape observe the same fundamental physics as pickup ions in other astrophysical contexts. Born into a plasma flow, these ions see the magnetic field of this plasma flow moving past them at the bulk flow speed of plasma, and feel a $-V \times B$ force accordingly. (The negative sign here *is* for positively charged particles and is due to the fact that the velocity in this expression is the velocity of the background magnetic field relative to the particle, as opposed to the velocity of the particle relative to the background field). Because all pickup ions of the same source experience the same bulk flow velocity, their initial acceleration will be in the same direction as they begin to gyrate around the magnetic field. Ions picked up one half of a gyroperiod later in time will be 180° out of phase but are still said to occupy the same "ring" in velocity space (e.g. *Yamauchi et al*., 2004; 2008). As is typical of plasma anisotropies, waves arise that tend to isotropize. Picked up ions experience pitch angle scattering, transforming the ring in velocity space into a thin spherical shell. The presence of this spherical shell in velocity space, which can be thought of as a spike in the energy distribution of the plasma, is still not stable, and diffusion in velocity space will eventually occur. For the case of ions picked up by the solar wind at Mars, however, this process of isotropization appears to occur on larger time scales than the amount of time it takes for solar wind to flow past the planet. The result is that the initial velocity space ring distribution is visibly present in pickup proton and heavy ion populations at Mars (*Yamauchi et al*., 2008; *Najib et al*., 2011; *Curry et al*., 2013a). A key factor that sets Mars apart is that the gyroradius of solar wind pickup ions at Mars can be large enough to result in planet-scale asymmetries, where 10 keV O^+ (O_2^+) ions flowing perpendicular to a ~10 nanotesla magnetic field have gyroradii of about 1.7 (2.4) Mars Radii. The most natural comparison would be

Venus, another inner planet with an induced magnetosphere, where proximity to the sun results in stronger IMF, a more radial Parker Spiral results in pickup ion velocities that are less perpendicular to the solar wind flow (reducing $v \times B$), and the planet's larger gravity results in fewer ions being born at the exospheric altitudes at where the requisite fast convective plasma flow is located. These three factors do not compete. They all work together to reduce the gyroradius, making planet-scale gyroradii the exception at Venus. At Mars, however, such large-scale asymmetries appear to be the norm, resulting in a population of pickup ions capable of leaping over the planet in a single bound, with the initial trajectory of their first gyration sending them away from Mars in a direction perpendicular to the solar wind flow. This occurs in the $+E_{sw}$ hemisphere, a name given to the hemisphere where the convective electric field points away from the planet. In the $-E_{sw}$ hemisphere, where the convective electric field accelerates ions down toward the planet, pickup ions themselves do not directly escape, but the effects of their high energies imparted by the convective electric can still be impactful.

2.2.6 Sputtering

The final source of energy for escape discussed here is sputtering, the process of particles at the top of the atmosphere being bumped or splashed into space by high energy particles precipitating into the atmosphere. The most discussed source of such energetic precipitating particles are pickup ions in the $-E_{sw}$ hemisphere. The energy deposited by these energetic oxygen ions slamming into atmosphere can directly eject particles (e.g. *Johnson et al*., 2000), or provide a boost to the energy and altitude of particles that enhances the extended neutral corona (e.g. *Johnson and Luhmann,* 1998). It is believed that sputtering effects were more prominent when the sun was younger, and estimates of the contribution of sputtering to atmospheric escape over

the lifetime of Mars are has high as 30% of the total amount of oxygen lost (*Luhmann et al.*, 1992).

2.3 Goals of the Research Community

With the larger goal in mind of estimating the quantity of water that may have escaped to deep space over the lifetime of Mars, at least three subgoals must be met. First, total escape can be divided into distinct and preferably non-overlapping escape processes, as was done in section 2.2. An alternative to such categorization of escape channels may be found in *Dubinin et al.* [2011]. Observations and models may be used in conjunction with each other to estimate escape fluxes for each of these escape channels for specific solar EUV and solar wind parameters. Second, studies of how the particle flux in each of these loss channels changes as these solar parameters, or drivers, change, must be completed. Third, in order to utilize knowledge of how drivers affect escape fluxes, reasonable values for these drivers must be estimated for all time periods spanning our solar system's history.

One consideration that may not fit cleanly into one of these three steps (estimating escape, estimating how this escape changes with drivers, and estimating how drivers have changed over time) is the question of how long Mars may have had a planetary dipole magnetic field, and how this field may have mediated escape. It can be argued that it is not immediately obvious that a planet with no planetary dynamo will experience more escape. After all, although the absence of a dynamo allows solar wind fields themselves to interact directly with the ionosphere, providing an additional source of acceleration, the presence of a dynamo exposes the magnetospheric system to energy from a larger cross sectional area of solar wind flow. What if energy from

portions of the solar wind that would pass by present day Mars could have been funneled by the ancient planet's intrinsic magnetic field to the magnetic poles, resulting in an increased polar wind outflow more analogous to the polar wind seen at Earth than to the polar wind discussed in the previous section? The dual questions of how much of atmospheric escape is unique to induced magnetospheres vs. how much is unique to planetary magnetospheres arising from an internal dynamo are very difficult to answer with observations alone. Observed particle and energy fluxes and locations are not always unique to one particular escape channel. As a result, escape tends to be classified not as "induced magnetosphere type escape" and "dipole field type escape," but simply as "neutral" or "ion" escape, a distinction arising as much out of the convenience of categorizing particles according to the instrument that detected them as from the desire to categorize escape mechanisms by the type of force that may have provided the particles with escape energy. One preliminary answer to the question of how an ancient Martian dipole may have altered escape rates can be found in *Dong et al*. [2017], which uses a magnetohydrodynamic (MHD) simulation to estimate ion escape rates from the nearby exoplanet Proxima Centauri B. Performing separate runs of their code for a case in which Proxima Centauri B is assumed to be unmagnetized and for which it assumed to host a strong planetary dynamo, *Dong et al*. found that ion escape fluxes were fully two orders of magnitude greater for the unmagnetized case. This is a first step toward understanding the overall impact that the presence or absence of a planetary dynamo can have on the escape of charged particles.

2.4 The Present Dissertation in the Context of these Broader Communal Research Goals

Preferential attention to detail in section 2.2 was given to the description of pickup ions because the study of heavy energetic planetary pickup ions escaping Mars' atmosphere (and the

associated convective-electric-field-based asymmetry of heavy ions in near Mars space) is central to all of the original work presented in the following chapters. The escape of planetary ions from the atmosphere of Mars into space has been investigated using measurements taken by Phobos-2, Mars Express (MEX), and the Mars Atmosphere and Volatile Evolution (MAVEN) spacecraft. Already in the Phobos-2 data there was evidence of a population of energetic heavy planetary ions, known as pickup ions, that extends outside of the induced magnetosphere boundary (IMB) (e.g., *Kallio et al.,* 1995*; Lundin and Dubinin*, 1992). Energetic planetary ions beyond the IMB were later also observed in MEX data (e.g. *Lundin et al.,* 2008). Analyses of both Phobos-2 and MEX data sets suggested that less energetic ions flowing within or close to the IMB dominated ion escape (e.g., *Lundin and Dubinin*, 2002; *Barabash et al.,* 2007). Additionally, MEX heavy ion data from the magnetosheath is often contaminated by strong proton fluxes, complicating the process of examining a region already thought to be of minor importance in terms of total escape fluxes (*Nilsson et al*., 2011). As a consequence, MEX studies of heavy ions tended to focus on ions located inside of the IMB (e.g., *Lundin et al.*, 2004; *Barabash et al.*, 1991; *Dubinin et al.*, 1996, 2006; *Fedorov et al.*, 2006; *Nilsson et al.*, 2011, 2012; *Liemohn et al.*, 2014).

At the same time, multiple numerical models predicted significant fluxes of pickup ions well outside of the IMB with initial trajectories not downtail, but in the direction of the solar wind convective electric field, $E_{SW} = - v_{SW} \times B_{IMF}$, where IMF stands for interplanetary magnetic field (e.g., *Luhmann and Schwingenschuh*, 1990; *Kallio and Koskinen*, 1999; *Boesswetter et al.*, 2004; *Modolo et al.*, 2005; *Harnett and Winglee*, 2006; *Kallio et al.*, 2006b; *Fang et al.*, 2008; *Najib et al.*, 2011; *C. Dong et al*. 2015). In the $-E_{SW}$ hemisphere – the hemisphere where the electric field points toward Mars - this ion population was predicted to be accelerated into the atmosphere and

lost. In the in the $+E_{SW}$ hemisphere, however, the ions are expected to be accelerated away from the planet in a direction perpendicular to the bulk solar wind flow, roughly perpendicular to the Sun-Mars line. In some cases, this energetic plume of pickup ions was predicted to contain as much particle flux as the central tail loss channel (*Curry et al.*, 2013; *Liemohn et al*., 2013).

Asymmetries in the planetary ion flow around Mars related to the effects of crustal fields had been observed previously (e.g., *Lundin et al*., 2011). Global asymmetries in the distribution of ions around Mars caused specifically by E_{SW} had also been reported, but these studies were either focused exclusively on ions observed within the IMB (*Carlsson et al*., 2008; *Dubinin et al*., 2006) or included ions from a broad energy range, allowing the less energetic ions to dominate the results (*Barabash et al*., 2007; *Fedorov et al.*, 2006, 2008; *Dubinin et al*., 2006). Pickup ions such as those produced in numerical models – a high energy population that can extend outside the IMB - have also been reported (*Dubinin et al.*, 2011; *Edberg et al*., 2009; *Liemohn et al*., 2014). These studies describe ion populations that increase in energy with distance from the planet, consistent with acceleration by E_{SW}, but these were case studies including only a small number of observations.

This dissertation addresses each of the following questions of interest to the research community:

- How well can the energetic plume of escaping planetary ions be seen in MEX IMA data beyond the MPB (i.e., in the magnetosheath and solar wind)?
- What are the statistics of energetic planetary ions outside of the MPB as a function of solar wind motional electric field?
- How can the assumed IMF proxy at Mars be improved?

- What changes to the planetary ion plume statistical characteristics are revealed by using an improved IMF proxy?

The next chapter, chapter 3, provides an overview of the various channels through which Mars' atmospheric particles can escape into deep space. A systematic search through Mars Express data for the predicted energetic plume of pickup ions was still absent prior to the work present in chapter 4. A statistical survey of MEX data for energetic heavy ions outside of the IMB was still absent prior to the study that will be described in chapter 5. Chapter 6 will detail an undertaking to facilitate searches through Mars Express data for energetic plume signatures or any other process or asymmetry in the Mars space environment that is oriented by the angle of the upstream IMF. Along the way, insight was gained into magnetic field configurations at "mid" altitudes, where magnetic field lines may be variously closed, open, or draped. Finally, chapter 7 unveils a project still in its infancy. Building upon the work done in chapters 5 and 6, and focusing specifically on the energetic plume escape channel, chapter 7 discusses an attempt at tackling the broader goal of determining how particle escape fluxes from Mars vary with solar drivers. All of these things are put into perspective in chapter 8, which puts things in context, providing a discussion of how and where the work presented in chapters 4-7 fits within the body of work that exists concerning Mars ion escape. Lastly, chapter 9 offers a final summary of the findings presented in this dissertation, before giving a brief glimpse at some potentially valuable work that has yet to be done.

Chapter 3: Datasets and Models Used

3.1 Mars Express

In December of 2003, European Space Agency's Mars Express (MEX) achieved orbital insertion at Mars. Fourteen years later, at the time of writing of this dissertation, it is still operational. Among the satellite's suite of instruments is ASPERA-3, a collection of in situ particle instruments, including an Ion Mass Analyzer (IMA), an ELectron Spectrometer (ELS), a Neutral Particle Detector (NPD) capable of distinguishing between hydrogen and heavy particles such as oxygen, and a Neutral Particle Imager (NPI) capable of measuring fluxes of energetic neutral atoms at higher energies than the NPD, but unable to resolve mass. A full description of the ASPERA-3 instruments can be found in *Barabash et. al*. [2004, 2006].

3.1.1 Ion Mass Analyzer

All ion data presented in the following chapters are from IMA. IMA's field of view is 360° azimuthally by 90° of elevation angle, with a deflection system in place to accept ions into the instrument from specific elevations at any given time. In addition to sweeping through elevation angle to achieve the 90° elevation angle field of view (see Fig. 3.1), IMA sweeps through a range of energies (96 energy steps in the range 10 eV - 32 keV per charge). This is done by exposing particles that have entered the instrument to radial electric field of varying strength. Only particles within the desired energy range for an energy step will have a radius of curvature in this field that matches the hemispherical shape of this electrostatic analyzer, allowing them to pass

through toward the detector. Once a specific range of energy per charge has been isolated in this way, a "post-acceleration voltage" is applied, accelerating the ions before they enter a toroidal magnetic field designed to deflect ions outward from a center line that is directed toward the center of a dart-board shaped detector. The concentric rings of this detector correspond to different ion masses, with the lighter ions being deflected outward more toward the outer rings, and heavier ions being deflected less, causing them to hit the detector nearer the center. The purpose of the post-acceleration voltage that is applied after energy is selected but before mass is resolved is to allow for instrument settings designed for example for solar wind detection or for better mass resolution of heavy ions. A solar wind type post acceleration (or PAC) setting should accelerate protons sufficiently that their trajectory will not be bent so much that it misses the detector completely. A post-acceleration geared toward improved mass resolution, on the other hand, should have particles moving more slowly, thereby increasing deflection amounts, so that the difference in deflection of O^+ and O_2^+, for example, may be resolved.

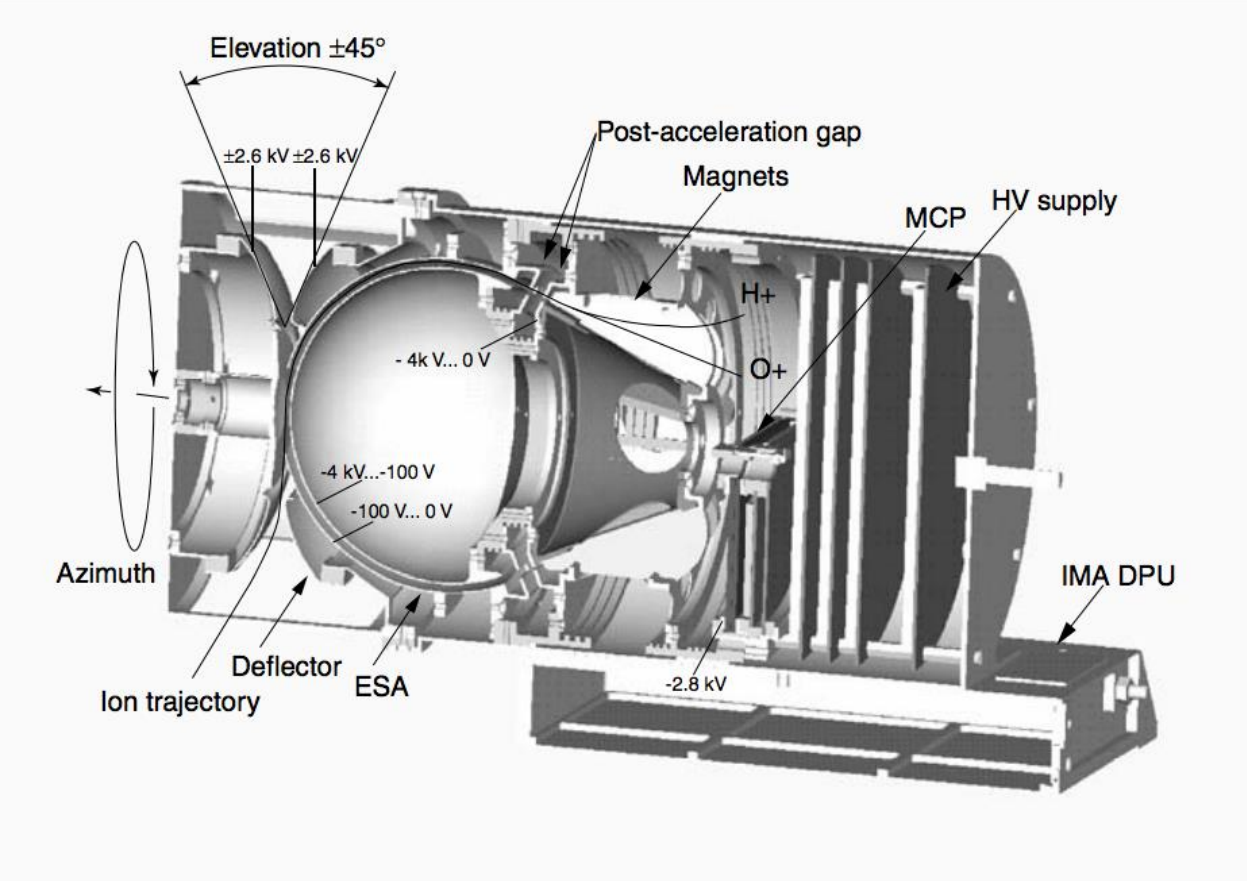

Figure 3.1. A diagram of the Ion Mass Analyzer taken from Fig. 28 of *Barabash et al*. [2006]. Particles enter the detector where the diagram shows the elevation angle deflector that allows ions in from one particular range of elevation angles at a time. The instrument field of view is a 90° wide range of elevation angles, rotated around instrument's axis of symmetry, for a 360° by 90° field of view.

3.1.2 Electron Spectrometer

The ELS is a great instrument for spacecraft missions in that it is both light-weight (almost ten times lighter than IMA) and also has low power requirements. ELS has a field of view of 360° by 4°, and employs logarithmically stepped energy bins in the 0.01-20 keV energy range. While the work presented in this dissertation is focused on ions, particularly those typical of the energetic plume escape channel, electron spectrometers in the Mars environment, particularly for a spacecraft that lacks a magnetometer, are often able to provide a good indication of which side

of plasma boundaries the spacecraft is located. Recall that in section 1.4 it was noted that an inward crossing of the MPB is accompanied by a decrease in electron temperature. This is precisely how the ELS will be used in chapter 4. Greatly increased fluxes of high-energy electrons are used to establish that MEX was indeed in the magnetosheath (outside of the MPB) at the time of detection of some energetic plume type planetary ions.

3.1.3 MEX Data Analysis Hurdles and Complications

The 360° by 90° field of view of IMA means that there are blind spots at the "poles" of the instrument. Although the size of these blind spots is relatively small (the instrument can see ions from over ¾ the full 2π sphere of flight directions), the blind spots are very unfortunately oriented. IMA was mounted on the spacecraft, in part, "to co-aligned the central plane of the IMA field of view with the ecliptic plane when the spacecraft is in the Earth pointing mode" (*Barabash et al*., 2006). An effect of this alignment is that when the IMF is in the ecliptic plane, the convective electric field, E_{SW}, accelerates ions in a direction outside of IMA's field of view. The population of planetary ions studied, energetic pickup ions, are accelerated by this field and are expected to be outside of IMA's field of view if they are still in the first portion of their large gyration about the IMF.

A second difficulty with the search for energetic plume signatures in MEX ion data is the presence of "ghost counts" in IMA observations. "Ghost" counts occur when solar wind protons cause false counts in heavy ion mass rings. Ghost counts are false counts which appear when a proton's path inside of IMA misses the detector, and their prevalence when MEX is in the solar wind was one reason that the region outside of the MPB was not previously studied in nearly the

same detail as the space inside of Mars' induced magnetosphere proper. Fortunately, a colleague at the Swedish Institute of Space Physics in Kiruna Sweden, Robin Ramstad, whose Ph.D. dissertation also examines planetary ion measurements by MEX IMA, was able to provide Figure 3.2, which helps illustrate where such proton contamination occurs as a function of energy and mass ring (an energy-mass matrix). Fig. 3.2 (a) shows many integrated solar wind measurements taken when the post acceleration setting of IMA was 2400V, whereas Fig. 3.2 (b) shows a similar integrated energy-mass-matrix, but for a post acceleration setting of 4200V. To minimize H^+ contamination of the heavy mass rings, we restrict the study to times when IMA was operating with a post-acceleration voltage of 2400V, and only include heavy ions striking mass rings 0-11 in the 2-15keV per charge energy range. This range is loosely indicated by a red oval in Fig. 3.2 (a). For this energy range and PAC setting, protons inside IMA strike the detector well away from the detector's edge, resulting in an orders of magnitude reduction in ghost counts, making it unlikely that ghost counts have significantly impacted our findings. Note that, because the ions considered are composed overwhelmingly of singly charged particles, the shorthand "2-15 keV" will be used in place of "2-15 keV per charge) for the duration of this dissertation.

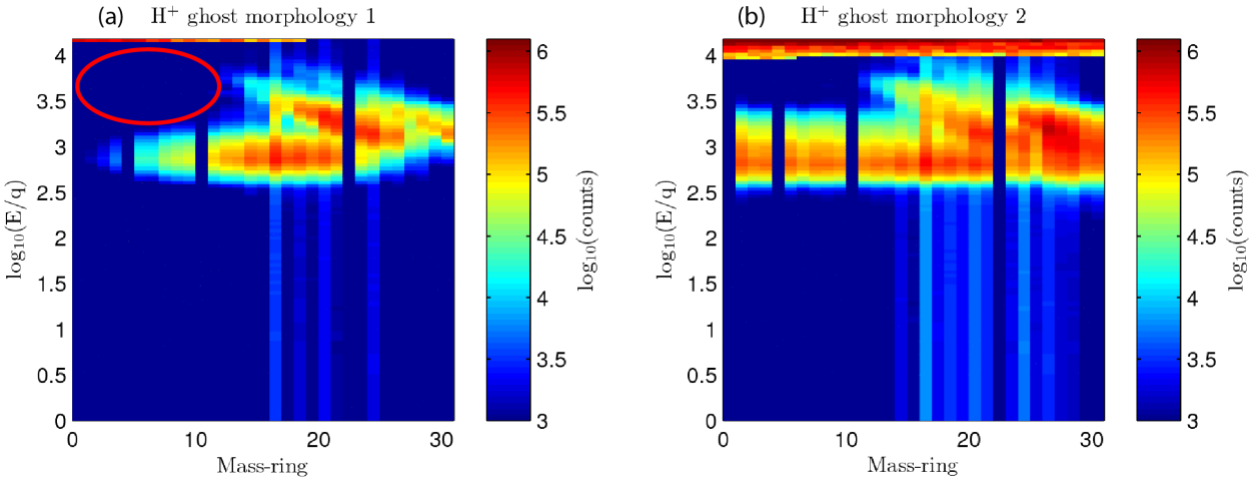

Figure 3.2. Integrated solar wind measurements showing how solar wind protons are dispersed across IMA's mass channels when IMA is operating in different two different modes: a post acceleration of 2400V (a), and a post acceleration of 4200V (b). The energy-mass regime from which data was taken for this study is indicated qualitatively with a red oval. The important point is that the oval is empty. This highlights the fact that, for the post-acceleration voltage for which data was used in this study, we were able to restrict the study to an energy and mass range that is free of ghost count contamination.

Apart from a field of view far from perfect for observation of this particular population of particles, and ghost counts masquerading as heavy ions, a third impediment to the use of MEX data to observe Mars' energetic plume is the fact that there is no magnetometer on board MEX. Upstream of Mars, there is no analogue for the Advanced Composition Explorer (ACE) spacecraft that sits at the L1 point upstream from Earth. No observations are present to allow people to know the magnetic field direction and other plasma parameters of the solar wind that is impacting the Martian plasma environment. This has led to a situation in which researchers attempting to study a phenomenon or a particle population such as pickup ions that is organized by the direction of the IMF prior to the arrival of NASA's MAVEN spacecraft in 2014 had only one magnetometer with which to estimate IMF direction. Not only was this magnetometer not in the upstream solar wind. It was way down at 400km altitude, where interaction with the Martian ionosphere and crustal fields prevents magnetic field observations from matching the direction of E_{SW}.

3.2 Mars Global Surveyor

The magnetometer referred to above was that onboard NASA's spacecraft Mars Global Surveyor, the same magnetometer that discovered that Mars does not have a global dipole magnetic field but rather strong crustal magnetic fields. Between April 1999 and October 2006 MGS magnetometer observations are available from what is known as the "mapping phase orbit"

of MGS. The spacecraft was parked in a 400km altitude 2am-2pm polar orbit. Much like the same side of Earth's moon remains directed toward Earth because the moon's rotation about its axis takes the same amount of time as its orbit around Earth, MGS was able to remain at the same local time because an orbital inclination slightly offset from 90° was used to obtain a rate of orbital precession that matched the rate at which Mars orbits the sun. The usefulness of remaining at the same local time above the planet is that, as the planet spins beneath the satellite, all longitudes are sampled evenly by spacecraft observations, exactly what was wanted in order to map out the magnetic fields of Mars. Like MEX, MGS was equipped to measure electrons. The electron reflectometer of MGS was used by *Brain et al*. [2006] to infer magnetic connectivity at 400km, leading to the conclusion that the fields observed at this altitude at 2pm on Mars' dayside were, at least for particular latitude bands, usually draped field lines, magnetic field that was connected to the solar wind at both ends.

3.2.1 MGS 400km Observations as an IMF Proxy

Once it is established that the magnetic field being observed is draped IMF rather than loops of crustal magnetic field, it becomes reasonable to ask whether these draped field lines down at 400km may be used to infer the angle of the IMF in the upstream solar wind (and hence the direction of E_{SW}). *Brain et al.* [2006] does exactly that. Using the assumption that the IMF field lines drape parallel around the planet (remaining in the same plane as the upstream field line), *Brain et al.* [2006] developed a 2-hour cadence data set which provides estimates of the upstream clock angle, θ_{IMF}, using magnetometer data from the 400km orbit of MGS. This set of IMF clock angle estimates has been widely used (e.g., *Carlsson et al.*, 2008; *Dubinin et al.*, 2008; *Nilsson et al.*, 2011; *Wang et al.*, 2013; *Dieval et al*., 2014), and it was adopted as the IMF clock

angle proxy used in chapters 4 and 5 of this dissertation. There is a large uncertainty in this estimation of θ_{IMF} due to draping configurations that are not ideal, due to field observations that are sometimes not of draped IMF at all, and also due to time variation in θ_{IMF}. An in-depth consideration of these factors is this basis of chapter 6.

3.3 Multi-Fluid MHD at Mars

In an effort to understand how interaction with the ionosphere bends draped interplanetary magnetic field lines, chapter 6 of this dissertation will make use of the Block-Adaptive-Tree Solar-wind Roe-type Upwind Scheme (BATS-R-US) multifluid magnetohydrodynamic (MHD-MF) model. This model included four ion species (H^+, O^+, $O2^+$, and CO_2^+), thermospheric densities, winds, and ionization frequencies taken from the Mars Global Ionosphere Thermosphere Model (*Bougher et al.*, 2015), and hot coronal densities taken from the Mars Adaptive Mesh Particle Simulator (*Lee et al.*, 2015). Both the theremosphere and exosphere are 3-D results. This type of multi fluid modeling work at Mars is the outgrowth of work that was performed in *Dong, C. et. al.* [2014], which details how the MHD-MF was coupled to previously existing models of the Martian ionosphere and thermosphere (*Bougher et. al.*, 2011). Crustral fields were removed from the simulation, the 100km inner boundary was set with B=0, and EUV flux was set to values representative of solar maximum at Mars' aphelion. Specifically, this means that the $F_{10.7}$ value for this model run was 74 solar flux units. Upstream solar wind conditions were a proton density of $4cm^{-3}$, a temperature of 3.5×10^5 K, and a bulk flow speed of 400 km/s. This is the same model run used as case B of *Liemohn et al.* [2017], which gives a more complete description of the model and of the specific run of the model used, than is given here.

Chapter 4: Energetic Plume Case Study and Initial Statistical Survey

This study was the first systematic search through years of MEX ion data for observations of the energetic plume of pickup ions in the regions of near-Mars space where it was predicted by models to exist. Two approaches were used. First, a search was performed through all IMA data collected on orbits when the direction of E_{SW} was closely aligned with the MEX orbital plane. This search yielded nine instances of unambiguous energetic (>2 keV) O^+ observations that were consistent with the energetic plume escape channel. The result, because it contains the problem inherent to looking for something only where you expect to find it, also begged the question: "are observations of energetic plume type ions actually more likely when one looks in the estimated direction of E_{SW}, or might this type of observation be equally likely in other directions from Mars center?" As a response to this line of questioning, the second portion of this study was a survey of all clock angles around Mars rather than a narrow window surrounding the estimated E_{SW} direction. This survey included many thousands of "data packets," complete IMA sweeps through all look directions and energies. The same Dave Brain-developed IMF clock angle proxy was used to estimate the direction of E_{SW}, which was then used to rotate observations into a Mars-Solar-Electric field (MSE) coordinate system. The result of this initial statistical survey was that the expected asymmetry in which fluxes of energetic heavy planetary ions is far higher in the $+E_{SW}$ hemisphere than in the opposite ($-E_{SW}$) hemisphere was only very weakly visible in the data.

4.1 What Does the Energetic Plume Look Like?

Ions born at extremely high altitudes, in the fast solar wind flow, are accelerated by the convective electric field, E_{SW}, in a direction perpendicular to the solar wind flow. In the hemisphere where E_{SW} points away from the planet, these ions take off into deep space. The gyroradius of these ions can be so large that not only can they leap past the planet in a single gyration, but their trajectory may take them out well beyond the bow shock before their cycloid motion bends them in the direction of solar wind flow, which in the zoomed-out view is the ultimate direction of the ExB drift of these particles (e.g., *Luhmann and Schwingenschuh*, 1990; *Kallio and Koskinen*, 1999; *Fang et al*., 2008). The energetic plume of particles arcing past the planet in the first gyration of this ExB drift is most dense near the terminator plane (e.g. figures 4 and 5 of *Fang et al*., 2010) and extends backward over the "top" of the planet in feature reminiscent of a mohawk. The velocity of these pickup ions ranges up to about two times the solar wind velocity (at the top of their gyration bounce). Because these are heavy ions (hydrogen's low mass results in a gyroradius too small for protons to be a part of the plume, whose very shape is defined by the large gyroradius of heavy ions), this velocity corresponds to energies of up to many tens of keV. Energy time spectrograms of plume observations often display a characteristic signature of increasing energies as the point of observation moves to higher altitudes (*Dubinin et al*., 2011; *C. Dong et al*., 2015). Generally speaking, this type of signature would be expected of any population of charged particles with a source near the planet that is accelerated by an electric field pointing away from the planet. In addition to the characteristics just listed (high fluxes of heavy keV ions near the terminator plane in the $+E_{SW}$ direction), it should be expected that the flow direction of these particles is roughly uniform and in the direction of E_{SW} or at some angle between E_{SW} and the downstream flow direction. In

other words, clear energetic plume observations should be "beams" of ions rather than ions entering the detector from many directions.

4.2 Case Study Methods and Results

In order to look for the energetic plume where E_{SW} is strongest – and also to help establish this work as distinct from previous studies which focused overwhelming on observations inside the MPB) – times when MEX was outside the average MPB location were identified. All times when MEX was inside the MPB were omitted from the survey. The next step taken for the search for individual instances of energetic plume sightings was to identify all MEX orbits for which the estimate of E_{SW} was within 5° of the orbital plane. This task was performed by using ephemeris data to compute normal vectors for MEX. Because the magnetometer of MGS provides a new estimate for the direction of ESW for each MGS orbit (a 2-hour cadence), normal vectors were computed for each 2-hour long segment of MEX orbit. Each 2-hour span of time whose corresponding MGS-derived estimate of E_{SW} was within 5° of the orbital plane was flagged for close examination. To further down-select the quantity of data that would be sifted through by eye, the requirement that MEX be on the $+E_{SW}$ side of the planet, near the terminator, and above the MPB was also imposed. This filtering left just 57 possible 2 hour long periods of time to examine. Of these 57 time intervals, nine contained a clear measurement of the energetic plume, exhibiting significant fluxes of heavy ions >2 keV.

Figure 4.1 displays one of the energetic plume observations that was found. In all three panels, the sun is to the left, the green and red curves represent the statistical location of the bow shock and MPB respectively, as calculated in *Trotignon et al*. [1996]. The top panel is in cylindrical

coordinates, and the other two panels are projections looking at the duskside of Mars (b) and down on Mars' orbital plane (c). The black curve (other than the circle representing Mars) is the orbital trajectory of MEX during the 2-hour period during which energetic plume ions were observed. Overplotted along the spacecraft's path is the count rate of singly ionized oxygen, or more specifically, the O^+ counts observed per IMA sweep (per 192 second sweep of all look directions and energies by the IMA). It can be seen that as MEX passed the terminator plane (x=0) above Mars' north pole, a strong burst of O^+ was observed. A caveat to keep in mind when viewing the plots that are in units of counts is that, because faster ions will enter the detector more frequently and be preferentially observed, count rate should not be used as an indicator of particle flux. Count rate is, however, proportional to the energy flux carried by this (or any) particle population.

The average location of the MPB shown in red is cylindrically symmetric by the very nature of how it was calculated (*Trotignon et al*., 1996), and so it is readily apparent from the top panel of Fig. 4.1 that MEX was outside of the average location of the MPB when these ions were observed. The actual position of this plasma boundary at any given time, however, is highly variable (e.g. *Trotignon et al*., 1996; *Vignes et al*., 2000). A demonstration that these observations did in fact occur outside of the MPB in the magnetosheath (as opposed to this being yet another observation of escaping planetary ions inside the MPB) is seen in Figure 4.2. The top and middle panels of Fig. 4.2, showing electron and proton fluxes respectively, provide convincing evidence that MEX was indeed in the hot magnetosheath plasma at around 17:30-17:50 UT when the high fluxes of energetic O^+ were detected (circled in yellow). The outward cross of the MPB at around 17:20 is a very sharp transition, leaving little doubt concerning the

plasma regime in which these observations occurred. It is also worth noting that a comparison of panels (b) and (c) indicate that the enhanced O^+ fluxes occurred at a time when there was no anomalous activity seen at the same energies in the proton data. This suggests that there is no reason for concern that the enhanced O^+ fluxes are really ghost counts rather than actual oxygen. In short, this is an unambiguous observation of energetic heavy planetary ions consistent with what is expected of the energetic plume ion escape channel. The O^+ fluxes seen in Fig. 4.2 are on the order of 10^6 ions $cm^{-2}s^{-1}sr^{-1}$, magnitude right in line with what simulations had already predicted (Figure 3 of *Kallio et al., 2008*, and Figures 7 and 8 of *Curry et al*., 2013a).

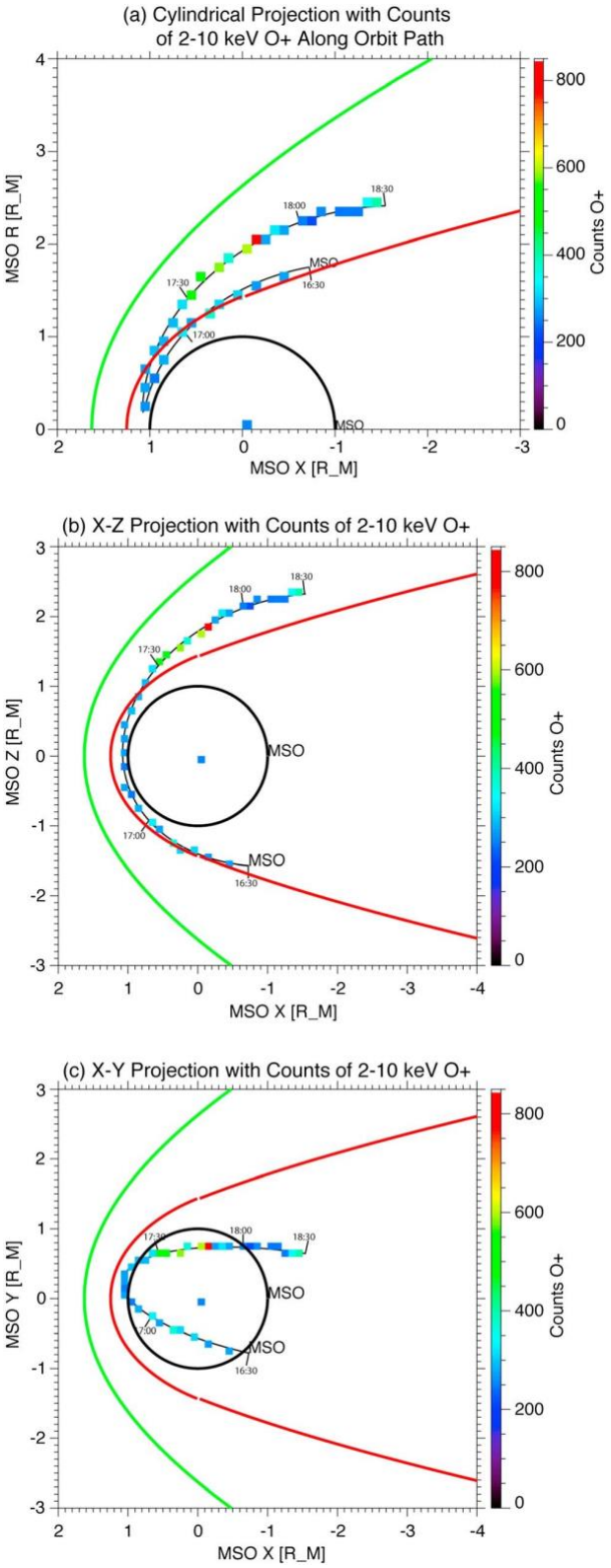

Figure 4.1. MEX orbit during a two hour interval on October 9, 2005 in the Mars Solar Orbit coordinate system. The green and red curves indicate the bow shock and MPB location, the circle represents Mars, and the colored boxes indicate 2-10 keV O^+ counts per sweep of velocity space.

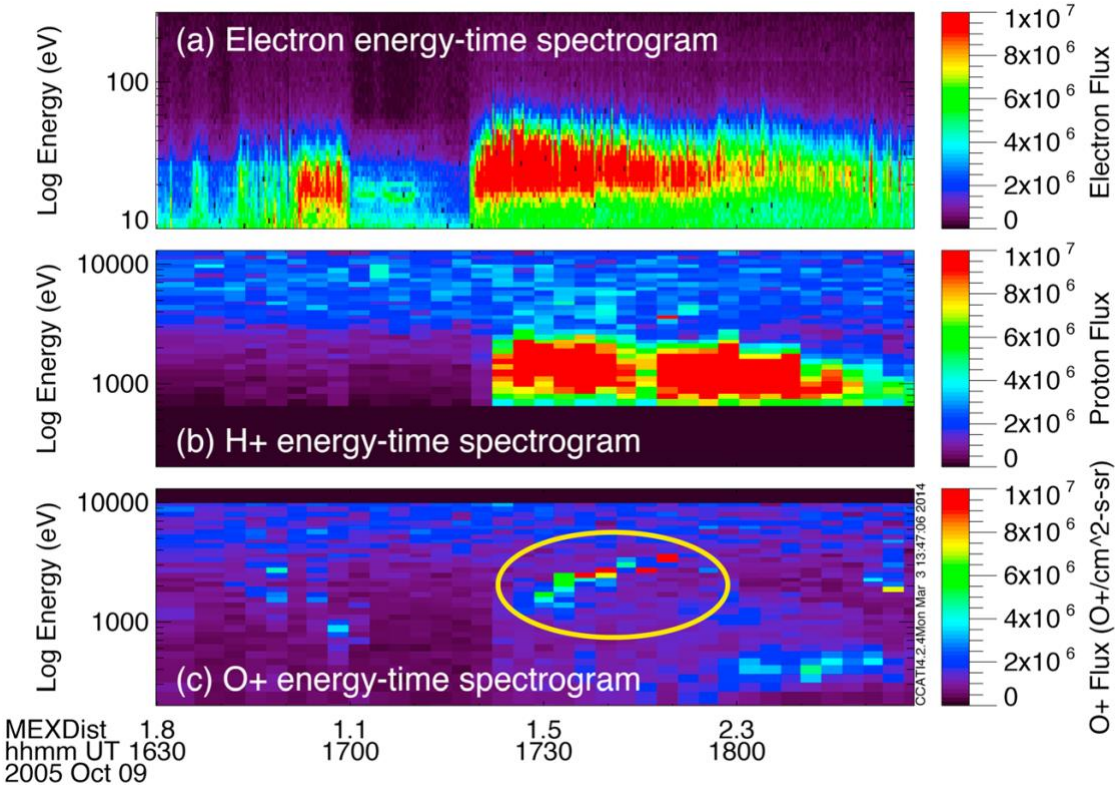

Figure 4.2. Energy-time spectrograms from MEX during a 2 hour interval on October 9, 2005. All particle flight directions are included. (a) shows electrons particle flux. (b) shows proton particle flux. (c) shows O^+ particle flux.

A yet closer look at this same event is seen in Figure 4.3. Fig. 4.3a is an energy-time spectrogram of O^+, much like Fig. 4.2c. The expansion of the vertical axis (energy) in Fig. 4.3a helps to highlight a classic energy plume signature, the increase in energy detected ions as the spacecraft moved further from the planet (which for the event is the same as moving forward in time, since the MEX was gaining rather than losing altitude at this time. Fig. 4.3b was produced specifically to demonstrate how unlikely it is that the heavy ion fluxes observed where in fact heavy ions and not the ghost counts that can plague IMA when outside of the MPB. The vertical axis of Fig.4.3b is "mass channel," with each channel corresponding to one of the concentric rings in the mass-resolving dart-board shaped detector within the Ion Mass Analyzer. A numbering system from the inside (where heavy ions impact the detector) outward (to where

lighter ions impact) results in a mass-time spectrogram as seen in Fig. 4.3b for which the lower mass channels correspond to heavier ions, while the higher mass channels correspond to low mass ions. In cases where proton-caused ghost counts are prevalent, a distinct vertical line appears in this type of mass-time spectrogram, as a huge swath of mass channels being flooded with ghost counts for a brief time. Focusing attention on the specific times when enhanced O^+ fluxes were seen, it can be seen that enhanced count rate in the lower mass channels (where oxygen is expected to hit the detector) taper off and do not extend upward into the mid-range mass channels. This is a sign that the detector is functioning as it should, with heavy ions hitting the detector where expected as opposed to detections registering across mass channels, which would lead one to suspect that mass channels are being hit after particles bounce within the instrument rather than particles curving cleanly through the detector's magnetic field and onto the dart board according to their mass.

Fig 4.3c shows the flight direction of this population of energetic oxygen at one snapshot in time (17:49:15). The horizontal axis represents the elevation angle at which ions entered IMA, and the vertical axis shows the azimuthal angle. This panel communicates two important things that further solidify the argument that this is an observation of the energetic plume. First, it is obvious that the vast majority the O^+ counts are coming from a specific look direction. A directed beam of ions, as expected from the plume. Second, the direction from which these ions are coming is consistent with flow in the direction of the estimated E_{SW}. The particular flow direction of this ion beam also serves as a reminder of the problematic orientation of the field of view of IMA. Due to our methodology, these observations over the north pole were examined specifically because the estimated E_{SW} direction at this particular time was northward. A northward E_{SW}

corresponds to IMF in the ecliptic plane. As was stated in chapter 3, the orientation of IMA on MEX is such that, during times when the IMF is in the ecliptic plane, the energetic plume ions whose flight directions are most nearly perpendicular to the solar wind flow will arrive at the spacecraft from a direction outside of IMA's field of view. Sure enough, in Fig. 4.3c the ion beam appears at the very edge of IMA's elevation angle field of view. It seems somewhat likely that the ions observed in this case were those far enough along in their enormous gyration to have tilted their trajectory in the antisunward direction, and that energetic plume ions at this time that were still at a steeper angle were present but not detected by IMA.

Figure 4.4 shows a final step in the process of affirming and reaffirming that these are indeed observations of O^+. The top two panels show an energy-time spectrogram of this same October 9, 2005 event using a "standard" calibration, while the two bottom panels show the same but with stricter calibration settings, settings which risk eliminating real O^+ counts to ensure that all or most false counts are removed. A comparison between Fig. 4.4a and 4.4b shows that supposed O^+ fluxes at energies above 7 keV are removed by the enhanced calibration method, but the data signature of interest, the plume like ions increasing in energy from about 2 keV to 4 keV as MEX moves further from Mars, remains mostly unchanged. A comparison of the mass channel vs time plots on the right side of Fig. 4.4 demonstrates that one of the changes in the enhanced calibration (bottom panels) is that problematic mass channels within the instrument, such as mass channel 5, have been recalibrated to better reflect the real plasma environment.

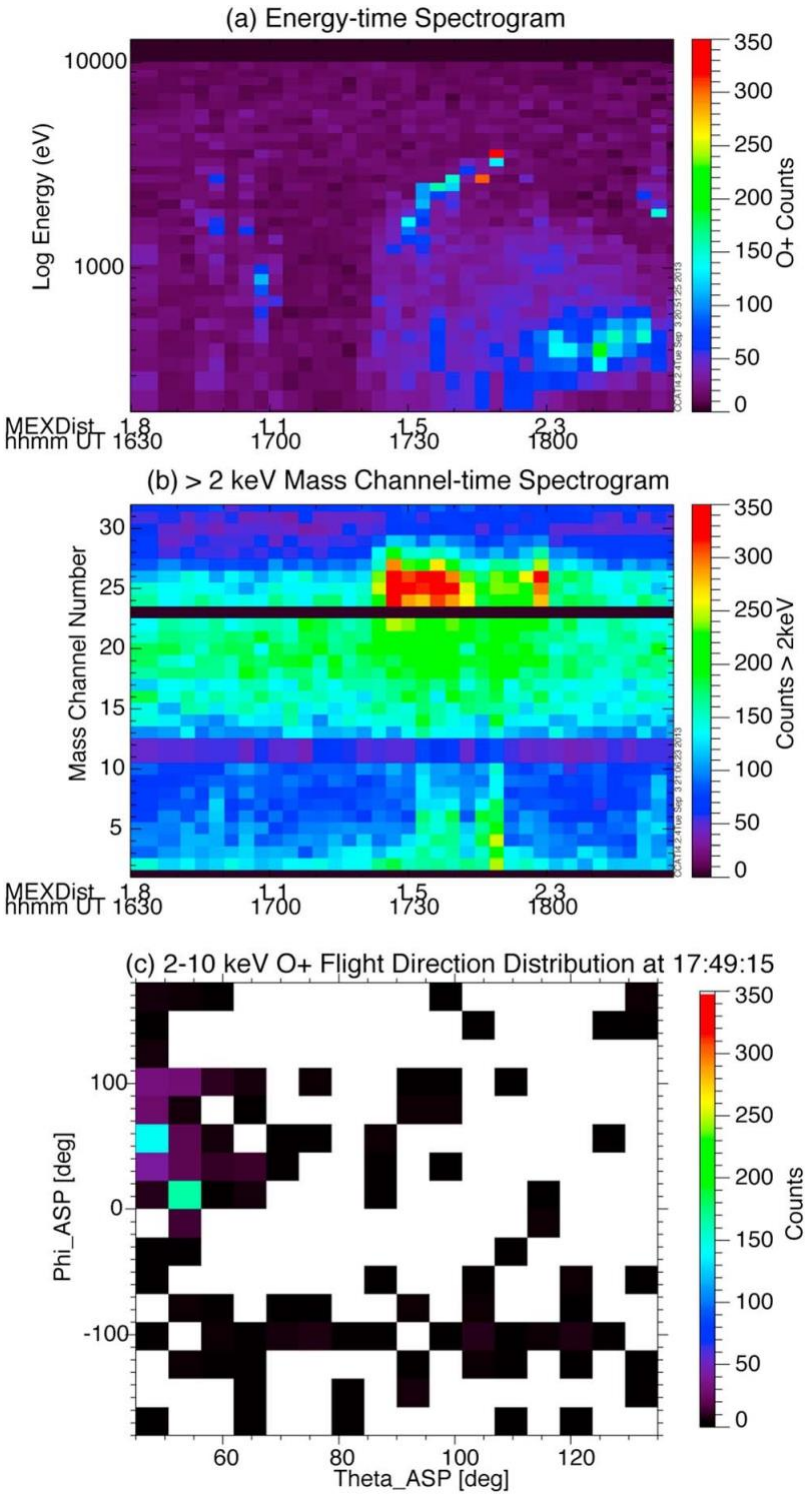

Figure 4.3. (a) Energy-time spectrogram of 2-10 keV O^+ during the 2 hour interval on October 9, 2005, integrated over all look directions. (b) Mass-time spectrogram of the same data. (c) The location of these O+ counts mapped on IMA's azimuth vs elevation angle for one specific 192-second data sweep at 17:49.

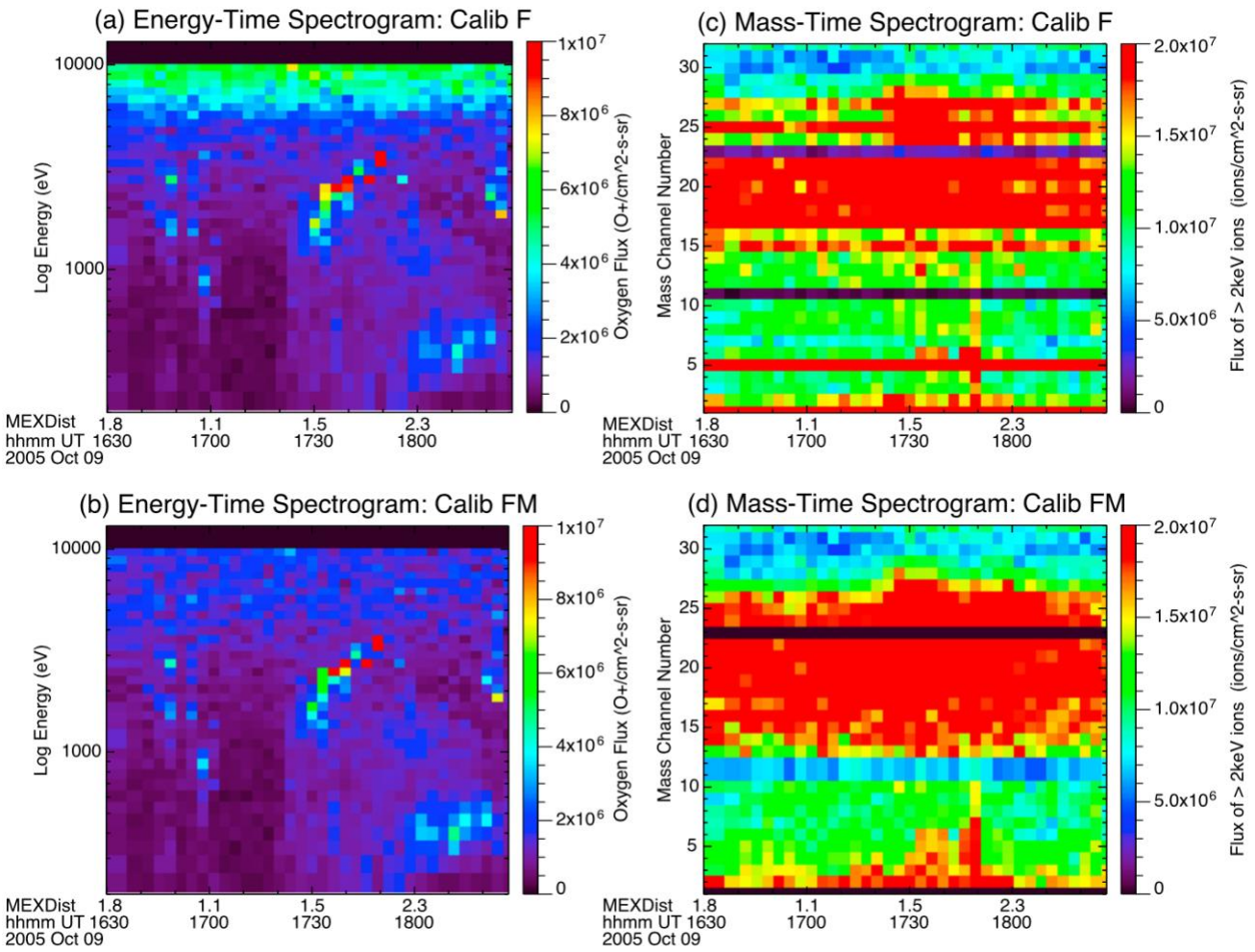

Figure 4.4. O^+ data for October 9, 2005. As in Fig. 4.3 except here units are again particle flux rather than counts. The top two panels are identical to the bottom two panels in every way other than the specific way that data has been cleaned by IMA data analysis software, with the bottom panels showing data that has undergone a more robust cleaning process to remove ghost counts and calibrate mass channels. (a) shows an energy-time spectrogram of IMA O^+ with the "standard" calibration. (b) shows an energy-time spectrogram with the enhanced calibration. (c) shows a mass-time spectrogram with standard calibration. (d) shows the same mass-time spectrogram with enhanced calibration.

Table 1. Intervals of Energetic O^+ Plume Observation When the Mars Express (MEX) Orbit Plane Was Aligned With 5° of the Mars Global Surveyor (MGS)-Derived E_{SW} Clock Angle (Measured Counterclockwise From Dusk)

Date	Start UT	End UT	UT of θ_E	Mars Solar Orbital (MSO) Dist. in R_M	Dist. to Induced Magnetospheric Boundary (IMB) in R_M	E Range in keV	θ_E	Prior θ_E	Next θ_E	In Sheath?
01 Aug 2004	04:40	04:50	04:49	1.7–1.9	0.4–0.6	2–3	197°	124°	71°	Yes
12 Dec 2004	11:00	11:50	11:46	1.5–2.8	0.2–0.3	4–7	301	214	314	Yes
15 Apr 2005	04:20	04:30	05:03	2.2–2.7	0.2–0.5	2–3	306	10	332	Maybe
03 Jun 2005	05:30	06:00	06:32	1.5–2.1	0.1–0.8	4–9	152	242	333	Yes
10 Jun 2005	05:50	06:00	05:21	2.1–2.4	0.6–0.9	2–5	351	4	151	Yes
09 Oct 2005	17:30	17:50	17:30	1.5–2.0	0.3–0.5	3–4	70	135	28	Yes
02 Apr 2006	22:30	22:50	22:43	1.3–1.5	0.0–0.2	2–4	347	26	0	Yes
10 Jul 2006	19:50	20:00	19:07	2.5–2.6	0.2–0.2	2–3	288	154	304	Maybe
23 Jul 2006	01:30	01:40	01:28	2.1–2.6	0.3–0.3	2–3	103	72	109	Yes

Table 4.1. Details for each of the individual energetic plume observations

Figures 4.1-4.4 all focused exclusively on a single event representative of what an unambiguous energetic plume sighting in MEX IMA data looks like. Table 4.1 lists relevant pieces of information concerning not just this event plus all eight other instances energetic plume observation identified in this survey. Many of the columns in the table are self-explanatory. The "Distance to Induced Magnetospheric Boundary) column simply provides the distance measured in Mars radii between the MEX position and the average location of the MPB as calculated in *Trotignon et al.* [1996]. The "Prior θ_E" and "Next θ_E" columns list the difference in E_{SW} angle in the MSO y-z plane as estimated by MGS. This is a reminder that there is significant variation in the IMF clock angle from one measurement to the next measurement taken a single two-hour MGS orbit later. This is a source of large amounts of uncertainty in these estimates for the direction of the clock angle of E_{SW}. (See Fig. 1.5 for an image of the plane in which this rotation of the IMF angle occurs and for a reminder of how clock angle is defined) . The correlations of start and end values of energy versus MSO and IMB distance are weak (0.19 and 0.43, respectively), and only the latter is statistically significant.

All nine energetic plume observations showed high count rates in the mass channels corresponding to O^+, and for all nine, plots corresponding to Figs. 4.2-4.4 were created to double-check both that the observations occurred outside of the MPB (the location of two of the events was ambiguous) and also that they represent real oxygen counts rather than ghost counts. Theta-phi matrices (such as Fig. 4.3c) of these events reveal that many of the observations are seen near the edge of the field of view of the instrument, suggesting that these blind spots are a very real obstruction to observations of the energetic plume in MEX data.

4.3 Initial Statistical Survey Methods and Results

In this survey, rather than omitting all observations that occurred when the orbit of MEX was not within 5° of the estimated E_{SW} direction, all data was used for which an estimate of E_{SW} was available. The angle between MEX and E_{SW} in the MSO y-z plane was simply saved for each 192 second data sweep so that the observations of each data sweep could be rotated around the Mars-Sun line until the ESW direction was directed vertically. This is known as Mars-Solar-Electric field (MSE) coordinates. The same (2004-2006) time interval was used for this analysis as was used for the case study. (This is the entire time of overlap after MEX arrived at Mars and before MGS stopped working). The result was that the statistical study yielded ~28,000 measurements, each measurement corresponding to one 192 second IMA sweep, or data packet. The expected result of rotating all of these observations into MSE coordinates is that a greater number of counts of these greatly accelerated O+ ions should be seen in the $+E_{SW}$ direction than in the $-E_{SW}$ direction, and that the flight direction of these ions is aligned with E_{SW}. The actual results are shown in Figure 4.5.

The black circle in each panel of Fig. 4.5 represents Mars. The view is from the sun in the MSE coordinate system, in which the estimated E_{SW} direction is aligned with the vertical axis. The spatial bins are 0.4 Mars radii, a value chosen to give some degree of spatial resolution while still retaining statistical significance (many observations per spatial bin). As was true for the case study, only observations outside of the statistical MPB were considered. There is data in the spatial bins near the center of each panel because the plots are integrated along the x direction, and the data is taken from upstream of the MPB in addition to the planet's flanks. Fig. 4.5a shows the data coverage. It would be reasonable to have expected that, upon rotation into MSE

coordinates there should be roughly even coverage of all clock angles. The asymmetric coverage is due to the fact that the orbit of MEX during this 2-year time period did not evenly sample all clock angles, combined with the fact that one direction for E_{SW} was estimated to have occurred far more often than others. In the energetic O^+ median count rate data shown in panel b, no statistical plume is visible. It can be seen that the median count rate appears to be higher at larger cylindrical distances from the Mars-Sun line. A possible (even likely) explanation for this is that one of the most common ways for ions to enter the high (2-5 keV) energy range considered is for them to have been accelerated in the direction of E for some distance. If this is the case, it may be that energetic plume ions are shown in this panel, but the estimate for the direction of E_{SW} is simply unreliable. Fig. 4.5c depicts normalized frequency of observed count rates. This panel shows which spatial bins were most likely to see a particularly high number of O^+ counts. This approach was inspired by the understanding that the energetic plume tends to be comprised of large number of ions accelerated together. Still, it seems a stretch to say that these high count rates are seen in this panel to occur more in the E_{SW} direction (upward on the vertical axis). The occurrence of high O^+ counts does not appear here to be restricted to the $+E_{SW}$ direction. Practically the only hints of the expected energetic plume based asymmetries are seen in the velocity vectors overplotted on Fig 4.5c, which may point more upward than down.

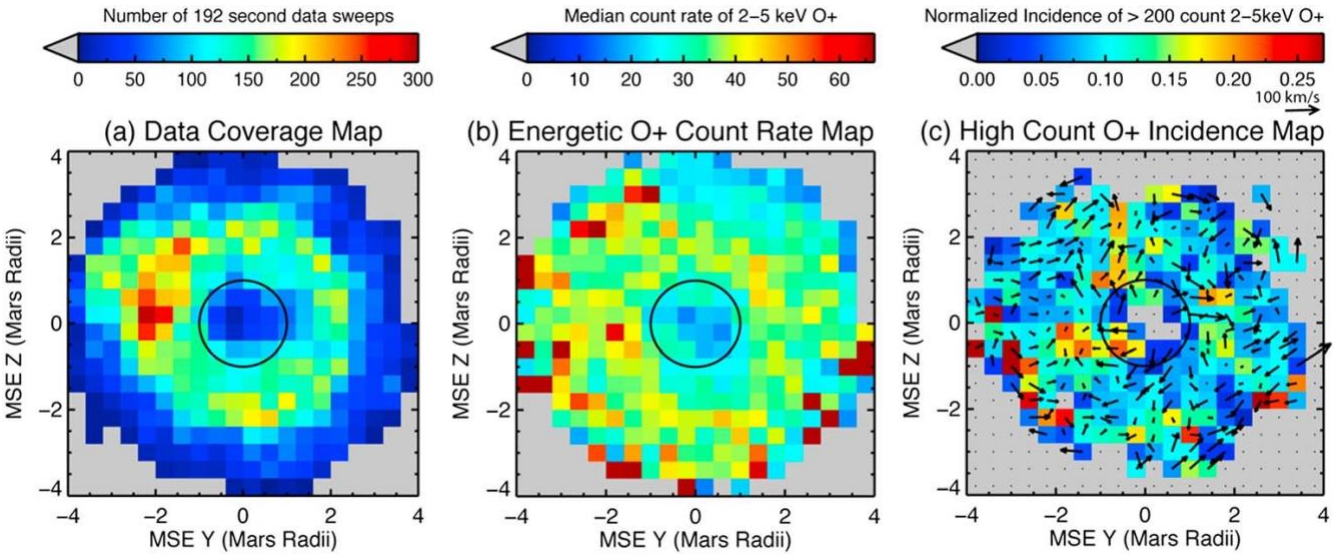

Figure 4.5. Results of the survey of all IMA data for which an MGS-derived estimate of the direction of E_{SW} is available. All panels are in MSE coordinates, in which E_{SW} is aligned with the vertical axis, and all panels show the view from the sun. Values are integrated along x coordinate. (a) shows the number of observations in each spatial bin. (b) median count rate of 2-5 keV O^+. (c) incidence rate, or occurrence frequency, of > 200 counts of 2-5 keV O^+. Arrows show projections of average velocities of O^+ in this energy range.

4.4 Chapter Discussion and Conclusions

The case study showed that it is certainly possible to identify observations of heavy ions escaping from the atmosphere of Mars that match simulations of the energetic plume in all respects. Here's a checklist: Located outside the MPB? Check. Located near the terminator lane? Check. Located in AND flowing in the estimated direction of E_{SW}? Check. Check. Accelerated to high energies? Check. Exhibiting higher energies as the spacecraft observation location moves further from the planet? Check. The results of the initial statistical survey that followed, however, throws a wrench into things. The observations shown in Fig. 4.5 suggest that the selection of times when MEX was located in the direction of E_{SW} was perhaps not why the case study succeeded in finding plume type ions. Perhaps a few such cases would have been found at any clock angle that might have been chosen.

Observation of the energetic plume in MEX data proves difficult. Some of the reasons for this were discussed in chapter 3. The field of view is inconveniently situated at or near the look direction to observe energetic plume ions, the presence of ghost counts interferes with the exclusive detection of heavy ions, and the lack of direct observations of the IMF adds a large degree of uncertainty to the estimated direction of E_{SW}. Here we offer a reminder that the uncertainty in the direction of E_{SW} is due to at least two separate factors. First, the observed field at 400km may be affected by crustal magnetic fields and induced ionospheric currents that bend the net field line as IMF drapes around the planet. Second, as was shown in Table 4.1, the IMF clock angle is time-varying, and there was often significant change in the observed angle at 400km from one MGS orbit to the next two hours later. The median change in observed angle from one measurement to the next was 44°. Another possible explanation of why the case study seemed so successful while the statistical survey was resoundingly inconclusive may be in the level of automation in the methodology. In the case study, plume type observations were picked out manually, whereas in the statistical survey the large size of the dataset made it impossible to screen out low quality observations. For instance, noise-dominated observations could be classified as times of high-count rates of O^+, negatively influencing the results.

The dubious results of the statistical study could not, of course, be said to invalidate models' predictions (even prior to the hindsight possessed by the author at the time of the writing of this dissertation). But neither could it be said that the results validated the models. One positive outcome of this initial statistical study, however, was that the process helped to generate ideas to improve such a study, even with the same imperfect data sets:

- Suppose a system were put in place to better shield statistical results from ghost counts nearly as effectively as the case study results were shielded from ghost counts manually and painstakingly
- Suppose a more justifiable (less arbitrary) means of determining what constitutes “high” count rates of energetic O^+ were developed
- Suppose the observations included in a statistical study were limited in a way that reduces uncertainty due to the time variation of the IMF

A more reliable statistical study was in the works.

Chapter 5: Better, Slower, Stronger: A New Study of the Energetic Plume as Seen by MEX

This study obtains a statistical representation of 2-15 keV heavy ions outside of the Martian Induced Magnetosphere and depicts their organization by the solar wind convective electric field (E_{SW}). The overlap in the lifetime of Mars Global Surveyor (MGS) and Mars Express (MEX) provides a period of nearly three years during which magnetometer data from MGS can be used to estimate the direction of E_{SW} in order to better interpret MEX ion data. In this study we use MGS estimates of E_{SW} to express MEX ion measurements in Mars-Sun-Electric field (MSE) coordinates. A new methodological technique used in this study is the limitation of the analysis to a particular instrument mode for which the overlap between proton contamination and plume observations is rare. This allows for confident energetic heavy ion identification outside the induced magnetosphere boundary. On the dayside, we observe high count rates of 2-15 keV heavy ions more frequently in the $+E_{SW}$ hemisphere ($+Z_{MSE}$) than in the $-E_{SW}$ hemisphere, but on the nightside the reverse asymmetry was found. The results are consistent with planetary origin ions being picked up by the solar wind convective electric field. Though the orientation of IMA's 360° by 90° field of view hinders quantification of plume fluxes and velocity space, this new energetic heavy ion identification technique means that Mars Express should prove useful in expanding the time period available to assess general plume loss variation with drivers.

5.1 Methodological Improvements

The solution to the problem of ghost counts in a statistical survey came from a colleague in Kiruna, Robin Ramstad. Robin was able to provide the plot seen in Fig 3.2. Fig 3.2a demonstrates that if a statistical study were restricted to times when IMA was using a post acceleration voltage of 2400V, a mass and energy range for the study could be selected (circled region of Fig. 3.2a) that meets two crucial criteria. First, it is a mass and energy range that avoids the vast majority of ghost counts. Second, it is a mass and energy well representative of the energetic plume. An instrumental effect had an instrumental solution. Note that the increased mass range chosen in this process means that throughout this chapter's study the planetary ions considered are no longer O^+ specifically, but the broader term "heavy ions," which for our purposes refers predominantly to O^+ and O_2^+, but it is likely that there is some CO_2^+ in the results as well. The energy range considered was also broadened. This study considers ions in the 2-15 keV range.

The solution to the problem of having used an arbitrary cutoff for what was considered to be a significant or "high" count rate of heavy ions came from the realization that the distribution of heavy energetic ion counts in IMA exhibit a two-humped shape. Figure 5.1 shows that the distribution of count rates is bimodal, with most of the 8,000 IMA sweeps included in this study having either less than 40 counts or between ~70-130 counts. The times with fewer than 40 counts are times when the heavy ions measured are scattered across the IMA's 16 by 16 angular pixel field. IMA sweeps falling within the 2nd peak also exhibit this scattered signature, but in addition to the scattered signature, these times see a large number of ions entering IMA from the same look direction, more than from all other look directions combined. The first peak represents

the typical background level of counts, whereas the 2nd peak tends to correspond to times when a focused of beam with significant counts is present. Therefore, when we talk about the incidence rate of "high" counts of 2-15 keV heavy ions, this may also be thought of as the occurrence frequency of heavy ion beams.

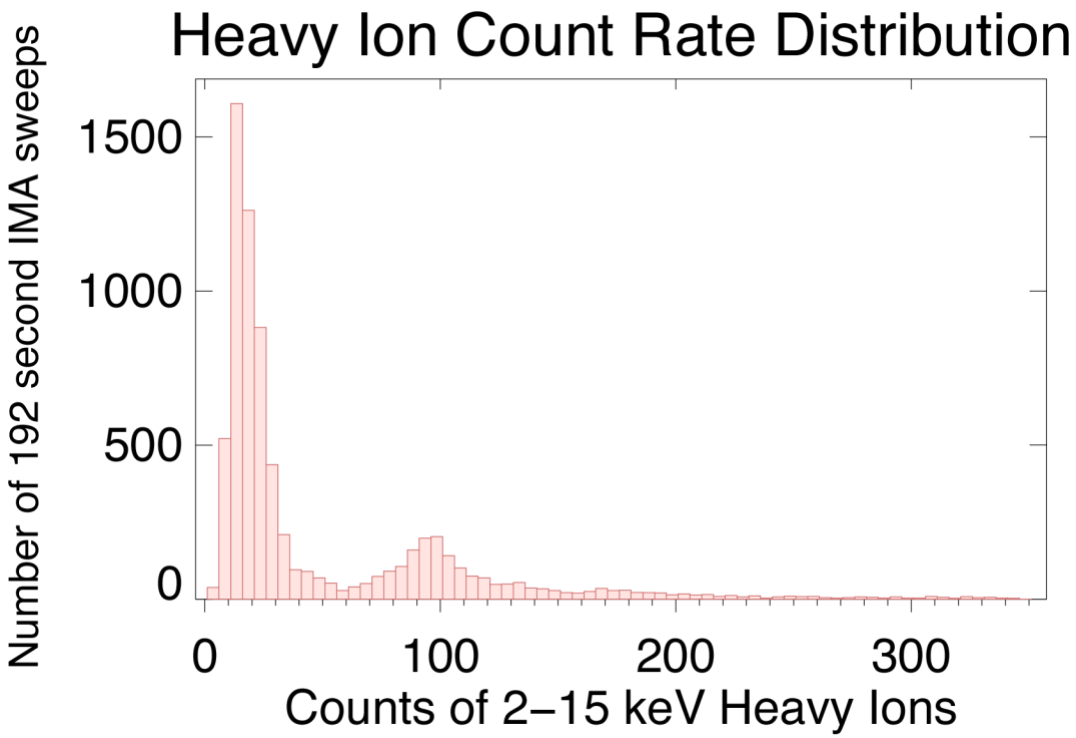

Figure 5.1. This histogram shows the number of IMA sweeps (vertical axis) that detected a given number of counts of 2-15keV heavy ions (horizontal axis). For most sweeps, the count rate was between 10 and 50. A count rate greater than 70 is considered to be "high counts" for the purposes of this study.

To find a partial solution to the increased uncertainty in the estimated direction of E_{SW} due to time variation of the IMF, two options were tested. First, signatures of a statistical energetic plume were searched for in a survey that was restricted to MEX observations that occurred within a twenty-minute window of each of MGS's estimates of the direction of E_{SW}. Next, signatures of the plume were searched for in a survey that included the entire hour before and

after each MGS estimate, but only utilized those 2 hour periods centered around MGS observations for which the clock angle was within 15° of the previous observation and also within 15° of the next observation. The early results of these two distinct methods of lessening the negative effects of the time variation of the IMF were quite clear. The second method resulted in a much better organization of ion observations in MSE coordinates. The choice was therefore made to limit the full statistical study to times of "steady" IMF, i.e. times when there was little change in IMF clock angle between three consecutive 2-hour cadence MGS estimates of E_{SW}.

5.2 Methodological Summary

To explore the role of the convective electric field in organizing heavy ions originating from the Martian upper atmosphere, ion data is combined with magnetic field data. The ion data were detected by the Ion Mass Analyzer (IMA) that is part of the Analyzer of Space Plasma and Energetic Atoms (ASPERA-3) instrument suite aboard MEX. Detailed descriptions of the ASPERA-3 instruments can be found in *Barabash et al.* [2004, 2006]. We exclude data from times when MEX was inside the IMB. The most precise way to isolate time intervals outside the IMB would be to identify boundary crossings for each orbit, but given the large quantity of data we chose the more practical method of automatically selecting times when MEX was outside of an average IMB location estimated empirically by *Vignes et al*. [2000]. The direction of the convective electric field was estimated using magnetometer (MAG) data from MGS. A histogram of the estimated clock angle of E_{SW} is shown in Fig. 5.2. The clustering of E_{SW} clock angle values around 330° corresponds to the clustering of IMF draping angles around 240° discussed in *Brain et al.* [2006], and indicates a systematic error in this proxy, which will be

brought up again in the discussion. Here, we simply ask readers to keep in mind as they view the figures that the site from which we downloaded this draping proxy warns that it is not thought to be more accurate than ~90°. For this reason, our analysis consists of coarse comparisons of MSE hemispheres and quadrants (quarter-cylinders) despite the modeled energetic plume often appearing narrowly focused in the direction of E.

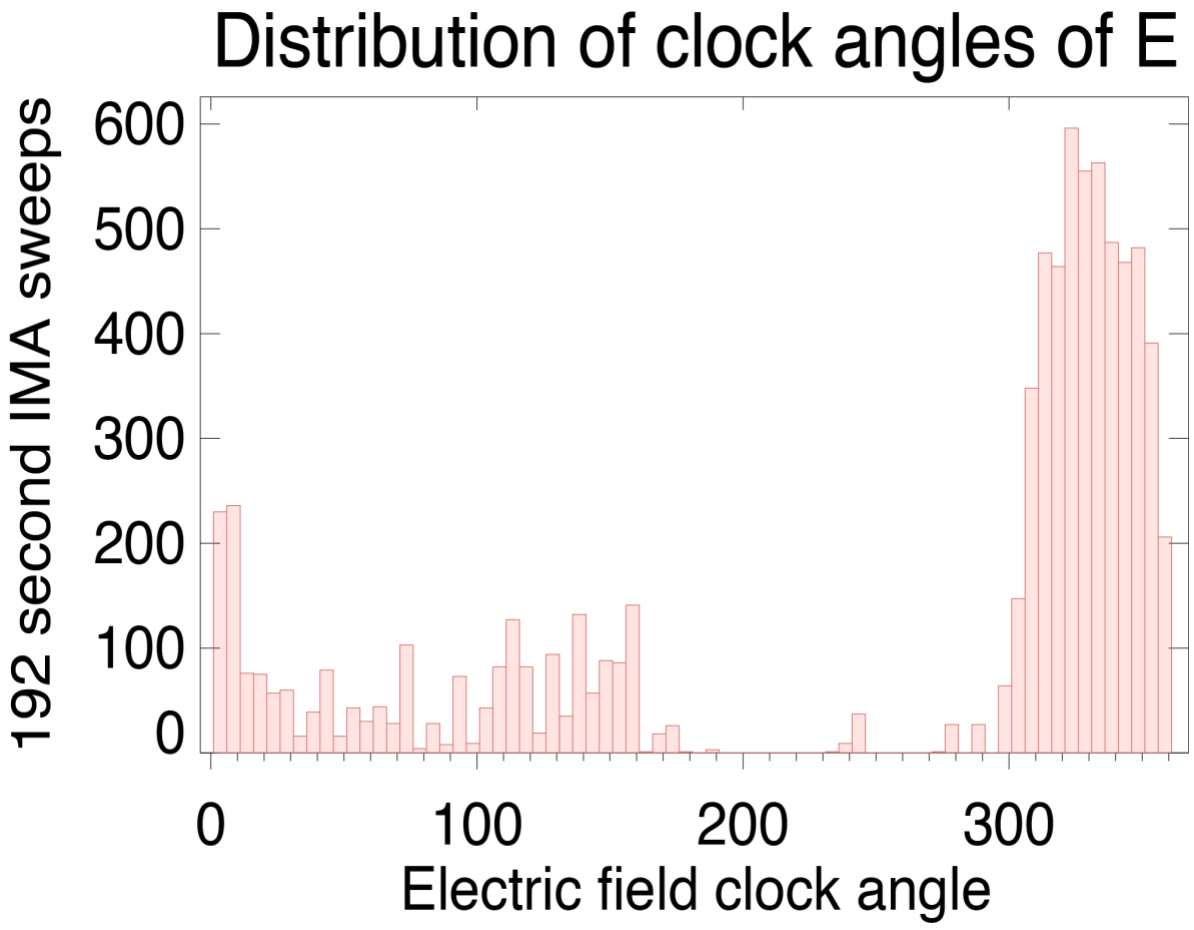

Figure 5.2. Histogram showing the distribution of clock angles estimated from MGS draping angle proxy. The angle is defined counterclockwise from local east. The large peak at a convective electric field angle of around 330 degrees corresponds to the clustering of IMF draping angles at 240 degrees as discussed in *Brain et al.* [2006], and explains the asymmetry in data coverage seen here in Fig. 5.3.

After excluding times when MEX was inside the MPB, excluding times when IMA was not using the post acceleration voltage now known to be best for limiting ghost counts, and excluding the large number of time intervals when the unsteadiness of the upstream IMF reduced the reliability of MGS estimates of upstream IMF clock angle, the number of IMA sweeps was much smaller than what appeared in the previous statistical study, but this remaining data is also much cleaner. The resulting data set consists of about 8000 192-second-long IMA sweeps from times when MEX was outside the model IMB and IMA was switched on and using the 2400V post acceleration voltage and the IMF clock angle was steady. In our results, ion locations and flight directions have been transformed into the Mars-Sun-Electric field (MSE) coordinate system by rotating around the MSO x-axis until the z axis was parallel to the direction of the convective electric field.

A map of the data coverage around Mars in MSE coordinates is shown in Figure 5.3. The circle represents the planet, and the curves in panel (b) represent average locations of the IMB and bow shock as estimated by *Vignes et al.* [2000]. Panel (a) shows the view from the Sun, integrating over all X for which there was data available, with Y_{MSE} on the horizontal axis and Z_{MSE} on the vertical axis. This panel highlights the fact that not all clock angles of the IMF are evenly sampled. MEX was most often in the $-Y_{MSE}$ and $+Z_{MSE}$ hemispheres. In principle, this uneven sampling in MSE coordinates should not occur, as Mars is expected to spend a roughly equal amount of time in the toward and away sectors of the solar wind over the course of two and a half years. The sampling asymmetry is explained by the distribution of the E_{SW} proxy shown in Fig. 5.2. Due to the large clustering of E_{SW} values, transformation into the MSE system rotates but partially preserves the MSO clustering of MEX's position during this time. Panel (b) shows

the X-Z_{MSE}-plane, where we have integrated over Y_{MSE} from -4 to +4 Mars radii. Note that values appear "inside" of the projection. All measurements included in this study are outside of the *Vignes et al.* [2000] IMB location. It should be noted that most of the data taken in the $-E_{SW}$ hemisphere is on the dayside, whereas in the $+E_{SW}$ hemisphere, the region most heavily sampled is slightly downtail of the X=0 plane. Therefore if we used only a view from the sun projected onto a plane, it would be difficult to determine whether differences seen between the $+E_{SW}$ and -E_{SW} hemispheres are actually due to asymmetries caused by the direction of E_{SW} or whether such differences are due to data from these separate hemispheres being dominated by different regions along the Mars-Sun line. For this reason, some separate analyses have been performed for dayside and for nightside.

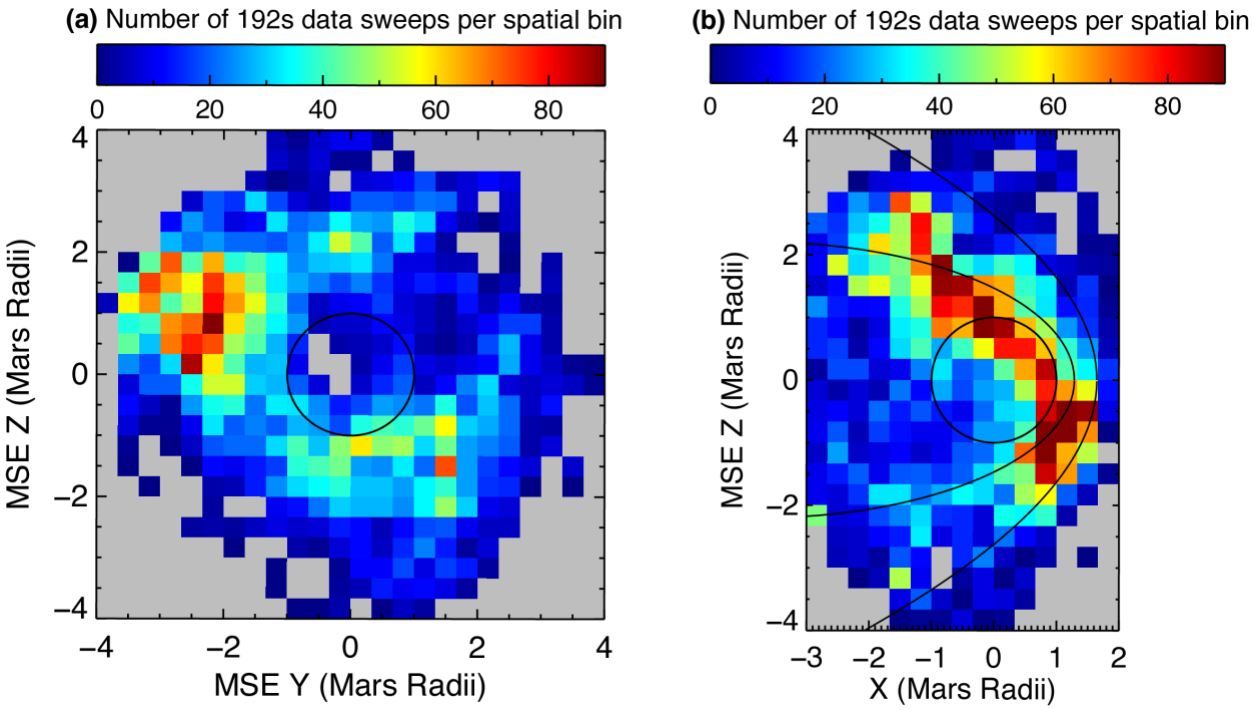

Figure 5.3. Coverage of the data used in this study in MSE coordinates, with the direction of the convective electric field directed upward along the vertical axis. Panel (a) shows the x-integrated coverage as viewed from the sun, and panel (b) shows the y-integrated coverage. The circle

represents Mars and the curves are average locations of the bow shock and IMB. The color of each bin indicates how many times that region was sampled.

5.3 Statistical Survey Results

Figure 5.4 is a map of the incidence rate (occurrence frequency) of significant counts of 2-15 keV heavy ions. By "high counts" here, we mean values above 70. As will be discussed below, a count rate of 70 or more is an indication that a physically meaningful presence of heavy ions was observed by MEX IMA, above any background level of noise count rate. The incidence rate of the high-count observations is a value from 0 to 1, with values approaching 1 indicating that a significant number of heavy ions are observed on nearly every 192-s IMA sweep. For example, an incidence rate of 0.6 means that for 60% of all 192-s IMA sweeps in that spatial bin, the integrated counts of heavy ions across all instrument look directions within the 2-15 keV energy range was at least 70. For statistical significance, we have also limited the values shown in Fig. 5.4 to only those spatial bins with more than 20 MEX IMA sweeps. These maps use the same MSE coordinate system used in Fig. 5.3, with (a) showing the view from the sun and (b) showing the X-Z_{MSE} plane.

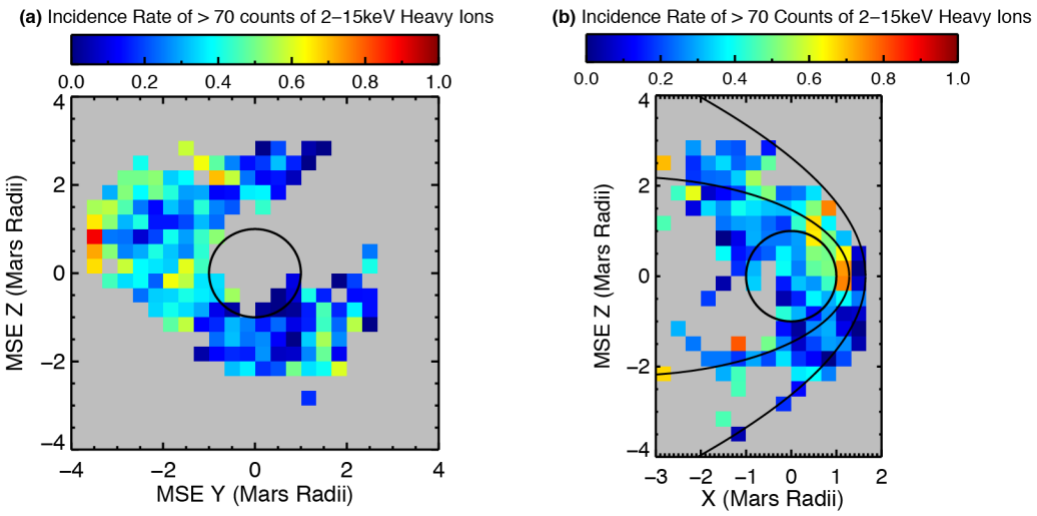

Figure 5.4. Incidence rate of high counts. Panel (a) and is integrated along x. Panel (b) is integrated along y. The color of each spatial bin denotes the fraction of the total number of data samples in that bin in with a count rate > 70. Spatial bins with less than 20 measurements appear in grey.

Fig. 5.4 (a) does not seem to show a clear trend of there being increased count rates of energetic heavy ions in the $+E_{SW}$ direction. It does indicate, however, that it is rare to see large numbers of these ions in the $-E_{SW}$ direction. Panel (b) reveals that if we integrate over all Y_{MSE}, it becomes clear that, on the dayside, the $+E_{SW}$ hemisphere has a far greater incidence rate of high counts than the $-E_{SW}$ hemisphere. To ease comparison between the hemispheres, Fig. 5.5 shows the difference between the incidence rate in each spatial bin in the +Esw hemisphere and the corresponding spatial bin in the –Esw hemisphere. Hence, positive values (red) indicate regions with a higher incidence rate of energetic heavy ion events in the $+E_{SW}$ hemisphere and negative values (blue) indicate regions where it was more common to observe energetic heavy ions in the $-E_{SW}$ hemisphere. Spatial bins for which at least one hemisphere had fewer than 20 measurements appear grey. Maps with fuller spatial coverage than what is seen in Figs. 5.4, 5.5, and 5.6 were also created. These maps include reproductions of these maps that color every spatial bin with at least one measurement, and the trends present in those plots were in line with what can be seen in Figs. 5.4, 5.5, and 5.6. Both on the dayside and in the terminator region there is a higher incidence rate in the $+E_{SW}$ hemisphere. In a few locations on the nightside there were actually more incidences of high counts in the $-E_{SW}$ hemisphere, however these $-E_{SW}$ hemisphere enhancements may not be significant, as will be seen in further analysis below.

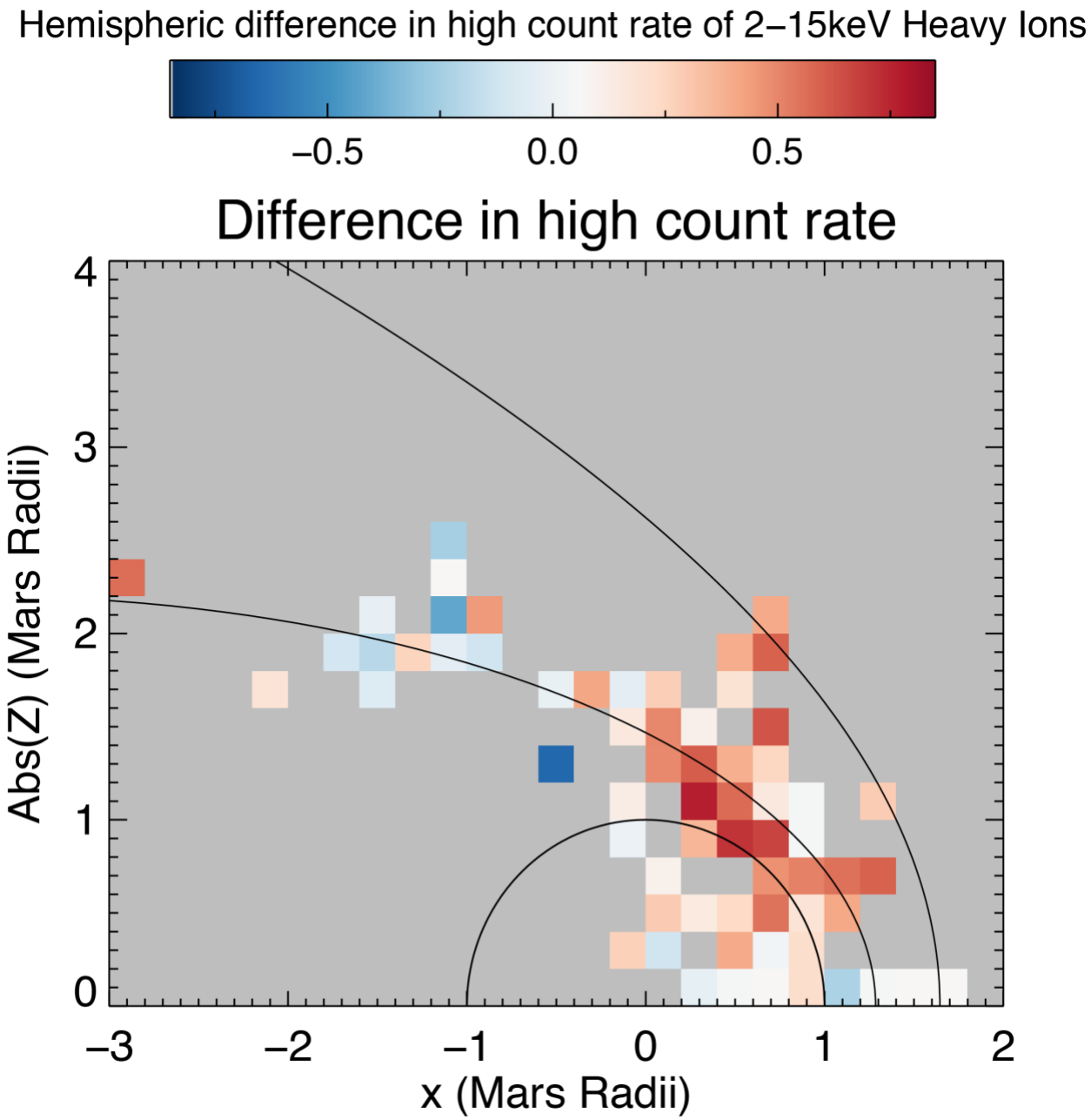

Figure 5.5. Difference in incidence rate of high counts between the + E_{SW} and – E_{SW} hemispheres. The vertical axis is the absolute value of Z_{MSE}. The color represents the incidence rate of high counts in the + E_{SW} direction minus the incidence rate of high counts in the corresponding spatial bin in the – E_{SW} direction. Spatial bins for which there were not at least 10 samples of data from the + E_{SW} hemisphere and at least 10 samples of data from the – E_{SW} hemisphere appear grey. Data has been integrated along y prior to calculating the difference.

When examining the plots depicting the occurrence frequency of "high" counts during a 192s data sweep, recall that the cutoff of 70 or more being considered "high" is not arbitrary. Rather,

it is a value that can be read directly off of Fig. 5.1. A close inspection of Fig. 5.4 reveals that the dayside region of high incidence of > 70 counts (seen in yellow and orange in Fig. 5.4 b) may be caused primarily by a projection of measurements taken in the $-Y_{MSE}$ sector (panel a) onto the plane of the plot in panel b. What would happen if we prevented these Y_{MSE} sector measurements from impacting the results? To answer this question, in addition to comparing the $+E_{SW}$ and $-E_{SW}$ hemispheres, data was sorted into quadrants, with all measurements taken within +/- 45˚ of the direction of E_{SW} categorized as belonging to the $+Z_{MSE}$ quadrant, and all measurements taken more than 135˚ from the direction of E_{SW} falling into the $-Z_{MSE}$ quadrant. Fig. 5.6 shows the incidence rate of high counts in cylindrical coordinates, with panel (a) showing the $-Z_{MSE}$ quadrant, or quarter-cylinder, and panel (b) showing the $+Z_{MSE}$ quadrant. The use of a cylindrical coordinate system here makes it more readily apparent than in previous figures that all of the data are confined to locations beyond the *Vignes et al.* [2000] IMB location, which is shown on the plot. The results look similar to what was seen when comparing hemispheres. On the dayside, MEX was more likely to see high counts when in the $+Z_{MSE}$ quadrant, while on the nightside it appears that MEX was more likely to see a high count rate the $-Z_{MSE}$ quadrant.

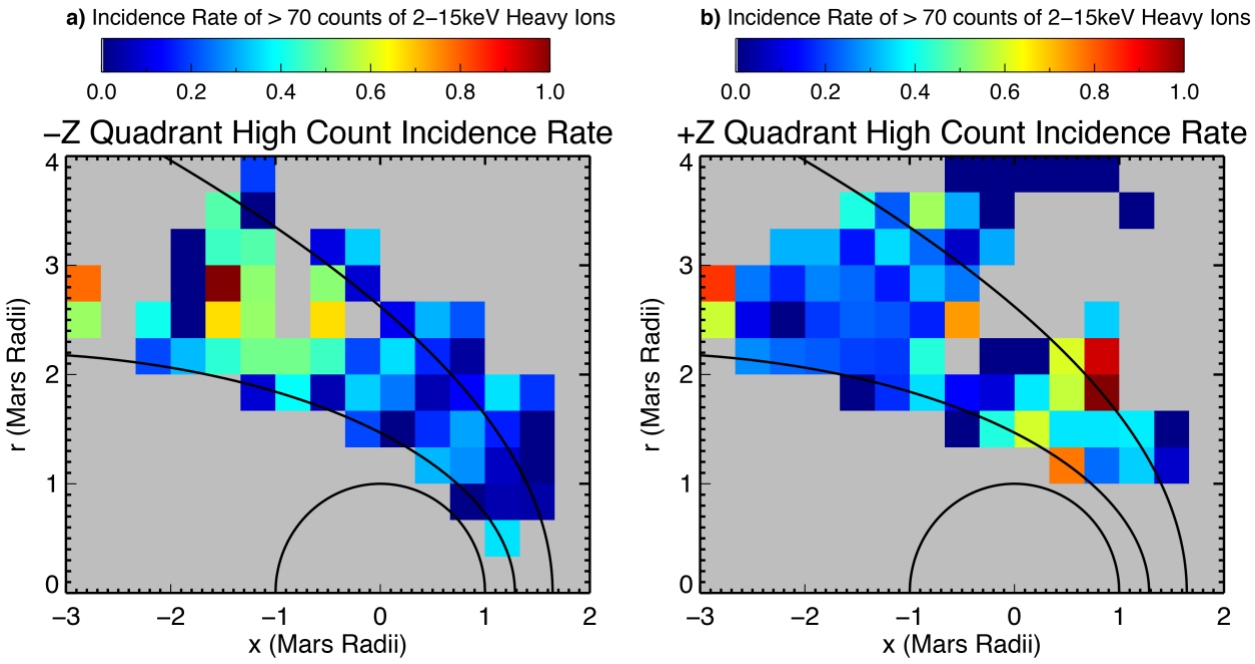

Figure 5.6. Incidence rate of high counts in the $-Z_{MSE}$ quadrant (left) and in the $+Z_{MSE}$ quadrant (right) in cylindrical coordinates. The color of each spatial bin denotes the likelihood of measurements taken there having greater than 70 counts of 2-15keV heavy ions. Spatial bins for which there were not at least 10 measurements in this quadrant appear in grey.

To quantify the differences between quadrants, cumulative probability distributions were created to show what proportion of the time the count rate exceeded any given value. Figure 5.7 presents such cumulative probability distributions, comparing the $+Z_{MSE}$ and $-Z_{MSE}$ quadrants on the nightside (panel a) and on the dayside (panel b). The thicker lines show the occurrence frequency, or incidence rate, of high-count events versus the range of possible count limits that might have been used to define what is meant by "high counts". The portions of the cumulative probability distribution with steep slopes correspond to count rates that occur more frequently, as seen in the histogram (Fig 5.1). The flat (horizontal) portions of the probability distribution correspond to low points in the histogram. The thin lines in Fig. 5.7 represent 90% confidence windows. As the count rate cutoff increases, the number of IMA sweeps with counts exceeding this cutoff falls rapidly, greatly decreasing the degree of certainty surrounding this cutoff's

occurrence frequency, leading to wider confidence windows. As expected, Fig. 5.7 (b) demonstrates that, on the dayside, the $+Z_{MSE}$ quadrant saw a greater occurrence frequency of heavy energetic ions than did the $-Z_{MSE}$ quadrant. Fig. 5.7 (a) reveals that narrowing our focus to opposite quadrants retains the unexpected reverse asymmetry seen on the nightside, with the nightside seeing a slight preference for high count rates in $-Z_{MSE}$ quadrant rather than $+Z_{MSE}$ quadrant, but the overlapping confidence windows suggest that this might be due to a limited amount of data. The confidence windows for the dayside panel in Fig. 5.7(b) don't overlap until reaching extremely rare high rates, indicating that the dayside asymmetry, more heavy ions in the direction of E_{SW}, is much more certain. It should be noted that the confidence windows only represent the uncertainty due to counting statistics. In other words, if we were 100% certain that all estimates of the IMF direction were correct, *and* 100% certain that all heavy ions actually present were detected and that there were no false heavy ion counts, *and* if spatial coverage were even (no patches without data), then we could say with 90% confidence that the true probability distribution lies within this confidence window. These confidence windows allow us to see that for count rates that are sufficiently rare (count rates greater than about 200), the uncertainty due to the small amount of data becomes quite large.

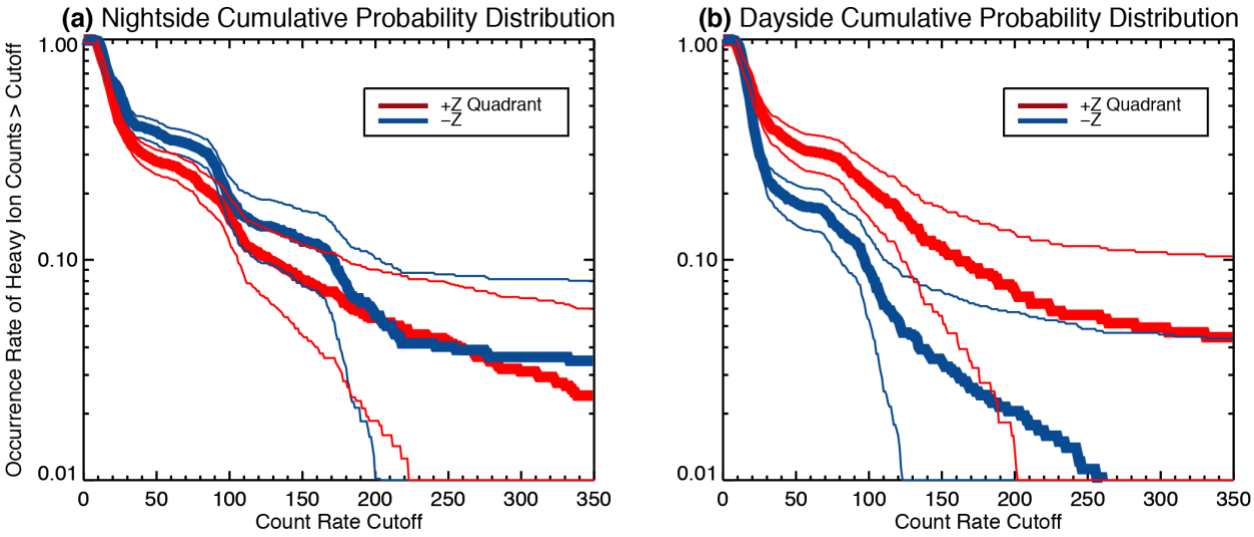

Figure 5.7. Cumulative probability distributions of 2-15keV heavy ions outside the Mars IMB for the nightside (a) and dayside (b). The red line shows the probability distribution of the $+Z_{MSE}$ quadrant (quarter-cylinder), and the blue line shows the distribution for the $-Z_{MSE}$ quadrant. The vertical axis shows the proportion of IMA sweeps for which the count rate exceeded the cutoff indicated on the horizontal axis. The higher the cutoff, the smaller the proportion of IMA sweeps exceeding this threshold, causing the lines to slope down monatonically. Thin lines are 90% confidence windows based on counting statistics.

An additional approach to presenting the E_{SW}-based asymmetry seen by MEX is shown in Figure 5.8, where a cylindrical coordinate system is employed in conjunction with units of particle flux. As in Fig. 5.6, the coordinate system in Fig. 5.8 divides the space around Mars into $+Z_{MSE}$ and $-Z_{MSE}$ quadrants, with data integrated along curves of constant cylindrical radius. The colorscale now shows particle flux (rather than counts), with arrows indicating direction and color indicating magnitude. Fluxes are integrated over all look directions, showing omnidirectional flux with units of ions per second per cm^2. The direction arrows show an average of two components of the flow for all IMA sweeps in that spatial bin, averaging the radial component and the longitudinal component, while ignoring the azimuthal velocity component in this calculation. The method used to calculate these fluxes is the same as that used in *Nilsson et al.* [2011]. Binning by energy, spatial location, and flight angle in cylindrical coordinates is used,

with average flux calculated separately for each bin so that uneven sampling of flight direction does not influence results. A full description of this technique can be found in *Fraenz et al.* [2015]. The arrows show a general motion away from the subsolar location and an upward-outward motion in the $+E_{sw}$ nightside. Other locations have seemingly random flow directions. This is addressed in the discussion section.

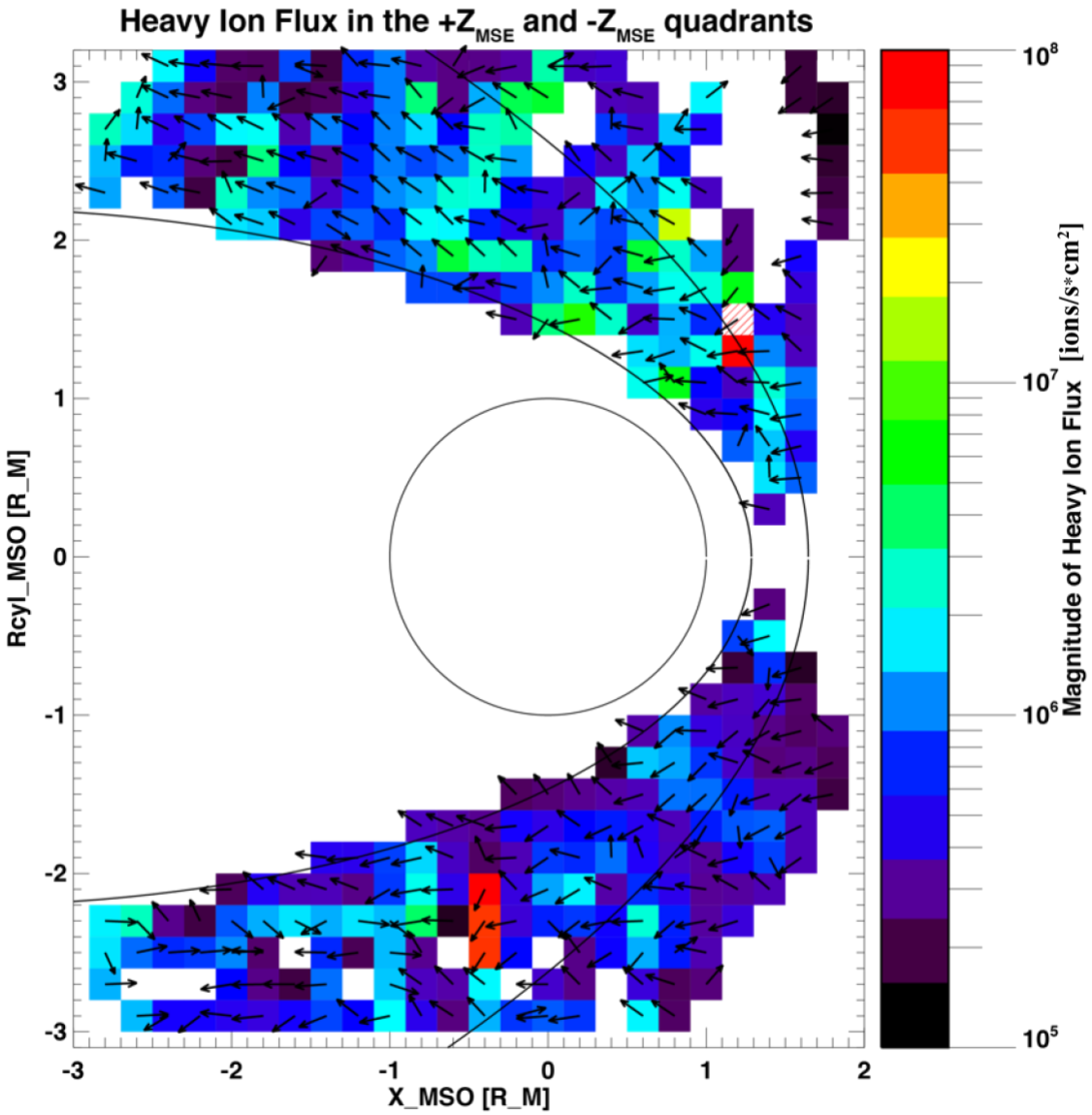

Figure 5.8. 2-15keV heavy ion particle flux magnitude (color) and direction (arrows). The coordinate system used is the equivalent of two quarter-cylinders, where data has been sorted into $+Z_{MSE}$ (top half) and $-Z_{MSE}$ (bottom half) quadrants before integration along curves of constant $radius_{cyl}$.

The color bar in Fig. 5.8 has been tweaked to highlight the hemispheric asymmetry, but just as was done in Fig. 5.5, a difference plot has been provided to make comparison between hemispheres even easier. In Figure 5.9, which uses the same coordinate system as Fig. 5.8, flux values from the $-E_{SW}$ hemisphere have been subtracted from flux values from the corresponding spatial bin in the $+E_{SW}$ cylindrical hemisphere. Red spatial bins indicate regions in which the $+E_{SW}$ hemisphere experienced higher mean particle fluxes of heavy ions than did the $-E_{SW}$ hemisphere, while blue colors represent regions in which the mean fluxes in the $-E_{SW}$ hemisphere were larger. The large dayside region where red dominates indicates higher fluxes of heavy energetic ions in the $+E_{SW}$ hemisphere located where hybrid and particle tracking models have predicted the energetic plume to be (e.g. *Fang et al*., 2008). The hemispheres seem far

more similar on the nightside, perhaps even with an indication of slightly higher fluxes measured by MEX in the near-terminator nightside, as seen in Fig. 5.5.

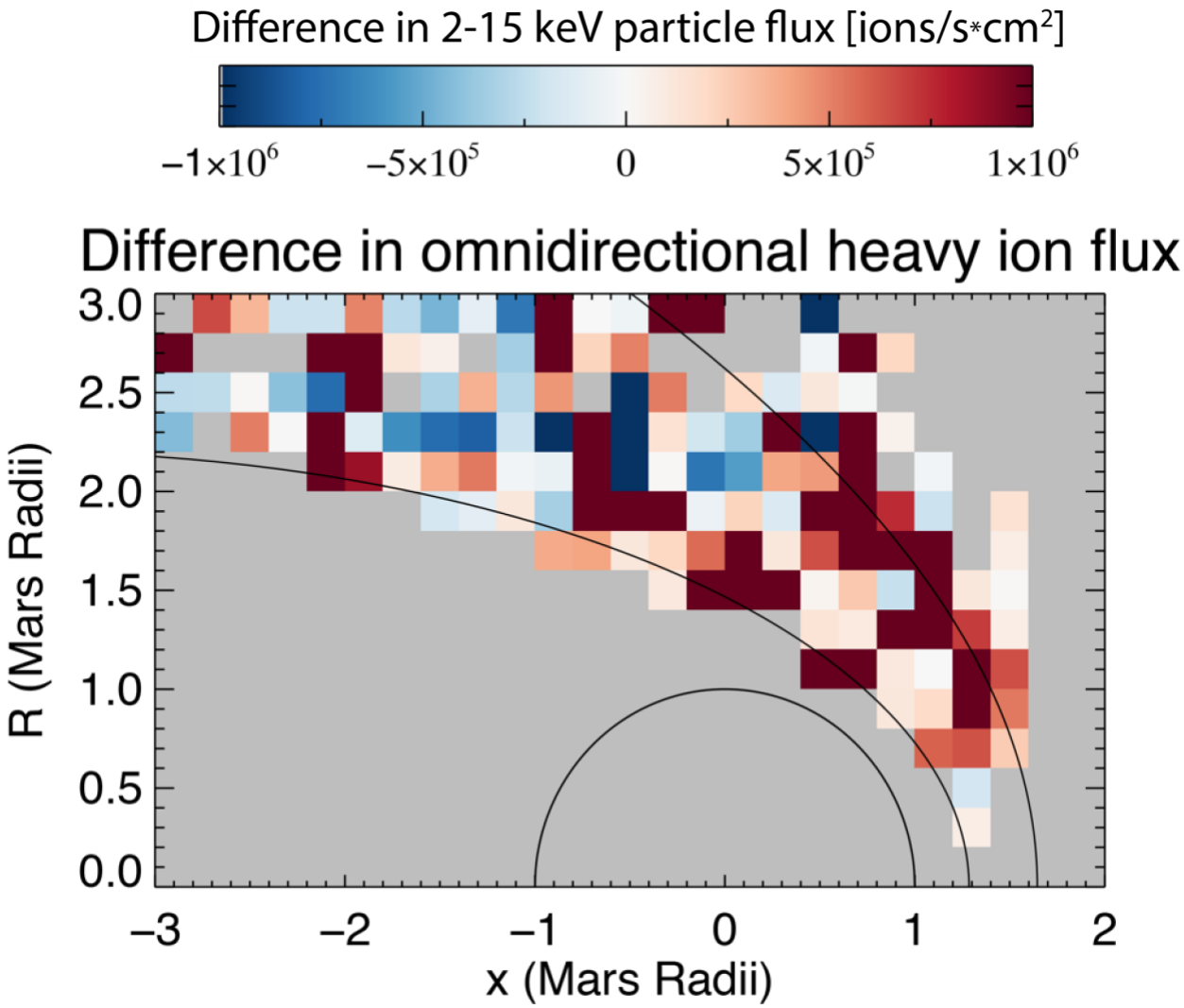

Figure 5.9. Difference in magnitude of 2-15keV heavy ion particle flux. The coordinate system is the same as that used for Fig. 5.8. Flux values from the $-Z_{sw}$ quadrant have been subtracted from flux values from the corresponding location in the $+Z_{sw}$ quadrant, so that negative values (blue) represent locations where the mean flux was greater in the $-Z_{sw}$ quadrant, while positive values (red) represent locations where there was greater flux in the $+Z_{sw}$ quadrant.

5.4 Statistical Survey Discussion and Conclusions

The results presented above indicate that on the dayside there is a clear + E_{SW} preference for observation of 2-15 keV heavy ions. On the nightside, this was not seen. This is in general agreement with the numerical models that predict a focused energetic plume of planetary ions escaping from Mars in the direction of the solar wind convective electric field.

It is interesting to see the much larger degree of success this survey had than did the statistical survey at the end of chapter 4. This can be readily explained, however, by taking into account the differences between the two methodologies of the surveys. First, the selection criterion with respect to E_{SW} is different. The present study only uses the MEX ion data if the clock angle is "steady," as defined above. Second, the criterion with respect to what is considered "high counts" is different. The former study chose a cutoff of 200 counts to be classified as a significant observation of planetary ions, while the present study uses the more defensible value based on the bimodal distribution of count rates (i.e., 70). Third, the criterion with respect to number of IMA sweeps in the presentation of the incidence rates is different. The former study has no lower threshold for including the value for a particular spatial bin, while the present study requires a minimum of 20 measurements in a spatial bin before it is shown in Fig. 5.4. Fourth, the exclusion of data from times when IMA was using a post acceleration voltage that sees more ghost counts in the relevant mass and energy ranges was instrumental in improving confidence that ghost counts do not have a major impact on the results. Fifth and finally, the plot-style presentation of the results is made differently. The former study only considered the X-integrated Y-Z plane format (MSE coordinates as viewed from the sun) while the present study uses a variety of formats. All of these small but important distinctions between the methodologies lead

to the present study producing more definitive answers regarding the characteristics of energetic planetary ions beyond the IMB at Mars.

Regarding velocities shown in Fig. 5.8, they do not consistently match what would be expected from high energy pickup ions accelerated by the convection electric field, but this does not necessarily mean there is a need to search for alternative acceleration mechanisms. The fluxes seen in Fig. 5.8 are directed more downtail (less radially outward) than is typically associated with the energetic plume, but this is due at least in part to the cylindrical coordinate system used, in which the radial component incorporates the Y_{MSE} velocity as well as the Z_{MSE} velocity. Still, the velocity vectors shown are more erratic than those appearing in work using the same method but looking at lower energies (see *Fraenz et al.*, 2015). There are at least three possible explanations for this. First, it is possible that some of the heavy ions in the 2-15 keV energy range were accelerated by a process other than motional electric field, causing them not to follow the bulk plume flow direction. Second, there was concern that, even though a concerted effort has been made to avoid ghost H^+ counts, the number of ions at such high energies is so low that even a very small amount of H^+ contamination could impact results in some spatial bins. Spot-checking revealed proton contamination to be rare but not non-existent in the mass and energy ranges used in this study. The global picture should be largely unaffected. Finally, velocity vectors are also affected by the large uncertainty in the angle of rotation to achieve MSE coordinates for each IMA sweep, which leads to incorrect binning. It is likely that many of the values creating the vectors in one quadrant would actually be in another quadrant if the IMF proxy were perfect. This will lead to, for example, measurements from Y_{MSE} quadrants sneaking

into the Z_{MSE} quadrant and making the mean flow direction less radial than what is expected for the energetic plume.

The reverse-asymmetry seen on the nightside, in which 2-15 keV heavy ions are seen more in the $-E_{SW}$ direction than in the $+E_{SW}$ direction (Fig. 5.5, Fig. 5.9, Fig. 5.7 a) might be explained by arguing that many of the ions measured are in fact plume particles moving more radially outward than the averaged flux vectors indicate, leaving a relative void of energetic heavy ions immediately anti-sunward of the main plume of radially-directed ions. Keeping in mind that Figure 5.3 shows that there is little data from the $-E_{SW}$ nightside, however, a more mundane possibility is that the apparent reversal in E_{SW} asymmetry in portions of the nightside is a product of low counting statistics (recall the overlapping error bars in Fig. 5.7 (a)). It is important to note that *Y. Dong et al.* [2015], which was able to directly measure the direction E_{SW} with MAVEN's magnetometer when MAVEN was upstream of the bow shock, found no such reverse asymmetry on the nightside. Instead, across all values of X_{MSE} examined, *Dong et al.* [2015] saw greater fluxes of O^+ in the $+E_{SW}$ hemisphere. This suggests that the reverse asymmetry seen here is due to a combination of low counting statistics and uncertainty in the direction of E_{SW}.

The primary uncertainty in this study – and therefore a key problem to be addressed and discussed further – is the precise direction of the upstream IMF. The exclusion of times when the draping direction of the IMF was unsteady has played a role in revealing a clearer global asymmetry than was seen in chapter 4, but the results presented here still rely on the assumption that the magnetic field at 400km altitude has the same clock angle as the upstream IMF. It is known that this simplified model of field line draping is an idealization of the actual picture.

Brain et al. [2006] found hints of "weathervaning" (a bending of field lines associated with unequal mass-loading along a magnetic flux tube) of the draped field in MGS magnetometer data as well as indications that the toward and away sectors of the solar wind do not result in draping configurations that perfectly mirror each other. *Luhmann et al*. [2015] presented comparisons of the MGS draping angle with MHD results, finding some agreement but also noticeable differences due to weathervaning and crustal field influences. *Xu et al.* [2017] used pitch angle measurements from MAVEN's Solar Wind Electron Analyzer to examine magnetic connectivity, and found that in the 400-600km range, at the latitude range used for the draping proxy adopted in the present study, MAVEN saw either closed or open field lines more often than draped field lines (*Xu et al*., Figs. 8,9,10). This suggests that the strong clustering of estimates of E_{SW} shown in Fig. 5.2 may be at least partially due to MGS at 400km, 50-60° latitude, having frequently measured field lines connected to the electron exobase, which may not correspond to draped IMF. The large uncertainty in upstream IMF angle, together with the fact that the clustering of values in Fig. 5.2 suggests that errors in the draping proxy are in part systematic, have inspired the planning of a project in which we will attempt to create a more reliable draping proxy that could be used to study the entire time period during which MGS was at its 400km mapping orbit. For the task of identifying hemispheric or quarter-cylinder resolution asymmetries, our analysis has convinced us that the Brain proxy is sufficient, allowing us to establish that the MEX ion data, used carefully and in conjunction with MGS, can be used to observe the planetary ion energetic plume statistically.

Limitations of the IMA instrument have also affected the results reported here. First, the IMA duty cycle is such that it is often inactive when MEX is at very high altitudes, where these E_{SW}-accelerated ions are most likely to be seen. Second, IMA was mounted on the spacecraft, in part,

"to co-aligned the central plane of the IMA field of view with the ecliptic plane when the spacecraft is in the Earth pointing mode" (*Barabash et al.*, 2006). An unfortunate effect of this alignment is that when the IMF is in the ecliptic plane, as it often is in the nominal Parker Spiral configuration, E_{SW} is aligned outside of IMA's field of view. Measurements in *Dong et al.* [2017] depict energetic plume flow directions that such a field of view would be expected to miss, and a specific example of this can be seen in the case study of the plume shown in chapter 4 in which very strong ion beam is seen at the furthest extent of IMA's elevation angle, suggesting part of this population may have been missed by IMA. The distribution of E_{SW} shown in Fig. 5.2, shows that much or even most of the time the IMF was estimated to not be in the ecliptic plane. However, since the field of view issue is expected to be worst for what is in general the most common IMF orientation, surveys of the energetic plume using MEX cannot hope to obtain realistic estimates of plume fluxes or escape rates.

An additional uncertainty may stem from any seasonal variations of the energetic plume or of IMF draping around Mars. The period of time covered by this study is only slightly longer than one Mars year, too short of an interval to identify seasonal patterns or to guarantee that effects of seasonal variations are completely washed out in the statistics. Using MAVEN's STATIC instrument, it was found by *Dong et al.* [2017], that plume escape fluxes did not appear to vary significantly with EUV flux. However, of the two time periods considered by *Dong et al.*, the period closer to the maximum of solar cycle 24 (and hence the time period from which their larger EUV values were drawn) was 11 November 2014 to 19 March 2015, which also happens to be a period that straddled Mars' northern winter solstice. It has been found that during southern summer conditions such as this, the strong crustal field region raises the altitude of the IMB across the entire dayside (*Brain et al.*, 2005). Thus, the unexpected result in *Dong et al.*

[2017], that increased EUV did not correlate with increased plume fluxes, may be due to the period of higher EUV coinciding with a period of high IMB. A higher IMB would mean that fewer ions were born outside of this raised IMB, and ions born inside the IMB would be less likely to make it out into the magnetosheath where E_{SW} is strong, effects which would tend to counteract the increased scale heights and increased production rates of a high EUV time period. Such possible seasonal effects should also exist in the present study. The time period we used included two northern summers but only one northern winter.

Given the broader communal goal of developing estimates of atmospheric loss on geological time scales, the question of how plume escape changes with key time-varying parameters is deeply important. MAVEN observations have shown the plume as well as the role of the solar wind convection electric field in creating the plume (*Brain et al*., 2015, *Dong et al*., 2017). However, exploring the time-variation of plume escape with limited amounts of data is very difficult. The difficulties associated with limited data have been highlighted in the previous paragraph's discussion of *Dong et al.* [2017], where it was noted that the period of high EUV flux also happened to correspond to a season that may counteract the influence of increased EUV. With MAVEN likely to begin prioritizing its role as a relay between Earth and assets on the Martian surface only a fraction of a solar cycle after its Mars orbital insertion, the importance of expanding the periods of time open to study is being made even more clear. As the only statistical study using IMA data to identify characteristics of this plume population by focusing specifically on the relevant locations and particle energies, we believe that this study is a first step toward opening a time period unseen by MAVEN to exploration of the plume and its variability.

We have shown that, despite the fact that the MEX mission was not designed to prioritize study of the energetic plume population, MEX IMA can and does see a statistical plume. The next step is to examine how the plume, as seen by IMA, varies with parameters such as EUV flux, crustal field positioning, and solar wind parameters. This examination of drivers, however, is complicated by our finding that these same drivers of plume escape rates can be shown to influence the IMF clock angle proxy used in the present study. This could lead to a result in which we are uncertain of whether a driver's correlation with a perceived stronger plume is truly due to increased plume loss or whether the actual correlation is between the driver and better estimates of the $+E_{SW}$ direction. Untangling these effects is beyond the scope of the present chapter. These exercises may be more fruitful after completion of a project to improve the IMF draping proxy.

Chapter 6: A Project to Improve the IMF Draping Proxy

The orientation of the Martian magnetosphere is determined not by a planetary dipole, but by the direction of the interplanetary field (IMF) in which Mars is embedded. Estimates of the upstream IMF direction from the time period when Mars Global Surveyor (MGS) was in a 2pm - 2am 400km altitude orbit (April 1999 – October 2006) are complicated by at least two major phenomena that affect low altitude magnetic field measurements: weathervaning (bending) of draped IMF and the presence of crustal fields that might at times entirely prevent the measurement of IMF. In this chapter, seasonal effects of weathervaning are examined, and a multifluid magnetohydrodynamic model is used to estimate (and then undo) the seasonally-dependent effects of weathervaning in the MGS observations. The result is an IMF clock angle estimate, usable for the entire 7.5 year time span for which the only magnetometer data is at 400km altitude, that is demonstrably more accurate than previous proxies.

6.1 The Interplanetary Magnetic Field Clock Angle

The orientation of Mars' induced magnetosphere is determined by the crossflow component of the interplanetary magnetic field (IMF). When the IMF rotates about the Mars-Sun axis, the induced magnetosphere rotates with it, reorienting itself on time scales of seconds and minutes (*Modolo et al.,* 2012). The list of phenomena reported to be organized by the IMF crossflow

direction is extensive, with a partial list including the orientation of the magnetotail lobes and current sheet (e.g. *Nagy et al.*, 2004), the distribution of ion beams in the magnetotail (*Carlsson et al.*, 2008), bow shock location (e.g. *Vignes et al*., 2002; *Edberg et al.*, 2009), asymmetries in magnetic field strength in the magnetic pileup region (e.g. *Dubinin* et al., 2006), energy input into the ionosphere associated with sputtering (e.g. *Hara et al.*, 2017), the occurrence of ion cyclotron waves (e.g., *Wei et al*., 2011), and atmospheric escape fluxes of heavy ions (e.g. *Dong et al.*, 2015).

Discussions of these asymmetries make use of some standard terms. The Mars-Solar-Orbit (MSO) coordinate system, centered on Mars, is defined with its x-axis pointing toward the sun, the y-axis pointing in the direction opposite to Mars' orbital motion, and the z-axis completing the right-handed coordinate system. The clock angle of the IMF (θ_{IMF}) is defined as the angle of the upstream IMF in the MSO y-z plane, measured counterclockwise from 0° at the Y_{MSO} axis. In this same plane, the convective electric field, $E_{SW} = -V_{SW} \times B_{IMF}$, points in a direction 90° counterclockwise of θ_{IMF}, and the +(-) E_{SW} hemisphere refers to the hemisphere in which E_{SW} is directed away from (toward) the planet.

Direct observations of θ_{IMF}, particularly prior to the arrival of the Mars Atmosphere and Volatile EvolutioN (MAVEN) spacecraft, were alternately scarce or nonexistent, resulting in a variety of methods of estimating θ_{IMF}. *Vennerstrom et al*. [2003] estimates θ_{IMF} by propagating IMF measurements by the ACE satellite at Earth's L1 point out to Mars' orbit, a technique that is only reliable when Mars is magnetically aligned with ACE. *Crider et al*. [2004] estimates θ_{IMF} over the course of an entire Mars Global Surveyor (MGS) orbit by observing the shocked IMF in the Mars magnetosheath and assuming the IMF direction held steady for the duration of the orbit

(unshocked IMF, tending to have a magnitude nearer to the magnitude of the spacecraft's own fields, was thought to result in a larger error). Using the Mars Express (MEX) satellite's Ion Mass Analyzer (IMA), *Yamauchi et al*. [2007] and *Yamauchi et al*. [2008] describe and validate a method of estimating θ_{IMF} by identifying the orientation of the ring distribution in velocity space of pickup H^+ observed by IMA. This clever approach is a powerful tool for case studies, but it can only be used for times when MEX happens to be upstream of the bow shock at the same time that the protons' velocity space ring distribution is seen clearly by IMA, a restriction that limits its usefulness for large statistical surveys.

Method of estimating E_{SW}	Technique Used	Limitations
Vennerstrom et al. [2003]	Propagates ACE measurements upstream of Earth to Mars' orbital distance	• Works well only when Earth and Mars are aligned
Crider et al. [2004]	MGS magnetosheath observations assumed to be representative of unshocked solar wind	• Sheath observations not present during era of MEX ion data • Assumes IMF steady throughout an entire orbit
Yamauchi et al. [2007,2008]	Identifies velocity space ring distribution of pickup H^+ using MEX	• Ring distribution clearly present only for cases, unrealistic for a statistical study
Fedorov et al. [2006]	MGS 400km alt. observations, IMF clock angle given as $\arctan(\frac{B_{IMF_z}}{B_{IMF_y}})$ in MSO coordinates Values interpolated linearly between the sparse observations meeting these requirements: MGS was at low SZA and in a region of low crustal field strength.	• 400km alt. measurements not necessarily representative of sheath, much less upstream sw • Low SZA requirement decreases amount of useable data (orbits when strong crustal fields were near subsolar point are omitted)
Brain et al. [2006]	MGS 400km alt. observations, IMF clock angle given determined using local angle-from-east. A single value given per MGS orbit, which is an average for the 50°-60° latitude range with weak crustal fields	• 400km alt. measurements not necessarily representative of sheath, much less upstream sw • Assumes IMF steady throughout an entire orbit

Table 6.1. Summary of techniques used to estimate the clock angle of E_{SW} at Mars. The technique described in *Brain et al.* [2006] includes the largest amount of time intervals for which MEX ion observations are available.

Of particular relevance to the present study are two methods of estimating θ_{IMF} that use MGS magnetometer data during the mapping phase the MGS mission, from April 1, 1999 through October 2006, when MGS was in a 2am-2pm circular orbit at 400km altitude. *Fedorov et al.* [2006] defines a proxy as $\boldsymbol{\theta_{IMF} = \arctan(Bz_{MSO}/By_{MSO})}$ for time intervals when the solar zenith angle is less than 60° and Cain's model (*Cain et al.*, 2003) of the crustal fields has a magnitude of less than 3nT. If there was less than 2.5 hours between consecutive brief periods for which both of these criteria were met, a linear interpolation was used so that times in this larger interval were also assigned a clock angle. Finally, a method of clock angle determination described in *Brain et al.* [2006] incorporates a larger number of time intervals by removing the low solar zenith angle requirement and attempting to maintain accuracy at high solar zenith angles by considering the draping of the magnetic field lines around the planet, and estimating θ_{IMF} everywhere by setting it equal to the azimuthal angle in the horizontal plane measured from 0° defined as local east. This *Brain et al.* proxy uses the median azimuthal angle measured between 50° and 60° N latitude, where the crustal magnetic fields are relatively weak at all longitudes, resulting in a single value of θ_{IMF} for each orbit of the MGS. A summary of the various methods that have been used to estimate the clock angle of θ_{IMF} – and hence the clock angle of E_{SW} – is provided in Table 6.1.

6.2 Limitations of Low-Altitude Proxies for Upstream IMF

The proxies for θ_{IMF} described in both *Fedorov et al.* [2006] and *Brain et al.* [2006] assume that the field measured at 2pm local time, 400km altitude corresponds to draped IMF lying in the

same plane as the upstream IMF. In reality, these field lines begin to bend as soon as they are in contact with heavy planetary ions, resulting in draped fields tilted toward the subsolar point. This effect was first seen at Venus in magnetometer data of Pioneer Venus Orbiter (*Luhmann et al.*, 1987), and reproduced with a three-dimensional convection/diffusion model of by *Luhmann* [1988], where it is described as a "focusing of the field toward the subsolar point." The curvature of the draped field lines is such that it appears as though, for each draped field line not located at the magnetic equator, the center of the field line has been dragged toward the subsolar point. *Law and Cloutier* [1995] dubs this effect "weathervaning," and describes it both as the effect of mass-loading of field lines and as an alignment of the field with the day-to-night ionospheric flow. Figure 10 in *Law and Cloutier* provides an illustration of the weathervaning seen by Pioneer Venus Orbiter.

In the case of Mars, low altitude magnetometer observations can be influenced by crustal fields in addition to weathervaning, even over regions where the crustal field strength is small. *Ulusen et al.* [2016] analyzed the results of a multi-species magnetohydrodnamic (MHD) model of the Mars-solar wind interaction for solar maximum conditions and found that, at 400km altitude on the dayside, large regions were on closed magnetic field lines. This presence of closed field lines was even seen within the 50°-60° N latitude band of relatively weak crustal field used in the Brain proxy. These MHD results are supported by a study performed by *Xu et al.* [2017] in which magnetic topology was inferred by distinguishing photoelectron populations from magnetosheath electrons at specific pitch angles using the MAVEN spacecraft's Solar Wind Electron Analyzer measurements. That study found that when MAVEN was in the 400-600 altitude range and in the 50°-60° N latitude band, electron signatures were consistent with closed

field lines more than 30% of the time. *Luhmann et al*. [2015] addresses the issue of MGS mapping orbit observations more directly, using multi-species MHD to show that for eastward IMF and for westward IMF, and for the strongest crustal fields oriented at noon or at midnight, the azimuthal angle of magnetic field at the θ_{IMF} proxy location was about 240°. This study concluded that "observations are consistent with the crustal field influence interpretation."

A third complication that arises in the interpretation of magnetic field observations at 2pm, 400km altitude, 50°-60°N is the effect of seasons. This location changes its position in an MSO coordinate system over the course of a Martian year, as Mars' 25° axial tilt rocks the proxy location toward the subsolar point (less weathervaning) or away from it (more weathervaning), and even puts the proxy location in the $-Y_{MSO}$ sector during a portion of the year, where the effects of weathervaning rotate the clock angle of a draped field line in the opposite direction as that of weathervaning rotation in the $+Y_{MSO}$ sector. This effect is visible in Fig. 6.1, in which a black curve marks the path of the MGS observation location over the course of a Mars year in MSO coordinates. It is clear from the figure that different extents of weathervaning may be expected at this MGS observation location at different points of the year, as MGS sees different portions of the global weathervaning pattern. Additionally, as Mars' highly elliptical orbit brings the planet closer to (perihelion ≈ 1.38 AU) or further from (aphelion ≈ 1.67 AU) the Sun, the change in EUV flux as a function of heliocentric distance can be as high as 45%, which may result in differences in ionospheric density large enough to cause seasonal changes in the extent of weathervaning.

Even though θ_{IMF} proxies exist and have been used in numerous studies, it is clear that improvements can be made by the isolation and removal of factors influencing the connection between a magnetic field measurement in the magnetic pileup region and the upstream IMF. In this study we examine the behavior of the observed field at the proxy location over the full seven and a half year extent of the mapping orbit of MGS, apply the knowledge gained from this examination to the creation of an improved proxy for the upstream IMF clock angle θ_{IMF}, and validate this new proxy by showing how successfully it organizes heavy ion data known to be highly dependent upon IMF direction. We have adopted the blueprint of the *Brain et al.* proxy, using observations from 50°-60°N to generate a single-value estimate of θ_{IMF} for every two-hour orbit throughout the entire seven and a half years of the MGS mapping phase. Throughout the remainder of this paper we will refer to the *Brain et al.* proxy as the "original proxy," as it will be used as a baseline against which our new θ_{IMF} may be measured.

6.3 Mapping Upstream IMF to a Weathervaned Azimuthal Angle

The MSO coordinate location of 55°N, 2pm, 400km altitude over the course of a Martian year is shown as a black curve in Fig. 21. The rest of the information contained in Fig. 21 comes from simulation results of the Block-Adaptive-Tree Solar-wind Roe-type Upwind Scheme (BATS-R-US) multifluid magnetohydrodynamic (MFMHD) model. This model was described very briefly in chapter 3 of this dissertation, and is described in more detail in *Liemohn et al.* [2017]. The colored curves in Fig. 6.1 are magnetic field lines that intersect the 2pm 400km altitude orbital location of MGS, extracted every 15˚ along the orbit track, for the specific case of the Mars axial tilt being aligned with the Z_{MSO} axis. These field lines are colored by altitude, showing that the field lines that map to the lowest altitude, which in the model occur in the $-E_{SW}$ hemisphere, are also the field lines that

exhibit the most extreme weathervaning. It is clear from the different extents of weathervaning beneath the seasonal path of the proxy location that in order to correct for weathervaning in MGS observations, season must also be taken into account.

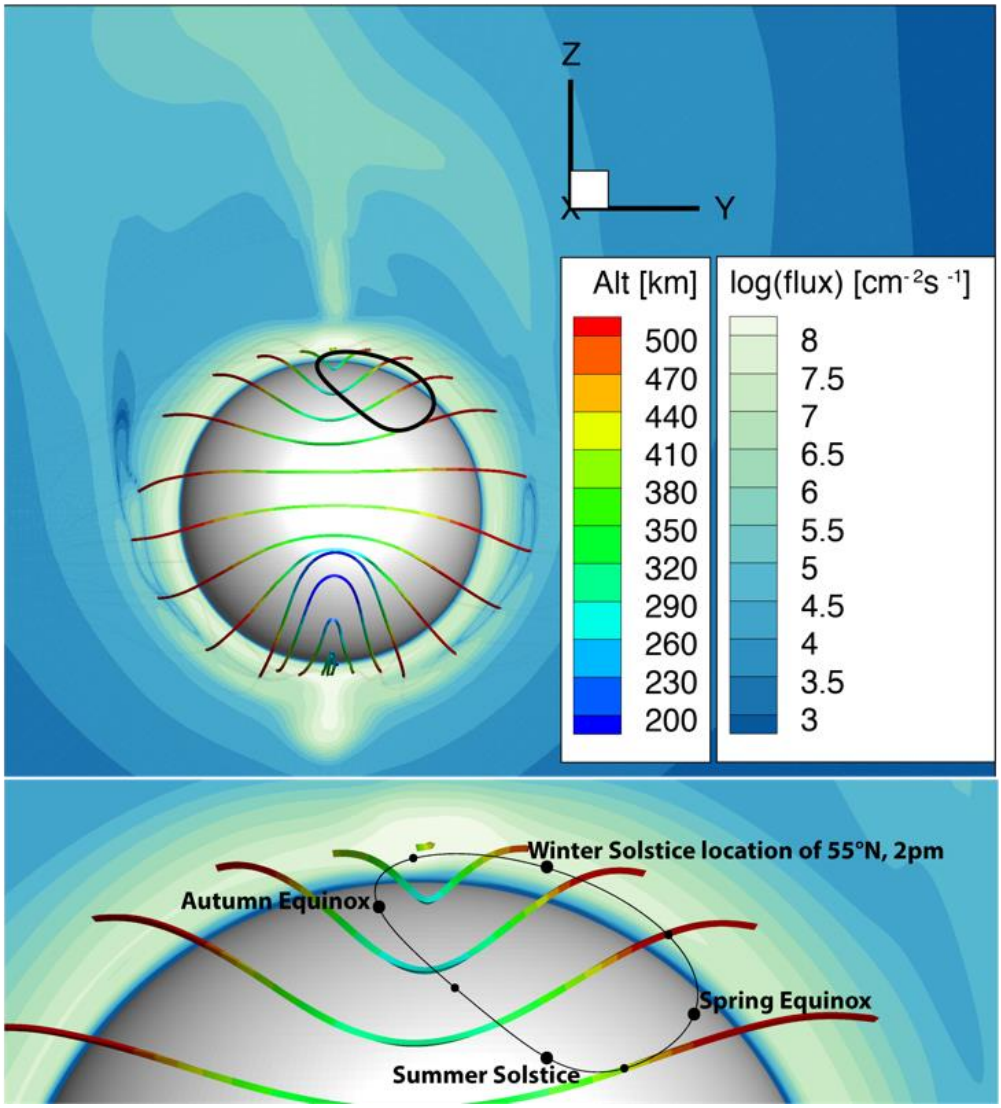

Figure 6.1. A view from the sun in what is effectively MSE coordinates (the upstream IMF points eastward on the dayside of Mars). The sphere is located at the 100km inner boundary of the MFMHD model. Overlaid on the MFMHD results is a black curve showing the seasonal track of the 2pm 400km altitude 55°N proxy location. The colored lines are magnetic field lines connected to the 2pm 400km orbital path of MGS and colored according to altitude at each point along the field line. The color contours on the terminator plane show the x component of O^+ particle flux. Beneath the global view is a zoomed-in image showing the proxy location for specific northern hemisphere seasons during a Mars year.

Just how well can seasonal weathervaning effects reproduce MGS observations at the proxy location? Figure 6.2a shows the observation frequency of azimuthal angles of the original proxy. It shows that MGS very often observed a magnetic field at the proxy location whose horizontal component pointed about 240° counterclockwise from local east. It is instructive to compare this with the azimuthal angle (again, measured counterclockwise from local east) of a line pointing toward the subsolar point from the average location of the proxy measurement, which is 250.7°. This demonstrates that the observed clustering of observations around 240° is consistent with the direction of weathervaned westward IMF, which would be bent in the direction of, but not directly toward, the subsolar point, much like the field lines depicted in Fig. 6.1. The bottom panel of Fig. 6.2 (Fig 6.2b) shows the occurrence frequency of azimuth angles defined in the same way but taken from the MFMHD at the seasonally-corrected location of the θ_{IMF} proxy. To generate Fig 6.2b, 360 upstream IMF clock angles were simulated by rotating to the proxy location around the X_{MSO} axis. Each IMF angle was then weighted according its rate of occurrence in ACE magnetometer data from the time period corresponding to the MGS mapping orbits. The similarities between the top and bottom panel suggest that some of the features in the observed data, such as a clustering in the 240° direction and a corresponding scarcity of observed azimuths in the 100°-200° range, may be explained by weathervaning and season alone. Key differences between the observed azimuths and MFMHD azimuths include the greater depth of the valleys in the bottom panel and the absence of a sharp peak at 40° in the top panel. The absence of a sharp peak at 40° in the top panel is likely due in part to *Brain et al.* [2006] having been correct in its supposition that weathervaning in the $+Z_{MSO}$ hemisphere occurs less

frequently for eastward IMF than for westward IMF. Noting that eastward IMF unweathervaned would center broadly around an azimuth angle of 0°, we would expect that the shallower depth of the 90°-200° valley in the observed draping azimuths is not caused only by the spreading out of the 40° peak. The difference in rareness of this azimuth range may instead be an indication that the MFMHD exhibited stronger weathervaning than MGS observed, bending a greater percentage of possible combinations of θ_{IMF} and MSO proxy location toward the subsolar point.

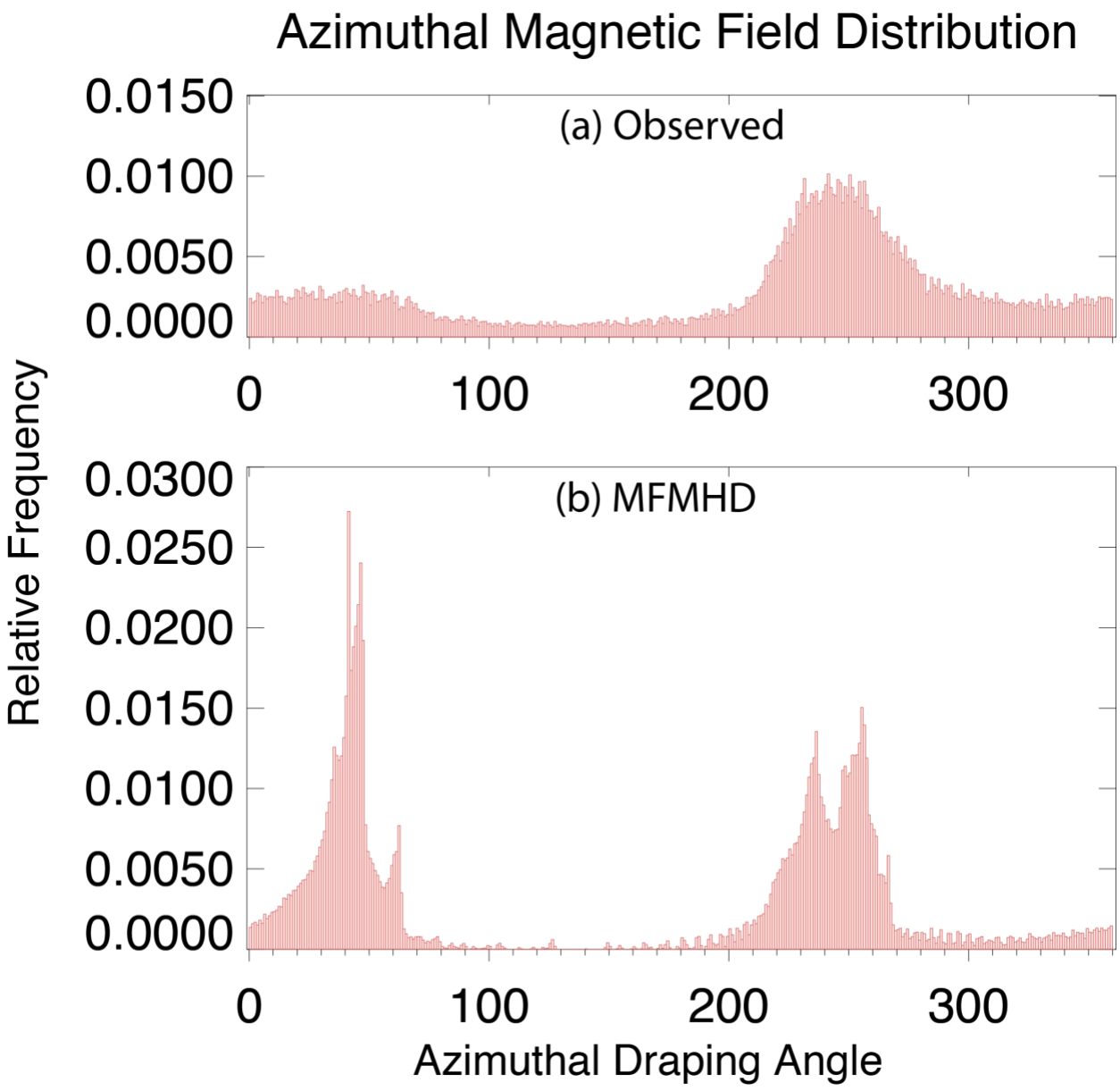

Figure 6.2. The top panel (a) shows the relative frequency distribution of observed azimuth angles, as measured counterclockwise from local east. The bottom panel (b) shows the weighted distribution of MFMHD weathervaned angles as extracted from the same locations as the observations, again as measured counterclockwise from local east.

We can take a closer look at the simulated weathervaned distribution of Fig. 6.2b by keeping track of which upstream θ_{IMF} directions are mapping to specific draped azimuthal directions. Figure 6.3 is like Fig. 6.2b in that it shows a relative frequency of MFMHD-simulated draping azimuths measured from local east. Whereas Fig. 6.2b shows the percentage of all IMF clock angles that map to each bin of the histogram, the vertical axis in Fig. 6.3 shows the percentage of IMF clock angles within a specific quadrant that map to each bin. Each θ_{IMF} quadrant is given a different color or shading. It is clear that in the MFMHD, due to our methodology, the clustering caused by weathervaning occurs for all ranges of θ_{IMF}. Fig. 6.3 shows that the dearth of simulated azimuth angles between 90° and 200° is associated with heavy weathervaning of westward IMF, and that an increase in observed azimuth angles in this range would be expected to accompany any decrease in the extent to which westward IMF weathervanes, consistent with the idea that the MFMHD simulated weathervaning is more extreme than what MGS observed. An unexpected feature of Fig. 6.3 is that a portion of westward IMF was caught mapping to the 40°-80° range, while a portion of eastward IMF maps to around 270°, both nearly in the opposite direction from what we expect from a measurement in the afternoon. Further breakdown of the mapping revealed the cause of these surprising features. They occurred during that time of year when Mars' tilt axis had moved the 2pm ~55°N measurement location into the $-Y_{MSO}$ sector. During these times, weathervaned westward IMF would be expected to be pointing nearly away from the subsolar point rather than nearly toward it (~110° rather than ~240°). The $-Y_{MSO}$ location of these measurements mostly explains the unexpected azimuths, but there is another

factor at work. The westward IMF azimuths seen during these times in the MFMHD are centered on the 'wrong' side of 90°, i.e., at 70° rather than 110°. This greater-than-90°-rotation of westward IMF cannot be explained by classic draping or by weathervaning, and is due primarily to the fact that Fig. 6.3 uses local east as the definition of a 0° azimuth angle, and this time of Mars' year when the proxy location was in the $-Y_{MSO}$ sector is necessarily also a time during which there is a large angle between local east and the $+Y_{MSO}$ direction, and is something to bear in mind while viewing the results.

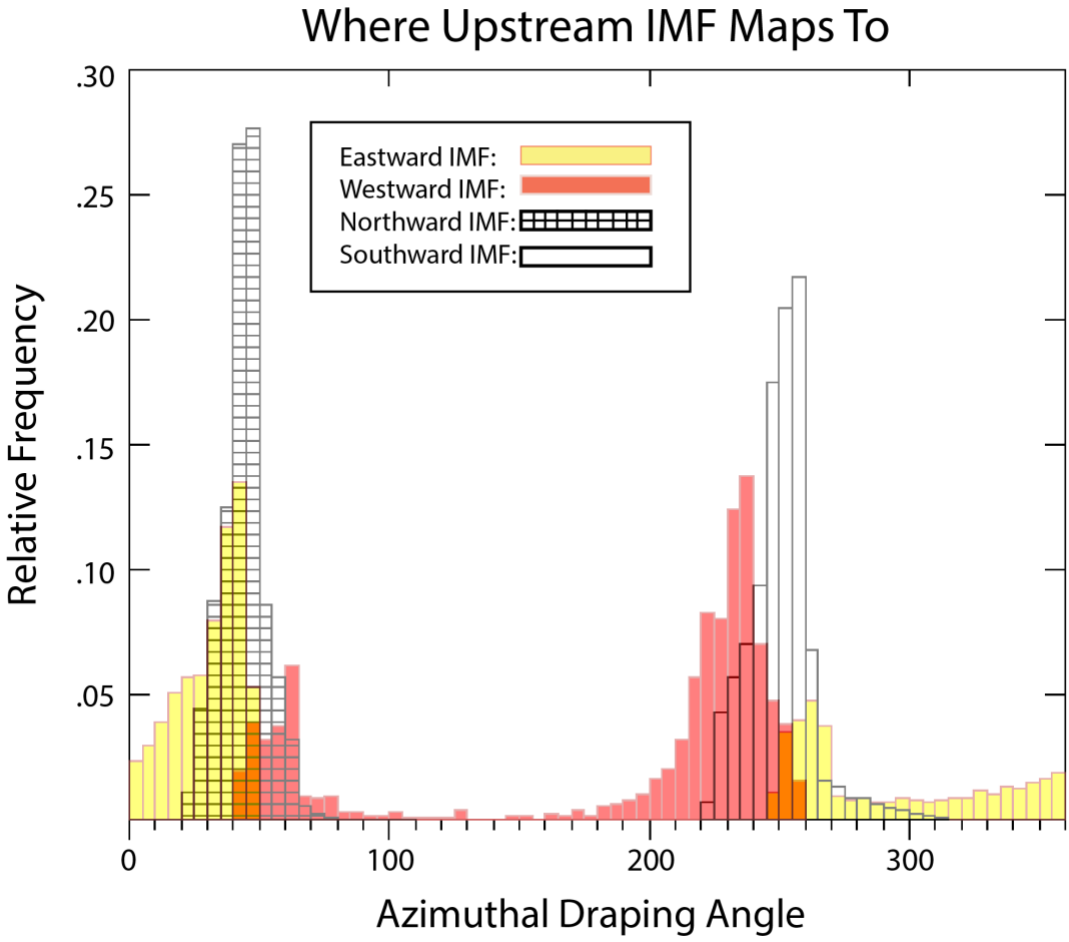

Figure 6.3. Separate histograms showing where upstream eastward (315°-45°), northward (45°-135°), westward (135°-225°), and southward (225°-315°) IMF clock angles map to at the proxy location after applying the heavy weathervaning seen in the MFMHD.

6.4 EUV Dependency

Two types of seasonal periodicities appear to be present in the MGS observed draping azimuths. Figure 6.4 is much like Fig. 2a in *Brain et al.* [2006], a scatterplot showing draping azimuth measured from local east on the vertical axis and time on the horizontal axis. The substantive differences are that, unlike the plot in *Brain et al*., Fig. 6.4 covers the entire time period during of the MGS mapping orbit, and it also includes vertical lines marking Mars' perihelion (red) and the northern winter solstice (black). The first type of periodicity is the exact direction of weathervaning of westward and southward IMF. The clustering of values near 240° occurs at a lower azimuth angle when local east is rotated counterclockwise (northern fall) and when the proxy location is closer to the subsolar point, decreasing weathervaning (northern summer). Conversely, this same clustering occurs at higher values when local east is rotated clockwise (northern spring) and when weathervaning is increased by the proxy location being situated further from the subsolar point (northern winter). The result is that the direction in which values cluster most strongly reaches its peak (~270°) at some point between Mars' northern winter and spring. The second type of seasonal periodicity is less obvious and, rather than being a seasonal shift in the exact direction of a weathervaned magnetic field vector, is a seasonal shift in whether weathervaning for eastward IMF occurs at all. Thus, rather than an oscillation around a weathervaned direction of 50°-60°, we see a larger amplitude oscillation between weathervaned values of ~60° all the way down to unweathervaned measurements of eastward IMF (330°-30°). Whereas the periodicity in the exact direction of weathervaning for westward IMF is interpreted as resulting from the movement in MSO coordinates of the proxy location over the course of a Mars year, the periodicity in whether eastward IMF weathervanes at all or does not is an effect

we attribute to the eccentricity of Mars' orbit. This periodicity peaks at azimuths ~60° around perihelion, when ionospheric production is highest due to increased EUV flux, so that the heavy-ion-driven effect of weathervaning is present in the northern hemisphere even for the eastward IMF.

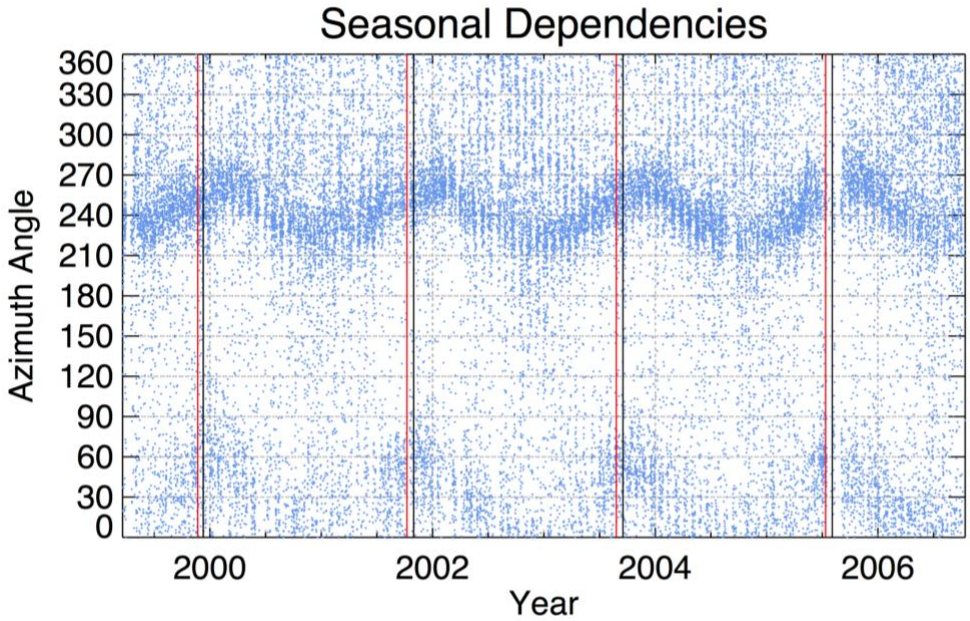

Figure 6.4. A scatterplot with time on the horizontal axis and observed azimuth angle from east on the vertical axis. Seasonal periodicities are present, and vertical lines in red (perihelion) and black (northern winter solstice) are marked to aid in understanding the drivers of the seasonal periodicities.

Evidence for the above interpretation – that eastward IMF is likely to result in weathervaning at the proxy location only during times of high EUV flux – is provided in Fig. 6.5, which shows how frequently different azimuth angles were observed as a function of ionizing flux. The horizontal axis of Fig. 6.5 represents the F10.7 flux measured at Earth, scaled to Mars' orbital distance as $\mathbf{1}/\boldsymbol{r}^{\mathbf{2}}$ and time-shifted from Earth to account for the time elapsed from when a point on the sun faced Earth to when that same point was directed toward Mars. This technique for a Mars F10.7 proxy was developed and first used by *Mitchell et al.* [2001]. The vertical axis shows

what fraction of the total number of observations made within a narrow range of F10.7 fell within specified clock angle ranges. The flat horizontal lines to the right of F10.7=110 are the result nonstandard binning of the data. Due to the low number of observed azimuth angles for which the F10.7 proxy was greater than 110, all observations for which the F10.7 proxy was higher than 110 were lumped into a single bin, allowing this bin, like the others, to have enough observations (several dozen) to yield reliable occurrence frequencies. The quantities displayed in the legend are the Pearson Correlation Coefficients calculated using all F10.7 bins except for the last, wider, bin. The red line shows that as EUV flux increases, a larger fraction of azimuths are observed in the 0°-90° range of azimuth angles, which is where weathervaned eastward IMF would be observed. This increase in 0°-90° azimuths with increasing EUV is associated with a simultaneous decrease in the fraction of azimuths observed in the 290°-360° range, where eastward quadrant IMF would often map to if weathervaning did not occur. Taken together, not only are Figs. 6.4 and 6.5 consistent with previous suggestions that weathervaning in the northern hemisphere of Mars may occur more for some clock angles than for others (see Fig. 9 in *Brain et al.*, 2006), they provide the evidence that for sufficiently high EUV fluxes, this asymmetry begins to disappear, as the ionosphere is dense enough that even less-frequently weathervaned orientations become weathervaned.

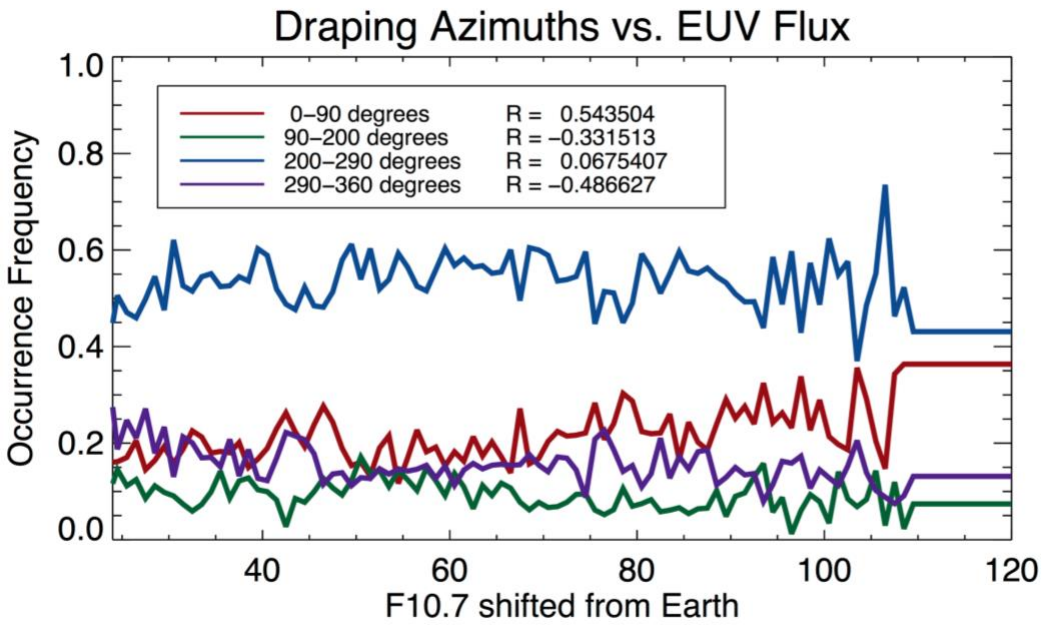

Figure 6.5. A breakdown of how often different ranges of azimuth angles from east were observed as a function of solar ionizing flux. The red (blue) line represents the direction expected for weathervaned eastward (westward) IMF, while the purple (green) lines largely represent the direction expected for unweathervaned eastward (westward) IMF.

6.5 Solar Wind Pressure Dependency

Figure 6.6 is much like Fig. 6.5, but rather than showing the observed draping azimuths as a function of EUV as in Fig. 6.5, in Fig. 6.6 we show the azimuth ranges mapped as a function of subsolar magnetic pressure. *Crider et al.* [2003] published a technique estimating upstream solar wind dynamic pressure using the magnitude of the magnetic field in the magnetic pileup region. The estimate of the subsolar magnetic field strength used in Fig. 6.6 is a similar method, that first used in *Brain et al.* [2005], in which a subsolar field magnitude is estimated for each MGS mapping phase orbit by taking all magnetic field data taken at solar zenith angles less than 110°, omitting locations with a strong crustal magnetic field presence, and extrapolating to the subsolar point by fitting to a cos(SZA) function. An increase in the frequency of strong weathervaning of

westward IMF would look like a decrease in the unweathervaned (green) line accompanying an increase in the blue line. Similarly, an increase in the frequency of strong weathervaning of eastward IMF would look like a decrease in the purple line accompanied by an increase in the red line. While it's possible that these effects are present (more on this in the discussion section), the largest trend seen in Fig. 6.6 is something else entirely. The azimuth ranges with the strongest correlation coefficients are the range that includes the direction of weathervaned westward IMF (blue line) and the range including the direction of weathervaned eastward IMF (red line). We think this is the result of a crustal field influence that becomes less severe with increasing subsolar pressure. The case was made in the introduction (section 6.3) that the clustering of observed azimuths around 240° may be the result of crustal field influence. Given that the frequency of observing eastward vs. westward IMF at Earth was equal over this 7.5-year time span, the fact that, for low subsolar pressures, more than half of observed azimuths fell into the 200-290° range is a warning flag of its own, an effect likely caused by crustal field influence resulting in a disproportionately high number of observations near 240°. What is clear in Fig. 6.6, however, is that as the dayside pressure increases, the red line and the blue line get much closer together. In other words, the fraction of observations falling into the weathervaned westward direction and the fraction of observations of weathervaned eastward azimuths become much more similar. This could be explained by crustal fields being pushed beneath the 400km observation altitude during times of high subsolar pressure, allowing us to see the "true" occurrence frequencies of different draping directions without crustal fields adding false weight to the 240° azimuthal direction.

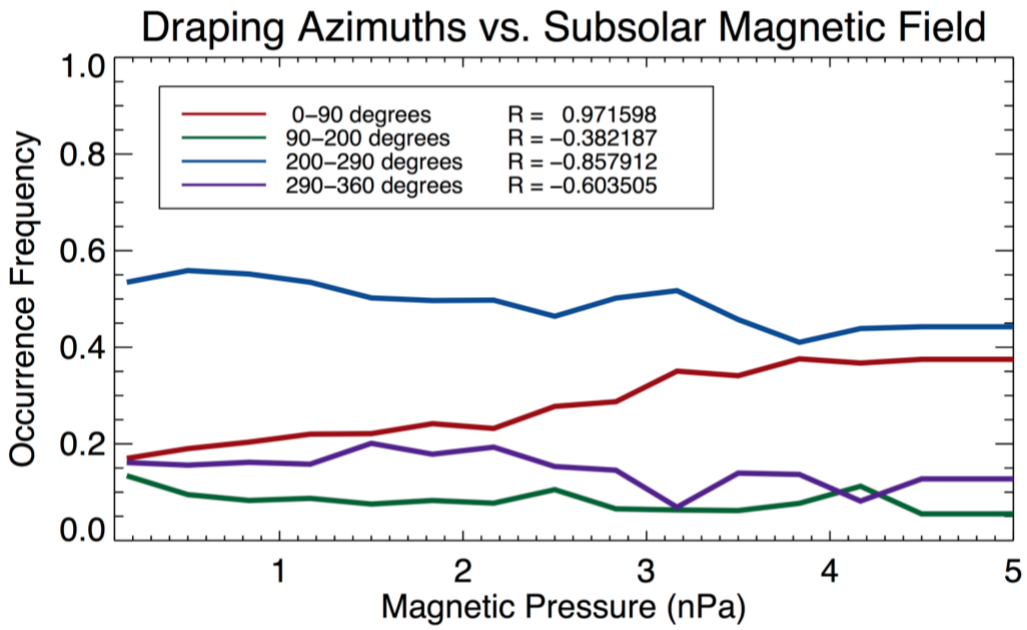

Figure 6.6. A breakdown of how often different ranges of azimuth angles from east were observed as a function of subsolar magnetic field strength. The red (blue) line represents the direction expected for weathervaned eastward (westward) IMF, while the purple (green) lines largely represent the direction expected for unweathervaned eastward (westward) IMF.

6.6 Creating New Proxies for θ_{IMF}

The alternative proxies explored in this study are each based on what we call the "original proxy," which is described in *Brain et al.* [2006]. A single azimuthal angle based on the weak-crustal-field 50°-60°N latitude band is given to represent the upstream IMF clock angle for each 2-hour long orbit of MGS during its mapping phase orbits (April 1999 – October 2006). The various proxies differ slightly in how this single clock angle measurement at 400km is mapped to an upstream IMF angle. The five new proxies tested vary from the original and from each other only by the conditions under which weathervaning is assumed to occur. The same MFMHD model run's weathervaning was used in the creation of all five proxies, so it is not the extent of weathervaning that differs between proxies, but rather the conditions under which weathervaning

is “turned on” (assumed and corrected for).

“Proxy a” is another name we have assigned to the original proxy. This proxy assumes that the clock angle observed at 400km is the same as the clock angle of the upstream IMF. It differs from the new proxies in two fundamental ways. First, it ignores weathervaning, instead assuming that field lines drape parallel around the ionosphere. Second, it ignores the seasonal effect of Mars’ ~25° axial tilt. Recall that 0° is defined as local east. All proxies except for proxy a take this seasonal effect, which in MSO coordinates changes the clock angle of local east, into account.

“Proxy b” assumes that weathervaning always occurs in the –E hemisphere, and assumes that weathervaning in the +E hemisphere occurs during the half-year surrounding perihelion, but not during the other half of the year. The reasoning behind this follows directly from our analysis of Fig. 6.4, in which it appears that weathervaning of eastward IMF occurs more during one half of the year. It will be shown that proxy b was the best-performing proxy, and is therefore the proxy that we encourage people to use in future studies requiring an estimate of IMF direction during the period of MGS’s mapping orbit.

“Proxy c” is very similar to proxy b. Like proxy b, it assumes weathervaning occurs for all upstream IMF directions during the half-year surrounding perihelion. For the other half of the year though, rather than assuming weathervaning occurs only for the –E hemisphere, proxy c assumes that weathervaning occurs only for upstream IMF clock angles greater than 90° and less than 270°. This distinction is akin to attributing the hemispheric asymmetry in the extent of

weathervaning to a geographic-coordinate phenomenon rather than attributing it solely to IMF clock angle, so that the asymmetry rotates with the IMF, as is assumed for proxy b. Because the hemispheric asymmetry in weathervaning hinted at in observational data is also visible in the results of this model run which did not include crustal fields, it seems more likely that the asymmetry rotates with IMF rather than being somehow tied to a planetary coordinate system. In other words, the model seems to support the assumption made in proxy b, that the asymmetry is related to the direction of the convective electric field and that this asymmetry should be expected to rotate as the IMF rotate.

"Proxy d" is in one sense the counterpart to proxy a. Whereas proxy a always ignores any weathervaning effects, proxy d assumes (and thus attempts to correct for) the presence of weathervaning for all times of year and for all upstream IMF clock angles.

"Proxy e" assumes weathervaning always occurred at the MGS proxy location for upstream IMF clock angles from 90°-270°, and that weathervaning never occurs for clock angles greater than 270° or less than 90°. Whereas proxy c assumed the less-weathervaned hemisphere experiences weathervaning only near perihelion, proxy e assumes that this hemisphere never experiences weathervaning at all.

"Proxy f" assumes weathervaning occurred at the MGS proxy location when this location was in the –E hemisphere, but not when the proxy location was in the +E hemisphere. In summary, all five new proxies tested assume that one hemisphere always experiences weathervaning. The different proxies simply alter whether the other hemisphere is weathervaned always (proxy d),

never (proxies e and f), or only near perihelion (b and c), and also whether the two hemispheres are defined in MSO coordinates (c and e), or made to rotate with the IMF (b and f). A summary of the various proxies tested is provided in Table 6.2.

	In what hemisphere(s) is MHD-MF weathervaning used during the half-year surrounding perihelion?	In what hemisphere(s) is MHD-MF weathervaning used during the half-year surrounding aphelion?
Proxy a	Neither hemisphere	Neither hemisphere
Proxy b	-E hemisphere and +E hemisphere	-E hemisphere only
Proxy c	MSO "southern" hemisphere and MSO "northern" hemisphere	MSO "southern" hemisphere only
Proxy d	-E hemisphere and +E hemisphere	-E hemisphere and +E hemisphere
Proxy e	MSO "southern" hemisphere	MSO "southern" hemisphere
Proxy f	-E hemisphere	-E hemisphere

Table 6.2. A summary of the proxies we tested. Each proxy represents a different way of determining when and where field lines were assumed to drape parallel, and when and where they were assumed to exhibit weathervaning as seen in the MHD-MF.

We first present a single proxy, to show how these proxies map observations at 400km to an upstream IMF value, and how a proxy varies over the course of a Mars year. Figure 6.7 shows the mapping between upstream IMF angle and the magnetic field angle at 400km altitude for three times of year. Panel a shows once again the magnetic field configuration of the MFMHD run used. Concentric circles have now been added to this plot, showing a projection of the locations from which magnetic field vectors were extracted from the model results in order to create the proxies. It is unreasonable to perform, for example, 360 model runs, each corresponding to a different upstream IMF clock angle, and so for this step of the process we assume that the weathervaning pattern for this run with eastward IMF can simply be rotated to yield the weathervaning pattern for any other upstream IMF angle. For example, to determine the

magnetic field clock angle at 400km altitude when the upstream IMF clock angle is 90°, we first determine the MGS proxy location for that day of the Mars year, and then extract magnetic field values from a point at 400km altitude equidistant from the Mars-Sun line that is located 90° clockwise from the proxy location. Panel a of Fig. 6.7 shows the circle of rotated points for three specific days of the Mars year: northern summer solstice (blue circle), fall equinox (red), and winter solstice (black). Panel b shows proxy b's mapping between upstream IMF angle and magnetic field angle at 400km altitude for these same times of year, with corresponding colors. At winter solstice, when the proxy location is far from the subsolar point and weathervaning effects are stronger, the tendency of many upstream IMF angles to map to the same weathervaned angle at 400km altitude is very strong. This is seen in Fig 6.7b as large regions where the mapping for winter solstice (black line) is nearly horizontal. At summer solstice, when the proxy location is much closer to the subsolar point, where weathervaning effects are less pronounced, this clustering of many upstream values mapping to the same weathervaned angle at 400km altitude is reduced. This demonstrates why *Fedorov et al*. [2006] restrict their IMF clock angle proxy to observation times when MGS was at a low solar zenith angle, specifically, below 60°. At low solar zenith angles a straight-line approximation (as that used in *Fedorov et al*. [2006] or in proxy a) is very close even when the global picture is one of extreme weathervaning. In this study, rather than avoiding large solar zenith angle observations, we retain them so that our improved proxy may be applied to a much larger range of time periods, noting that our steps taking account for weathervaning should allow for reasonably accurate draped IMF mapping even at high solar zenith angles. Another feature of Fig. 6.7 b's summer solstice mapping (blue) is that, for half of all upstream IMF angles, the mapping becomes a straight

diagonal line. This is because the summer solstice falls within the half of the year (near aphelion) when half of all upstream clock angles are not weathervaned by proxy b.

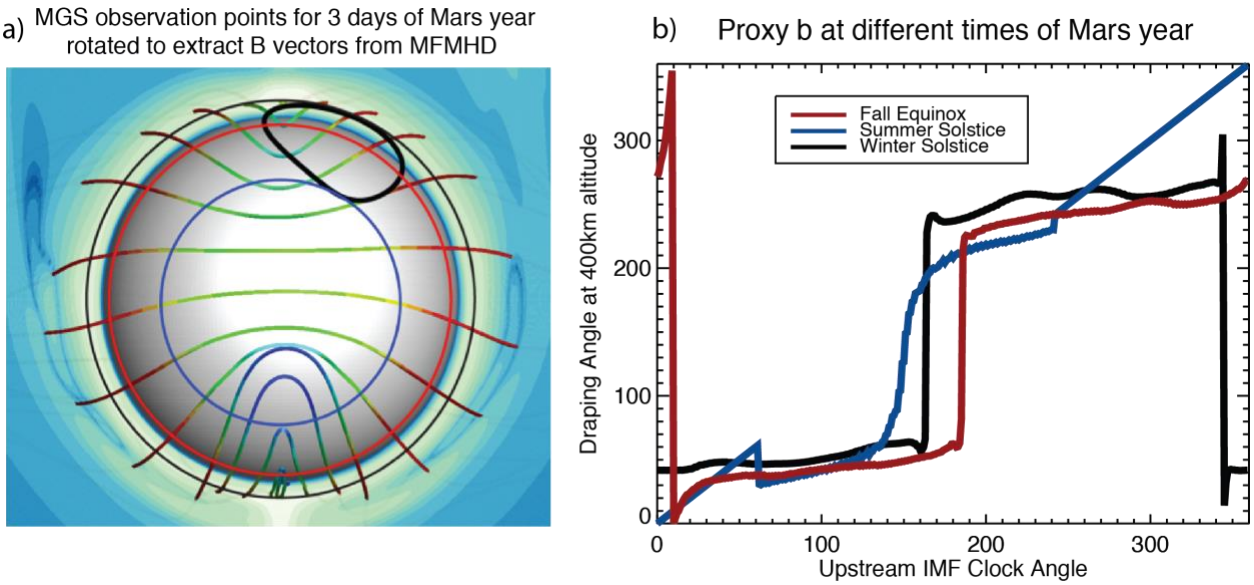

Figure 6.7. Panel a shows weathervaned magnetic field lines from the MFMHD, the path of the MGS proxy location over the course of a year, and also three concentric circles, representing the locations from which magnetic field data was extracted from the model for three specific times of year: northern winter solstice (black), fall equinox (red), and summer solstice (blue). Rather than doing a separate model run for each angle bin of upstream IMF, it was assumed that the draping pattern remains the same but rotated for different IMF clock angles, so all IMF angles can be considered by simply picking the appropriate point on the circle. For each of these times of year, panel b shows the resulting mapping between upstream IMF angle (horizontal axis) and the magnetic field angle taken from the MFMHD at 400km (vertical axis).

A representation of how different proxies can map the same observed magnetic field direction to very different upstream IMF clock angles is given in Fig. 6.8. Each panel in Fig. 6.8 has an azimuthal draping angle on its vertical axis and the corresponding upstream θ_{IMF} on the horizontal axis. The top row in Fig. 6.8 shows the mapping of the original proxy. In this simplest approximation, a straight line mapping is used, with the upstream IMF clock angle assigned by the proxy assumed to exactly match the observed azimuth angle at 400km. The remaining rows in Fig. 6.8 are mappings of the new proxies we tested, all of which rely on weathervaning seen in

the MFMHD. Each row corresponds to a different proxy tested, a different way of mapping observations at 400km to what the upstream IMF clock angle may have been. Because all proxies except for the original take into account how the location of the MGS observation location changes over the course of a Mars year, two columns are shown, corresponding to two different days of the Mars year. The left column shows how each proxy maps 400km observations to upstream IMF angle at Mars' northern summer solstice, while the right column shows this mapping for Mars' northern fall equinox. A nearest-value approach was used in generating the new proxies, such that the upstream θ_{IMF} assigned to each orbit was the clock angle (horizontal axis in Fig. 6.8) whose corresponding azimuthal angle from the MFMHD result (vertical axis) most nearly matched the MGS observed azimuth angle. If we reimagine these mappings as 360 points rather than a solid line, this process can be thought of as taking a specific MGS measurement at 400km, finding that point on the vertical axis of the mapping, and setting the estimated upstream clock angle equal to the value on the horizontal axis of the point nearest that position on the vertical axis.

In short, the steps to creating our new proxies were as follows:

1. Determine the location in MSO coordinates of the 2pm 400km 55°N MGS proxy location for each 24-hour period in Mars year.
2. Extract from zero-crustal-field MFMHD results the magnetic field vector at this location.
3. Choose whether to define draping azimuth as the angle from east in a horizontal plane or as the angle from $+Y_{MSO}$ in an MSO y-z plane.
4. For proxies utilizing a "straight line" approximation (no weathervaning) for some seasons and clock angles, bypass the MFMHD entirely for those times and assume parallel field

line draping. In all other cases, assign upstream clock angle from MFMHD azimuths using a nearest-value approach.

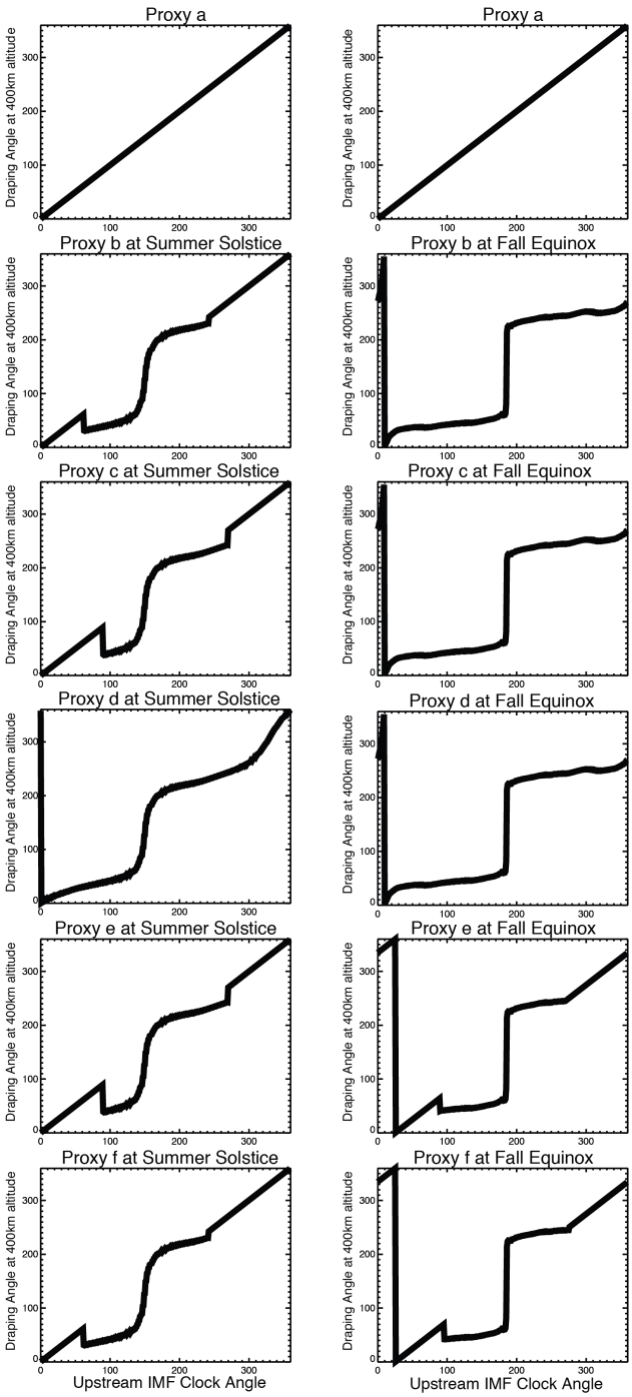

Figure 6.8. Mappings between 400km-altitude (draped) magnetic field and upstream θ_{IMF}. Each panel has an azimuthal draping angle on its vertical axis and the corresponding upstream θ_{IMF} on the horizontal axis. The top row shows the parallel draping assumption of

the original proxy, proxy a. The remaining rows each correspond to one of the new proxies we tested. Because some of the proxies only differ from each other during portions of a Mars year, two columns are provided. The left column shows the mapping of each proxy at northern summer solstice. The right column shows this mapping at fall equinox.

6.7 Proxy Performance

Evaluation of the performance of each of the proxies was done by seeing how well each proxy organized a particle population whose behavior is known to be controlled by θ_{IMF}. An energetic plume of heavy planetary ions is known to be picked up by the solar wind and accelerated in the $+E_{SW}$ direction with particle energies that extend into the tens of keV (e.g. *Dong et al.*, 2015).

This population of pickup ions has been referred to variously as a "polar plume" or an "energetic plume," and in addition to being predicted by particle tracking models (e.g. *Curry et al.*, 2013a) and hybrid models (e.g. *Kallio and Koskinen*, 1999; *Boesswetter et al.*, 2004; *Modolo et al.*, 2005) which account for finite gyroradii effects, it has been seen observationally in case studies (e.g. *Dubinin et al.*, 2011; *Edberg et al.*, 2009; *Liemohn et al.*, 2014) and in statistical studies (e.g. *Johnson et al.*, 2017; *Dong et al.*, 2015). This entire body of research suggests that in Mars-Solar-Electric field coordinates, a clear asymmetry exists in the Mars space environment in which the +E direction contains far greater fluxes of heavy energetic planetary ions than the –E direction, particularly at altitudes above the main source population. The present study makes use of this known asymmetry by assuming that the proxy producing the clearest asymmetry in

that proxy's version of MSE coordinates is in fact the proxy best able to infer upstream IMF clock angle based on the available observations at 400km.

Figure 6.9 maps the location of heavy ions detected by the Ion Mass Analyzer (IMA) aboard Mars Express at energies (2-15keV) that would be difficult to obtain by particles not accelerated by E_{SW}. The ion data shown here was processed in the same way that data was processed in chapter 5. One key point in this regard is that only observations outside of the statistical induced magnetosphere boundary are included. This means that the data are taken at high altitudes where the heavy ion asymmetry should be clear even without considering flight direction, since in the –E hemisphere pickup ions will get accelerated toward the planet rather than out to even higher altitudes. Another important point is that, at the post acceleration voltage setting of the instrument that was used, there exists a mass and energy range that is typical of the energetic plume while also being a mass and energy range for which "ghost counts" (an instrumental effect whereby protons bouncing inside the detector lead to false heavy ion counts) are negligible. Every panel in Fig. 6.9 is in a Mars-Solar-Electric field coordinate system in which the location of ion observation has been rotated around the MSO x-axis until the direction of E_{SW} is aligned with the vertical axis. This act of rotation is in fact the only thing distinguishing each row of Fig. 6.9 from the others. Each row contains the exact same Mars Express ion data collected during the time when the lifespans of MGS and MEX overlapped, and each row rotates into MSE coordinates by using its own unique estimate of what the direction of θ_{IMF} (and hence E_{SW}) was for at the time of each ion measurement. The left column of Fig. 6.9 is the view from the sun integrated along x. The right column is a view from the side integrated along curves of constant cylindrical radius, in which the color scale shows the difference between the $+E_{SW}$ quarter-

cylinder and the $-E_{SW}$ quarter-cylinder. The median count rate of the $-E_{SW}$ quarter cylinder has been subtracted from the median count rate in the $+E_{SW}$ quarter cylinder, so that reds signify plume regions where heavy energetic planetary ions were seen more in the direction estimated to be the $+E_{SW}$ direction and regions in blue are locations where these ions were seen more in the direction estimated to be the $-E_{SW}$ direction. Each row corresponds to one of the θ_{IMF} proxies tested, with the top row corresponding to the original proxy we set out to improve upon. A qualitative examination of Fig 6.9 reveals that proxies b, c, and d, with their high median count rates in the direction of the estimated electric field, appear to do the best job of organizing plume-energy ions in an MSE coordinate system, but it is not possible using only Fig. 6.9 to determine which proxy is best at creating an MSE coordinate system.

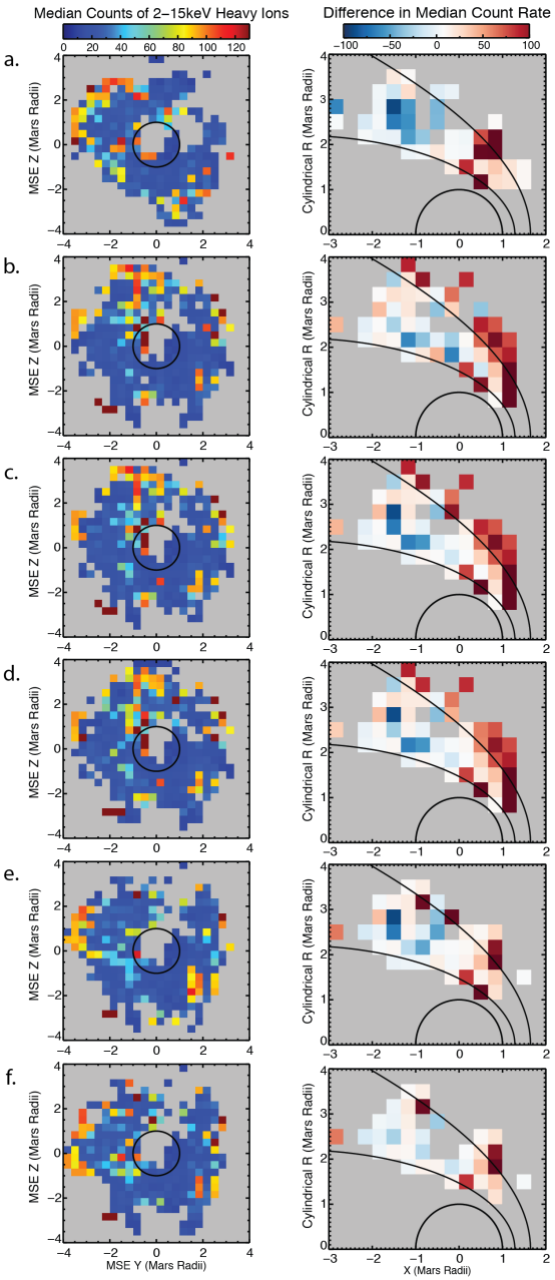

Figure 6.9 Each row represents a different proxy and uses its own estimate of θ_{IMF} to rotate plume type ion data into a Mars-Sun-Electric Field coordinate system in which the vertical axis is aligned with the direction of $+E_{SW}$. Both columns give information regarding the median count rate of 2-15keV heavy ions. The first column gives the view from the sun, integrated along x, with the color of each bin showing the medium IMA count rate. The second column is a difference plot in MSE cylindrical coordinates, in which the color of each bin shows the value remaining when the $-E_{SW}$ cylindrical quadrant's median count rate is subtracted from the $+E_{SW}$ cylindrical quadrant's count rate. Red (blue) bins correspond to regions of higher (lower) count rates of plume-type ions in the direction estimated by each row's proxy to be the direction of $+E_{SW}$.

A more direct and quantitative proxy vs. proxy comparison is given in Figure 6.10. The horizontal axis is a "cutoff" number of counts of 2-15 keV heavy ions during one full 192-s sweep of the MEX Ion Mass Analyzer. The vertical axis shows the fraction of observations in the $+E_{SW}$ quarter cylinder for which more than the cutoff number of counts was observed. Note that these probability distributions are created from all MEX IMA measurements during the MEX-MGS mission overlap (that is, for which there was a clock angle proxy), not just from the binned median values shown in Figure 6.10. The exact number of measurements in the probability distribution is slightly different for each curve because each proxy has its own mapping from a measurement location into MSE coordinates. We make the assumption that a proxy that is more successful in estimating θ_{IMF} and hence $+E_{SW}$ will have an increased likelihood of detecting plume-type ions in that proxy's $+E_{SW}$ quadrant, thereby causing the curves of the more successful proxies to be consistently above the more mediocre proxies in Fig. 6.10. By this measure we see that, while some of our attempted new proxies (proxies e and f) are no better than original proxy (black curve in Fig. 6.10), some do considerably better (as also seen qualitatively in Fig. 6.9). Proxy d performed very well simply by assuming a MFMHD-produced weathervaning at all times and for all upstream IMF clock angles. Proxy b, which assumed weathervaning occurred year-round when the MGS measurement feeding the proxy (i.e., at 50-60˚ north latitude) was made in the $-E_{SW}$ hemisphere and occurred only during the half-year

surrounding perihelion when the measurement was made in the +E_{SW} hemisphere, outperformed all others.

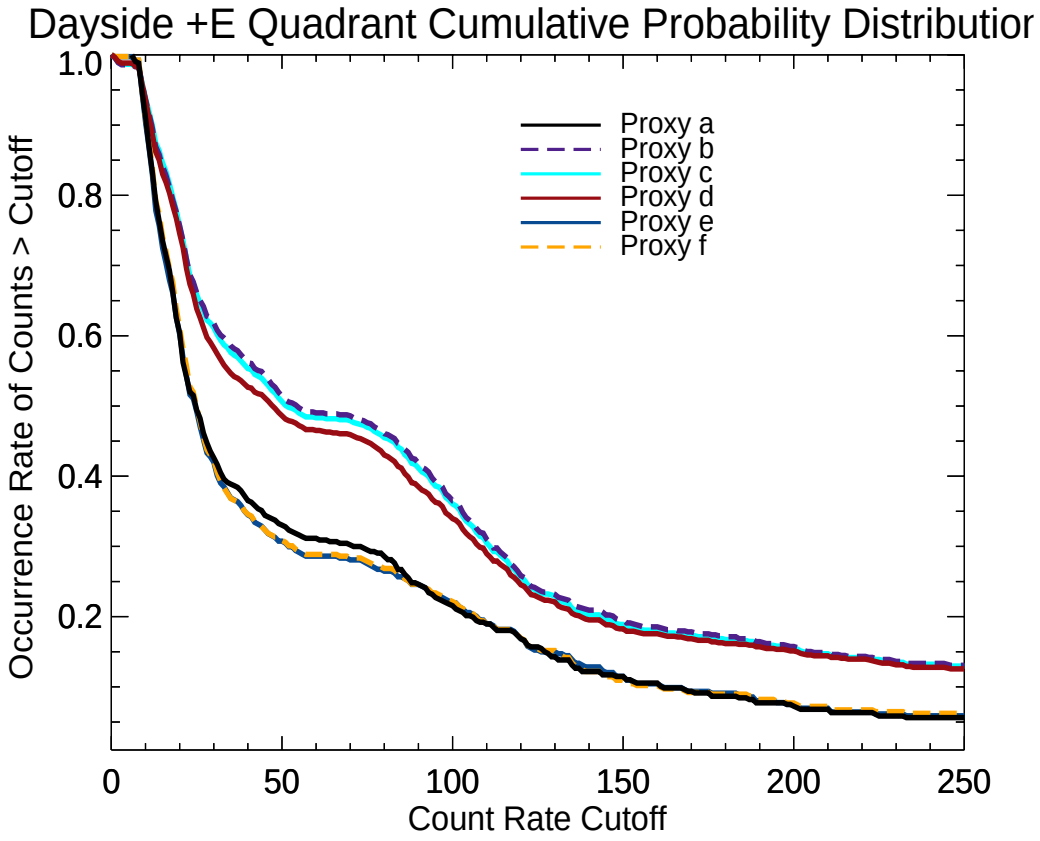

Figure 6.10. Cumulative occurrence frequency of energetic plume type ions detected within the cylindrical quadrant that was determined by each proxy to be the +E_{SW} quadrant. Each line corresponds to one of the θ_{IMF} proxies tested. Example of how to read the plot: the original proxy's +E_{SW} quadrant (black line) saw greater than 70 counts of plume-type ions about 30% of the time, while proxy b's +E_{SW} quadrant (purple dashed line) saw greater than 70 counts about 50% of the time. This serves as a method of ranking the performance of the proxies.

6.8 Discussion and Conclusions

Mars' induced magnetosphere is organized by the direction of the convective electric field. The original proxy, or "proxy a," developed by Dave Brain and discussed in *Brain et al.* [2006a] has

been used numerous times to gain insight into this induced magnetospheric system [e.g. *Brain et al.*, 2006b; *Briggs et al.*, 2011; *Carlsson et al.*, 2008; *Dieval et al., 2014*; *Dubinin et al.*, 2008; *Halekas et al., 2006*; *Nilsson et al., 2011*; *Wang et al., 2013*; *Johnson et al.*, 2017]. These past studies could be revisited with the use of our improved upstream IMF proxy. A yet-unwritten study concerning how plume escape rates varied with external drivers during the time of MEX-MGS overlap should use our improved proxy, and will be a useful companion to *Dong et al.* [2017]'s examination of plume escape variation with drivers during MAVEN's first months at Mars. In addition to these uses of the proxy, which can be useful in organizing and interpreting ion behavior during the time period MEX-MGS overlap, this improved proxy could be used with more up-to-date observations. If, for example, MAVEN's apoapsis is in the tail, providing no upstream solar wind observations, but dayside low altitude observations are available, the present study may inform interpretation of these low-altitude dayside magnetic field measurements when attempting to estimate upstream θ_{IMF}.

The use of MHD-MF results that account for weathervaning but not for crustal field effects generated an improved proxy. This suggests that, despite the important role played by crustal fields in mediating interaction between the solar wind and the Martian ionosphere, the mass loading of magnetic flux tubes and bending of draped magnetic field lines (i.e. weathervaning) still plays a role in the Martian induced magnetospheric system.

One issue not directly addressed by this study is the underlying cause of the finding that, for some set of upstream IMF clock angles mapping between ~300°-90°, weathervaning occurred more during one half of the year than during the other half of the year. This trend, which is

somewhat apparent in Fig. 6.4, and which is supported by the fact that selective weathervaning produced the best-performing proxy, has at least two possible explanations. The most likely explanation is that weathervaning occurs less in the $+E_{SW}$ hemisphere, as was seen in the MHD-MF results. The other possibility is that, due perhaps to crustal field interactions, weathervaning occurs less when the IMF is directed eastward, and that this only happens to correspond to MGS being in the $+E_{SW}$ hemisphere because of the 50°-60°N latitude band chosen as the proxy location.

Another remaining question involves the nature of the seasonal periodicity of whether weathervaning is observed in the $+E_{SW}$ hemisphere (or, as discussed in the previous paragraph, perhaps we should say the northern latitude hemisphere). The trend seen in Fig. 6.5 indicating that these IMF clock angles weathervane more during times of high EUV flux fits nicely into a narrative of increased mass-loading and weathervaning near perihelion, but examining the bottom half of Fig. 6.4 gives one the impression that this oscillation peaks at azimuth angles of about 60° some time shortly *after* perihelion. It is possible that a more complete explanation of the data may be that the exact seasonal location of this peak is a compromise between the time of perihelion, when even the $+E_{SW}$ hemisphere experiences heavy weathervaning, and the time between winter and spring when the seasonal MSO position of the proxy location tends to cause the greatest increase in observed azimuth angle.

Our study included examining how observed draping changes with both subsolar pressure and with EUV flux. We note that there is a potential problem with this type of analysis: subsolar pressure and EUV flux are not completely independent variables. Both EUV flux and solar wind

density fall off as heliocentric distance squared, raising the question of whether any trends seen in one of these variables is in fact due in part to the other. *Halekas et al.* [2017] contains a good discussion of the potential pitfalls of failing to control for all variables in such situations. Due to this concern, we created replicas of Fig. 6.5 showing draping correlation with EUV flux for specific pressure ranges as well as replicas of Fig. 6.6 showing draping correlation with EUV flux for specific ranges of EUV flux. The most obvious trends in Fig. 6.5 and Fig. 6.6, which are the trends discussed previously, remained under this closer examination. For narrow ranges of subsolar pressure, increased weathervaning of eastward IMF was observed to correlate with EUV flux. For narrow ranges of EUV flux, increasing subsolar pressure was associated with greater balance between the 240° weathervaned direction and the 60° weathervaned direction, suggesting that the remarkably dense clustering of observed azimuths near 240° may be caused by crustal fields that tend toward 240° azimuths ballooning all the way out to 400km altitude during times of low upstream dynamic pressure.

Our assertion that crustal fields are likely impacting MGS proxies θ_{IMF} is not new. As discussed in the introduction, several recent studies suggest that crustal fields sometimes influence magnetic field observations at the θ_{IMF} proxy location (*Luhmann et al*., 2015, *Ulusen et al*., 2016, *Xu et al.*, 2017). Armed with the hindsight provided by these studies, one may begin to notice features in the data of older publications that are consistent with what such crustal influence would probably look like. Figure 2 in *Halekas et al.* [2006], which shows that observed draping azimuths on the dayside correspond to specific magnetic field directions in the magnetotail, contains an asymmetry that could be explained as being the result of 240° azimuths sometimes being recorded during what was actually eastward IMF due to crustal field influence. Figure 7 of

Brain et al. [2006] demonstrates that the strong clustering around 240° seems to occur across all latitudes, however the crustal fields in this latitude band are fairly homogenous, and this same figure shows an increase in the frequency of observing azimuths of about 50° at 75 east longitude, which above 30°N latitude is the only longitude with significant radially outward crustal fields (e.g. plate 2 in *Acuña et al*., 2001). This is consistent with a picture of proxy location observations sometimes seeing crustal fields blown back away from the subsolar point rather than draped fields organized toward or away from the subsolar point. If the "blown back" crustal field has a radially outward component, as at 75 east longitude, it would be observed at the proxy location to have an azimuthal angle of about 60°, whereas such a crustal field line had a radially inward component we would expect to observe an azimuthal reading of about 240°. A final example of evidence for crustal field influence hidden in earlier publications is Figure 4c in *Brain et al.* [2005]. This figure shows that, during the time of year surrounding aphelion, MGS observed magnetosheath electrons less frequently when the draping azimuth measured was near 240°. This was sensibly interpreted as an indication that specific IMF clock angles result in a higher magnetic boundary at the proxy location. In light of the present study's discussion of the effects of pressure on draping azimuth direction, an alternative explanation arises. Suppose that low-pressure conditions do sometimes result in crustal field influence rising to 400km so that other IMF clock angles appear to have a draping azimuth of 240°. If this is true, then among observations of azimuths near 240°, low pressure time periods would be over-represented. This would be sufficient to lead to the result that sheath electrons are seen less when an azimuthal angle near 240° is observed.

We explored the behavior of magnetic fields at 2pm, 400km altitude, 50°-60°N latitude, and found that weathervaning of draped field lines similar to what was first seen by Pioneer Venus

Orbiter appears to play a role at Mars. Despite the complications introduced by the presence of crustal fields at Mars, the concept of weathervaning retains some predictive power concerning how field lines rotate in the upper atmosphere. Both scatterplots of draping azimuth vs. season and plots showing the draping azimuth direction as a function of ionizing solar flux produce results suggesting that eastward IMF causes weathervaning at the proxy location less consistently than westward IMF does, and that this observed weathervaning of eastward IMF is more likely to occur during times of high EUV flux, when a strengthened ionosphere can cause mass loading for field lines that do not dive as deeply into the atmosphere. Trends of draping azimuth vs. subsolar pressure presented here, taken in conjunction with evidence of crustal field influence at 400km seen in other studies, suggest that a clustering of observed azimuths at 240° is likely the result of crustal field influence, and that the crustal field influence is most pronounced during times of low subsolar pressure. Although no attempt was made to correct observations for crustal field influence, simply taking seasonal weathervaning effects into account allowed for the creation of demonstrably improved proxy for what the direction of the upstream IMF is prior to contact with the Martian ionosphere. This improved θ_{IMF} proxy, proxy b, can be applied to the entire 7.5-year time period during which MGS was in its mapping orbit and no upstream magnetic field observations are available. The improved proxy, in the form of a clock angle estimate for most MGS orbits and a corresponding time stamp, will be made available to any interested party who contacts the author.

Chapter 7: Energetic Plume Variation With Drivers

In order to enable an eventual complete picture of time-integrated atmospheric escape, one goal of researchers must be to determine how each escape channel changes for various solar conditions. In 2017, Y Dong et al. published a study of how the energetic plume's escape fluxes change with EUV flux. Total ion escape was divided into flux through two planes, one at x=-1.6 R_M (tail escape), and the other at Z_{MSE}=+1.6 R_M (plume escape). This study found that, while total escape was indeed higher during periods of higher EUV flux, fluxes in the energetic plume (O^+ fluxes > 6eV through the Z_{MSE}=+1.6 R_M plane) were not greatly affected. This result is counterintuitive because enhanced EUV fluxes should increase both the exospheric neutral source for pickup ions and the rate at which these neutrals become ionized. Of the two time periods used in Dong et al. [2017], the one nearer solar maximum (the high-EUV time period) was also the time period nearer to Mars' southern summer. Brain et al. [2005] found that during southern summer, when the strongest crustal fields are positioned nearer the subsolar point, ion escape fluxes appear to decrease, probably due to a shielding effect of the crustal fields. It is likely, or at least entirely possible, that the conclusion drawn in Dong et al. [2015], that moderate EUV variation has little effect on plume fluxes, is correct. However, given that it was the first study of its kind, and that the result is both counterintuitive and open to reasonable criticism concerning factors unaccounted for, Mars Express' Ion Mass Analyzer and its observations of time periods unseen by MAVEN should be seen as a valuable asset to help address the question

of how EUV variation impacts the plume. Other factors that may impact plume escape rates, such as upstream solar wind dynamic pressure, may also be considered.

7.1 Preliminary Results

An initial glimpse at how EUV fluxes and solar wind pressure may alter energetic plume pickup ions observed by IMA is shown in figures 7.1 (EUV) and 7.2 (pressure).

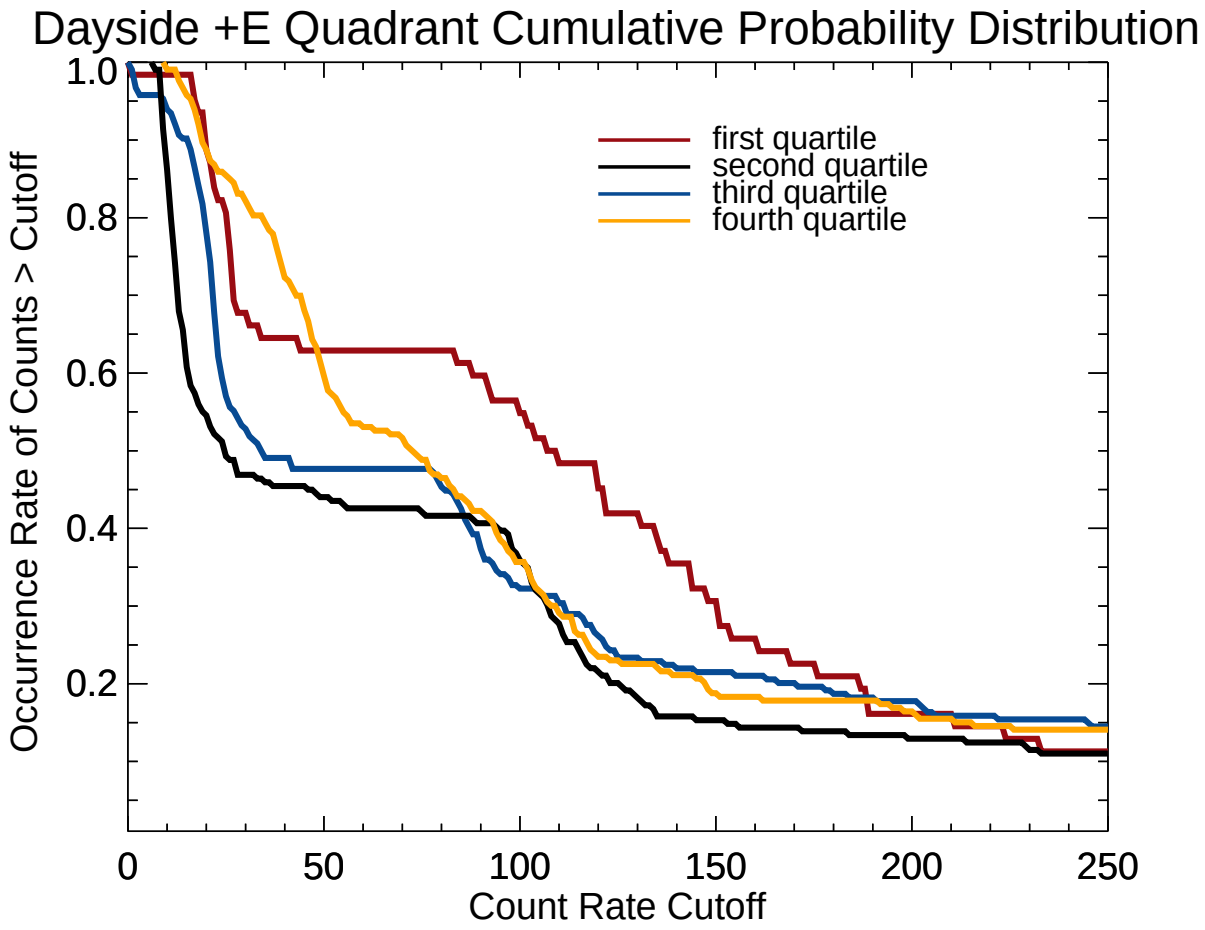

Figure 7.1. Cumulative probability distributions for lowest (red), 2nd lowest (black), 2nd highest (blue) and highest (orange) quartiles of a proxy for EUV flux. The vertical axis shows the

percentage of the time that IMA observed at least as many 2-15 keV heavy ions as is shown on the horizontal axis. Only data from the $+E_{SW}$ quadrant dayside are included.

IMA observations during the time period for which our improved MGS-derived estimate for the direction of E_{SW} are available were divided into four bins based on estimated EUV flux. The data was put into MSE coordinates using the best-performing proxy (proxy b) described in chapter 6. The energetic plume is located primarily on the dayside and in the direction of E_{SW}, so observations taken on the dayside and in the $+E_{SW}$ quadrant were selected. Fig. 7.1 is a cumulative probability distribution using those observations and displaying the percentage of the time that IMA saw at least as many counts of 2-15 keV heavy ions as is shown on the horizontal axis. Horizontal portions of the figure correspond to ranges of count rates that were rarely observed. The bimodal distribution of count rates discussed in chapter 5 is clearly visible in Fig. 7.1 in the flatness of the lines near count rates of ~50-100. Recall that this is what led to the use of a cutoff of >70 counts of 2-15 keV heavy ions as an indicator of when an ion beam is present. 192-second data sweeps that observed fewer than this amount tend to show their counts scattered across all income flight directions, whereas the other peak of the bimodal distribution, above the loose ~70 count threshold, tend to include a focused beam of ions in addition to the scattered signature. With this in mind, the most striking feature of Fig. 7.1 is that more beams of energetic

heavy ions were seen during the times estimated to have had the lowest amount of EUV flux (red line).

Figure 7.2 was created in exactly the same manner as Fig. 7.1, with the exception that the data has now been binned into quartiles based on a proxy for solar wind dynamic pressure.

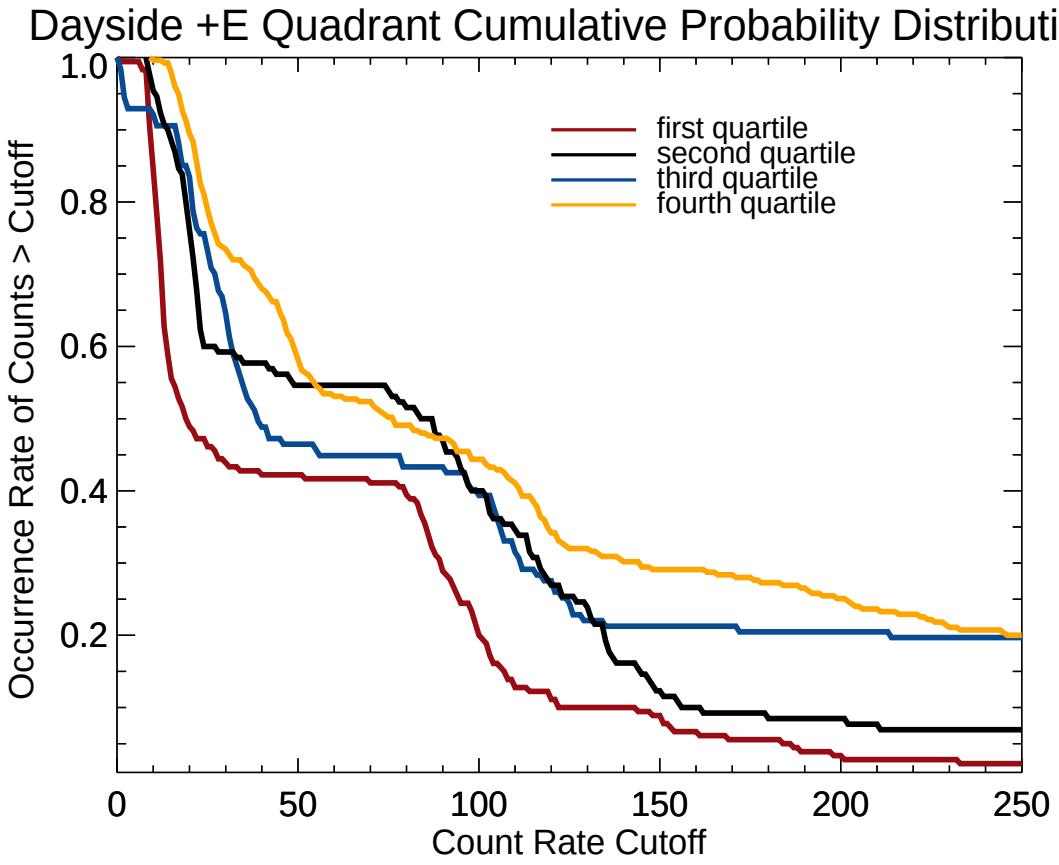

Figure 7.2. Cumulative probability distributions for lowest (red), 2nd lowest (black), 2nd highest (blue) and highest (orange) quartiles of a proxy for solar wind dynamic pressure. The vertical

axis shows the percentage of the time that IMA observed at least as many 2-15 keV heavy ions as is shown on the horizontal axis. Only data from the +E_{SW} quadrant dayside are included.

Fig. 7.2 appears to suggest the possibility that the energetic plume increases in strength as the incident solar wind pressure increases. Times from the lowest quartile of estimated pressures were by far the least likely to see energetic heavy ion beams, while times from the highest quartile of estimated pressures had the greatest likelihood of observing a strong ion beam. While this is likely to be a real physical effect (high dynamic pressures and high magnitudes of the E_{SW} that accelerates plume ions are both associated with high solar wind speeds), other possible explanations have not yet been ruled out. One such possible explanation for the observed pattern in Fig. 7.2 is that, rather than increasing pressures causing a stronger plume, increased pressures simply push crustal magnetic fields to lower altitudes, allowing our estimate for the direction of E_{SW} to be more accurate.

7.2 Discussion

Because the accuracy of the estimated direction of E_{SW} may vary with drivers, tackling the problem of plume variation with these same drivers will be a complex – and ultimately inexact – task. One initial attempt at addressing the question raised at the end of section 7.1, whether increased pressure increases plume strength or simply improves our estimate of where the plume is located, is shown in Table 7.1. If the differences seen in Fig. 7.2 were due solely to certain pressure conditions improving the IMF angle proxy that was used, then those differences should vanish when looking at all clock angles rather than only at the clock angles in which we expect

to see the plume. The fact that ordering of the pressure quartiles in table 7.1 (with the 1st and then 3rd quartiles showing lowest likelihood of energetic ion beam observation) suggests that the trends seen in the $+E_{SW}$ quadrant hold true for near-Mars space generally, suggesting that differences between pressure proxy bins depicted in Fig. 7.2 is probably not due purely to possible pressure effects on the IMF proxy. Similarly, the ordering of EUV quartiles by ion beam incident rate is the same for all clock angles (Table 7.1) as it is for the $+E_{SW}$ quadrant dayside (Fig. 7.1). It can be noted that the ordering seen in Fig. 7.2, from least likely to observe ion beams to most likely, changes to a well-organized 1st, 2nd, 3rd, then 4th pressure quartile ordering in the tail of the distribution. Closer examination should include verification of whether this ordering seen in the tails of the distribution in the $+E_{SW}$ quadrant holds true when considering all spatial quadrants.

	1st pressure quartile	2nd pressure quartile	3rd pressure quartile	4th pressure quartile	1st EUV quartile	2nd EUV quartile	3rd EUV quartile	4th EUV quartile
% of data sweeps with > 70 counts of 2-15 keV heavy ions	27%	32%	29%	32%	38%	20%	29%	31%

Table 7.1. The likelihood of observing > 70 counts of 2-15 keV heavy ions anywhere in near-Mars space for various solar conditions

A thorough analysis of how energetic plume loss rates vary with drivers should soon examine total outward flux through a surface. Whether this surface should be used as a definition of what is plume escape and what is "tail" escape (as was done in *Dong et al.* [2017]) is debatable. It may be argued that defining the plume based on energy per particle makes as much or more sense. In

defense of Dong et al., it may be pointed out that, unlike the case of the Earth's magnetosphere where energy-based definitions of particle populations (radiation belts, ring current, plasmasphere) have arisen in part because these populations can be co-located, most planetary ion flux through the plume-defining planes of Dong et al. had no way of getting to that point in space without being accelerated by the solar wind's convective electric field, and are therefore energetic plume ions by any definition. Due to the energy constraints imposed by the avoidance of ghost counts (Fig 3.1) which make statistical studies of low energy ions outside of the MPB using IMA data, defining the plume based on flux surfaces rather than on energy is the most viable way to proceed.

An additional step that should be taken before these results are worthy of publication in major journal is to ensure that the proxy used for EUV flux at Mars is the best proxy available. *Thiemann et al*. [2017] describes a Flare Irradiance Spectral Model (FISM) that can be applied at Mars (FISM-M) that uses multiple indices (as opposed to simply F10.7) to generate a spectrum of all ionizing solar radiation. Their work may better capture the EUV environment to help form initial understandings of how the energetic plume varies (or doesn't) with EUV.

Chapter 8: Broader Discussion

In chapter 2, the process of determining the amount of oxygen that has escaped over time was broken down into three parts: observing current escape rates, determining escape rate variation with drivers, and estimating how these drivers have changed over time. This method works particularly well for slow and steady loss processes. Processes resulting in the rapid escape of large quantities of particles should not escape consideration. A primary example of such event-based atmospheric loss is escape to due to meteorite impact. It is possible that large impact events, such as comet and asteroid collisions with Mars, have played a significant role in the total time integrated atmospheric loss (e.g. *Frey*, 2006). Another source of rapid atmospheric escape that may be viewed as event-based rather than ongoing are Coronal Mass Ejections, or CMEs. Like large impact events, the effects of CMEs on ion escape is still largely unknown. Escape rates during the sheath phase of the passage of a CME have been estimated to be an order of magnitude higher than ion escape rates during nominal solar wind conditions (*Curry et al*., 2015; *Dong et al*., 2015), while other estimates found no significant change in escape rate during a CME (*Ramstad et al*., 2017). Although the specific energization processes associated with CMEs may be argued to be the same processes outlined in chapter 3, processes that are simply temporarily enhanced by a CME, it can be useful to treat loss due to CMEs separately. CMEs are thought to have been much more common when the sun was a younger, more active star. The increased frequency of these events in the past is mostly easily taken into account in time-integrated escape estimates if escape during CMEs is considered separately.

How does this dissertation fit into the long- term goal of estimating the total quantity of particles that have been lost from Mars' atmosphere? What has this work accomplished? In the time since the work presented in this dissertation was begun, the Mars Atmosphere and Volatile EvolutioN (MAVEN) spacecraft has arrived at Mars, equipped with a larger suite of plasma instruments than MEX has, instruments specifically designed to study the upper atmosphere of Mars and its interaction with the solar wind. It has been found that the current escape rate of neutral oxygen, estimated to be ~$\mathbf{5 \times 10^{25}}$ (*Rahmati et al*., 2017; *Lillis et al*., 2017), may exceed present day ion loss rates, which have been given a lower bound of ~$\mathbf{3 \times 10^{24}}$ ions per second (*Brain et al*., 2015). This estimate only includes ions with energies >25 eV, far higher than ~2 eV required for oxygen to escape; the total ion escape rate may well be significantly higher than this lower bound. Also in the time since this dissertation work was begun, the arrival of MAVEN's magnetometer has raised some questions concerning the usefulness of chapter 6's improved IMF draping proxy for the time period of the MGS mapping orbit. Chapter 5's statistical study of the energetic plume – though vastly superior to the initial statistical study seen in chapter 4 – has been upstaged by *Y. Dong et al*. [2015]'s clear portrayal of the energetic plume with highly accurate E_{SW} directions based on MAVEN magnetometer measurements made directly in the solar wind. And something on the order of ~$\mathbf{10^{33}}$ oxygen ions have escaped from the Martian planetary system into deep space. If it is assumed that all of this oxygen came from water, which has a molecular mass of ~ $\mathbf{3 \times 10^{-26}}$ kg/molecule, this is the equivalent of about $\mathbf{3 \times 10^{7}}$kg of water. This equal to the amount of water in 12 Olympic-sized swimming pools, or a large pond.

So where does the research presented here fit in? One way to answer this question is depicted in Table 8.1, where the work described in chapters 4 and 5 occupy one cell of a table of the

growing collection of knowledge concerning Mars ion escape (references 10 and 11 in the table). Another way of answering the question of where this dissertation's research fits, in light of the superior relevant capabilities of MAVEN's instrument suite as compared with that of Mars Express, is with a reminder that more data is almost always better. MAVEN is scheduled to alter its orbit to prioritize its role as a relay for rovers on the Martian surface over its role as an observer of atmospheric escape. This means that, all told, MAVEN's best data is expected to cover less than one complete solar cycle. One example of the potential pitfalls of insufficient data was discussed briefly in chapter 5, where it was noted that a variation in energetic plume fluxes that was attributed to changes in EUV flux may have actually been due in part to a change in season, as southern summer places the strong crustal fields of Mars' southern hemisphere nearer to the subsolar point, where they act as a better shield to ion escape. Of course, the many factors that influence escape rates do not have the same periodicities. A Mars year, for instance, is not as long as a solar cycle. Thus, when data is gathered over longer periods of time, it becomes far easier to reliably isolate the effects of one particular factor, allowing for more accurate extrapolation of loss rates backward in time. (Even with complete knowledge of how EUV flux behaved billions of years ago, estimates of time-integrated oxygen loss require not only knowledge of how EUV changed, but also knowledge of how changes in EUV influence loss rates). Viewed in this way, the statistical study presented in chapter 5, by demonstrating energetic plume observations can in fact be teased out of MEX IMA data, is useful in that it opens up an additional time period (the time period of MEX-MGS overlap) that may be studied to improve estimates of how drivers influence loss rates. The improved IMF proxy that was the topic of chapter 6 is valuable for this same reason.

Spacecraft Name	Orbital Insertion or (flyby date)	Observed evidence of past water	Energetic plume observations	Ion escape rate estimates
Mariner 9	Nov. 14, 1971	Erosion patterns consistent with flooding[1,2]		
Viking 1	June 19, 1976	Further evidence of outflow channels[3] and Suggested evidence of shorelines[4]		
Phobos 2	Jan. 29, 1989		energetic planetary ions outside of the MPB[5]	$\sim \mathbf{2 \times 10^{25}}$ ions/s [6]
Mars Global Surveyor	Sept. 12, 1997	MOC imager onboard MGS fails to find supporting evidence for proposed shorelines[7]		
Mars Odyssey	Oct. 24, 2001	Gamma Ray Spectrometer detects elemental distributions of potassium requiring fractionation "consistent with aqueous activity."[8]		
Mars Express	Dec. 25, 2003		Plume observation case studies[9,10] Statistical plume observed[11]	$\sim \mathbf{2 \times 10^{24}}$ ions/s [12] $\mathbf{1.8 - 5.6 \times 10^{24}}$ [13]
Mars Reconnaissance Orbiter	March 10, 2006	Evidence of hydrated minerals such as clays[14]		
Rosetta	(Feb. 24, 2007)		energetic planetary ions outside of the MPB[15]	
MAVEN	Sept. 12, 2014		Statistical plume [16]	$\sim \mathbf{3 \times 10^{24}}$ ions/s [17,18]

Table 8.1. Not intended to be a complete list of the relevant research, merely a tidy timeline of sorts. References: (1) *McCauley et al*., 1972; (2) *Baker and Milton*, 1974; (3) *Lucchitta et al*., 1986; (4) *Parker et al*., 1993; (5) *Kallio et al*., 1995 (6) *Lundin and Dubinin*, 1992; (7) *Malin and Edgett*, 1999; (8) *Dohm et al*., 2009; (9) *Dubinin et al*., 2011; (10) *Liemohn et al*., 2014; (11) Johnson et al., 2017; (12) *Nilsson et al*., 2012; (13) *Ramstad et al*., 2015; (14) *Mustard et al., 2008*; (15) *Edberg et al*., 2009; (16) *Dong et al*., 2015; (17) *Brain et al*., 2015; (18) *Dong et al*., 2017

The work performed to create the improved IMF proxy is valuable for other reasons as well. The

majority of literature discussing the “weathervaning” of field lines is on the topic of the induced magnetosphere of Venus. Chapter 6’s demonstration that a directing of low altitude magnetic field lines roughly toward or away from the subsolar point occurs at Mars both in simulations and in observations is therefore useful in helping to round out understanding of magnetic field configurations in the Mars space environment. Additionally, as the question is addressed of exactly why it is that one hemisphere experiences significantly more weathervaning than the other, further insight into ionospheric draping and induced current systems might be gained. Finally, chapter 6 also succeeds in adding yet another piece of evidence to the body of literature pointing toward heavy crustal field influence of magnetic field configurations near ~400km altitude.

Chapter 9: Conclusions and Future Work

9.1 Summary of the Work Performed

The chapters of this dissertation stitched themselves together more easily than may be the case for many dissertations, because the progression from one research project to the next flowed very naturally, with each building on the project that came before. Chapter 4 reported the identification of specific incidences of energetic heavy planetary ion observations that were remarkably consistent with what had been predicted by models while also raising questions about whether the obstacles to plume observations using IMA might be too great and too numerous to overcome. Chapter 5 overcame these obstacles, with a methodology better able to screen out ghost counts, control for time variation of the upstream IMF clock angle, identify an appropriate cutoff for when the count rate of heavy ions was above the background level, and display data only in spatial bins with a more significant number of observations. Out from remaining uncertainties surrounding the accuracy of the MGS derived IMF proxy (used to organize the statistical observations in chapter 5) sprouted ideas for how this proxy might be improved upon. This was accomplished in chapter 6, along with the added bonus of a deeper understanding of magnetic field configurations in the upper atmosphere of Mars. With the IDL code structure then in place for more reliably estimating the direction of E_{SW} and also for generating Mars-Solar-Electric field plots of clean IMA data using this E_{SW} estimate, the ground was finally set for a more direct contribution to what was revealed in chapter 2 to be one of the

overarching goals of this scientific subcommunity: estimating how a specific escape channel for Mars' oxygen changes with varying solar input parameters. This was explored in chapter 7.

Questions to be addressed by this dissertation were outlined toward the end of chapter 2. Answers to these questions are provided below.

- **How well can the energetic plume of escaping planetary ions be seen in MEX IMA data beyond the MPB (i.e., in the magnetosheath and solar wind)?**

  This question can be answered in two parts. First, it was demonstrated in chapter 4 that heavy energetic planetary ions outside of the MPB, moving in the estimated direction of E_{SW}, and increasing in energy as the observation point moves further from the planet, can certainly be found. In other words, individual instances of energetic plume observations can be found that exactly match the phase space characteristics of the plume predicted by models. A second answer to this question would be that this good match between model predictions and MEX IMA data occurs only a fraction of the time. The unfortunately-oriented field of view, which misses ions moving directly in the E_{SW} direction when the IMF is in the ecliptic plane, are very likely a main reason for this. In short, the plume can be seen by IMA, and it can be seen well enough to help expand understanding of how the plume varies with drivers, but given the instrumental limitations, IMA cannot be expected to see the plume well enough for MEX data to be a primary basis of estimates about the total magnitude of plume escape fluxes.

- **What are the statistics of energetic planetary ions outside of the MPB as a function of solar wind motional electric field?**

  The ease with which the energetic plume can be seen statistically in ion data is directly

dependent upon the accuracy of the estimate used for the direction of E_{SW}. Figure 4.5 showed almost no discernable plume signature. After data is downselected to include only times when the clock angle of the solar wind is relatively steady over the course of at least four hours, the remaining estimates for E_{SW} are good enough to see the expected asymmetry in heavy ion data with energies typical of the plume (e.g. Figs 5.8 and 5.9). Further improvements on the estimated direction of E_{SW}, obtained in chapter 6 by using MF-MHD to estimate an average extent of weathervaning, result in a much clearer organization around E_{SW} (e.g. Fig. 6.9). Analysis of Fig. 6.10 suggests that plume-like ion beams are seen at last ~45-50% of the time when MEX is in the $+E_{SW}$ quadrant. This may be considered to be a lower limit, given that, despite multiple rounds of improvements upon the proxy for E_{SW}, the estimates of E_{SW} used to generate these $+E_{SW}$ quadrants remain imperfect. Ion observations taken when magnetic field information upstream of Mars is available would likely yield E_{SW} estimates accurate enough that plume-like ion beams could be seen in the $+E_{SW}$ quadrant over half the time.

- **How can the assumed IMF proxy at Mars be improved?**

  The estimate for the clock angle of the upstream IMF (and hence the estimate for the clock angle of E_{SW}) can be improved by assuming that draped field lines that have been convected downward to altitudes of substantial planetary ion density will experience "weathervaning," and by using models to estimate the extent to which this bending of field lines occurs. Further improvements to estimates of upstream IMF using ~400km

altitude magnetic field observations might be made following an improved understanding of when and how crustal magnetic fields influence these measurements.

- **What changes to the planetary ion plume statistical characteristics are revealed by using an improved IMF proxy?**

  Much of this was addressed in the answer to the previous question. Use of an improved proxy results in enhanced organization around E_{SW}. Maps of near-Mars space made with the better proxies reveal large fluxes of heavy 2-15 keV ions to be concentrated in the E_{SW} direction on the dayside and near the terminator plane. It can also be noted that the unexpected result of the $-E_{SW}$ hemisphere seeing greater quantities of heavy energetic ions than the $+E_{SW}$ hemisphere when MEX was on the nightside (Figs. 5.6 and 5.7 and top-right panel of Fig. 6.9) seems to become much less pronounced when using a more accurate proxy (Fig. 6.9). The improved IMF proxy was then used to examine variations in the presence of energetic plume ions for different conditions, and the initial results suggest the plume may be enhanced during periods of high solar wind pressure, as seen in Fig. 7.2.

9.2 The Adaptive Mesh Particle Simulator: A Gold Mine of Future Work

The Adaptive Mesh Particle Simulator (AMPS) developed by Valeriy Tenishev is a highly adaptable model capable of calculating the trajectories of particles within background fields fed into AMPS and also capable of modeling the effects of the collisions of these particles with a background medium and with each other. For a detailed description of AMPS, see *Tenishev et al.* [2008]. AMPS has previously been adapted to model trajectories of neutral particles and the

formation of Mars' hot oxygen corona (*Lee et al.*, 2015). Once AMPS is adapted to model Mars ions, a variety of exciting studies will be possible.

The altitude of origin of most escaping ions remains unknown. Comparisons of the escape rates of O^+ and O_2^+ can give some partial understanding of source altitude, with enhanced O_2^+ fluxes for given solar conditions used as an indication that more of the escape may originate at lower altitudes for these conditions (*Brecht and Ledvina*, 2014), but a large amount of uncertainty remains surrounding source altitude. This uncertainty can be demonstrated with a side by side comparison of *Brecht and Ledvina* [2014] and *Curry et al*. [2013b] Both modeling papers test out the importance of inclusion of the hot oxygen corona as a source population for escaping oxygen ions, and with very different results. *Curry et al*. [2013b] found that inclusion of the hot oxygen corona enhanced escape fluxes by roughly a factor of two. In contrast, *Brecht and Ledvina* [2014] saw almost no change in O^+ escape rates after inclusion of the hot O corona. Later, *C. Dong et al*. [2015] indicate that, not only is the inclusion of a hot O corona important, but that using a seasonally-correct (EUV-dependent) hot O corona is important. As a model capable of both keeping track of ion source locations and examining the transition region between the collisional atmosphere and the collisionless exosphere, AMPS is extremely well suited to analyses of where escaping planetary ions seem to originate.

Given that the investigation of phenomena involving collisions is a strength of AMPS, a study of sputtering could also prove fruitful. For instance, AMPS may be able to determine the number of

atmospheric particles brought to escape energy for typical precipitating particles of various energies.

Another way in which in which AMPS' collisional capabilities may be utilized is to investigate recombination rates. After cross sections for recombination rates are fed to AMPS, the simulation domain could be hit with a solar wind pressure pulse that would compress the Martian ionosphere. Would the increased electron densities resulting from this compression be enough to significantly increase recombination rates and then reduce electron densities, as was reported in Venus simulations (*Jin et al*., 2008).

9.3 More Future Work (And Closing Remarks)

As available observations increase, leading to corresponding increases in understanding of how ion fluxes vary with angle with respect to E_{SW}, it will become increasingly easy to improve observational estimates of total present-day ion escape by incorporating knowledge gained concerning clock-angle-dependent escape fluxes. For example, if an escape rate estimate were made using only observations for which the data could be transformed into MSE coordinates, then rather than simply multiplying ion-per-area fluxes by a cylindrically symmetric area, fluxes specific to a particular angle in MSE coordinates would be used. Similar considerations also have potential use for cases for which there are very few observations. Consider as an example the passage of a CME by Mars. Observations of CMEs are sufficiently rare that decades of CME observations may be gathered without ever achieving reasonable statistical data coverage at all MSE clock angles. If a method of weighting escape fluxes by clock angle based on quiet times were available, this could be used to achieve an approximation of total escape rates during a

CME of a given magnitude even if only a few spacecraft passes worth of data were present.

With a paper concerning the weathervaning and the improved IMF proxy so recently written, it is difficult not to think about lines of research related to the behavior of "draped" field lines around an ionosphere (with or without the presence of crustal fields). Is the description of weathervaning as primarily an effect of mass-loading slowing the center of field lines? Or should weathervaning be thought of more in terms of the field aligning itself anti-subsolarward according to the ionospheric flow patterns? What if crustal fields influenced the results more than we recognize, and the consideration of weathervaning-type field line configurations was successful in generating an improved IMF proxy not only because many of the MGS observations at 400km altitude were weathervaned draped IMF, but also because, even when the observations were actually of crustal fields, these fields also have a tendency to partially align themselves in an anti-subsolarward direction? And what of the hemispheric asymmetry of weathervaning? Might there be an associated asymmetry in the location of the MPB? These are questions for the community of researchers that I feel blessed to have been a part of.

References

Acuña, M. H., Connerney, J. E. P., Wasilewski, P., Lin, R. P., Mitchell, D., Anderson, K. a., … Ness, N. F. (2001). Magnetic field of Mars: Summary of results from the aerobraking and mapping orbits. *Journal of Geophysical Research*, *106*(E10), 23403. http://doi.org/10.1029/2000JE001404

Appleton, E.V. (1933), Fine structure of the ionosphere, *Nature* 131, 872-873, doi: 10.1038/131872a0

Baker, V. R., and D. J. Milton, Erosion by catastrophic floods on Mars and Earth, *Icarus*, **23**, 27–41, 1974.

Barabash, S., Dubinin, E., Pisarenko, N., Lundin, R., and Russell, C. T. (1991), Picked-up protons near Mars – PHOBOS observations, *Geophys. Res. Lett., 18,* 1805–1808.

Barabash, S., et al., (2004), The analyser of space plasmas and energetic atoms (ASPERA-3) for the European Mars Express mission, in *Mars Express: A European Mission to the Red Planet*, Wilson, A. (Ed.), European Space Agency, ESTEC, Noordwijk, The Netherlands, pp. 121–139. ESA publication SP-1240.

Barabash, S., et al. (2006), The Analyzer of Space Plasmas and Energetic Atoms (ASPERA-3) for the Mars Express mission, *Space Sci. Rev., 126*, 113-164.

Barabash, S., A. Fedorov, R. Lundin, and J.-A. Sauvaud (2007), Martian Atmospheric Erosion Rates, *Science, 315*, 501–503, doi:10.1126/ science.1134358.

Bertucci, C., F. Duru, N. Edberg, and M. Fraenz (2011), The Induced Magnetospheres of Mars, Venus, and Titan, in *The Plasma Environment of Venus, Mars, and Titan*, pp. 113–172.

Boesswetter, A., Bagdonat, T., Motschmann, U., Sauer, K. (2004), Plasma boundaries at Mars: A 3-D simulation study, *Ann. Geophys. 22,* 4363–4379.

Bougher, S. W., A. Ridley, D. Pawlowski, J. M. Bell, and S. Nelli (2011), Development and validation of the Ground-to-Exosphere Mars GITM Code: Solar cycle and seasonal variations of the upper atmosphere, in Fourth International Workshop on the Mars Atmosphere: Modeling and Observations, edited by F. Forget and E. Millour, pp. 379–381, NASA, Paris, France.

Bougher, S. W., A. Ridley, D. Pawlowski, J. M. Bell, and S. Nelli (2011), Development and validation of the Ground-to-Exosphere Mars GITM Code: Solar cycle and seasonal variations of the upper atmosphere, in Fourth International Workshop on the Mars Atmosphere:Modeling and Observations, edited by F. Forget and E. Millour, pp. 379–381, NASA, Paris, France

Bougher, S., A. Ridley, D. Pawlowski, J. M. Bell, and S. Nelli (2011), Development and validation of the Ground-to-Exosphere Mars GITM Code: Solar cycle and seasonal variations of the upper atmosphere, in *Fourth International Workshop on the Mars Atmosphere: Modeling and Observations*, pp., 379-381, NASA, Paris, France.

Bougher, S., D. Pawlowski, J. Bell, S. Nelli, T. McDunn, J. Murphy, M. Chizek, and A. Ridley (2015), Mars global ionosphere-thermosphere model: Solar cycle, seasonal, and diurnal variations of the Mars upper atmosphere, *J. Geophys. Res. Planets*, *120*, 311–342, doi:10.1002/2014JE004715.

Brain, D. A., F. Bagenal, M. H. Acun, J. E. P. Connerney, and D. H. Crider (2002), Observations of low-frequency electromagnetic plasma waves upstream from the Martian shock, *Journal of Geophysical Research*, *107*.

Brain, D. A., A. H. Baker, J. Briggs, J. P. Eastwood, J. S. Halekas, *and* T.-D. Phan *(2010*a*)*, Episodic detachment of Martian crustal magnetic fields leading to bulk atmospheric plasma escape, *Geophys. Res. Lett., 37, L14108, doi:*10.1029/2010GL043916.

Brain, D. A., et al. (2015), The spatial distribution of planetary ion fluxes near Mars observed by MAVEN, Geophys. Res. Lett., 42, doi:10.1002/2015GL065293.

Brain, D., S. Barabash, S. W. Bougher, F. Duru, B. Jakosky, R. Modolo, Chapter 15: Solar Wind Interactions and Escape Processes, in *The Atmosphere and Climate of Mars*, ed. B. Haberle, M. Smith, T. Clancy, F. Forget, R. Zurek, Cambridge UniversityPress, (2017), doi:10.1017/9781107016187.

Brain, D. A., D. L. Mitchell, and J. S. Halekas (2006), The magnetic field draping direction at Mars from April 1999 through August 2004, *Icarus, 182*, 464-473, doi: 10.1016/j.icarus.2005.09.023.

Brain, D. A., et al. (2005). Variability of the altitude of the Martian sheath. *Geophysical Research Letters*, *32*(18), L18203. http://doi.org/10.1029/2005GL023126

Brain, D., Barabash, S., Boesswetter, A., Bougher, S., Brecht, S., Chanteur, G., … Terada, N. (2010). A comparison of global models for the solar wind interaction with Mars. *Icarus*. http://doi.org/10.1016/j.icarus.2009.06.030

Brain, D. A., J. S. Halekas, L. M. Peticolas, R. P. Lin, J. G. Luhmann, D. L. Mitchell, G. T. Delory, S. W. Bougher, M. H. Acuña, and H. Rème (2006b), On the origin of aurorae on Mars, Geophys. Res. Lett., 33, L01201, doi:10.1029/2005GL024782.

Brecht, S. H., *and* S. A. Ledvina *(2012),* Control of ion loss rates from Mars during solar minimum, *Earth Planets Space, 64,* 165*–178.*

Brecht, S. H., and S. A. Ledvina (2014), The role of the Martian crustal magnetic fields in controlling ionospheric loss, Geophys. Res. Lett., 41, 5340–5346, doi:10.1002/2014GL060841.

Briggs, J. A., D. A. Brain, M. L. Cartwright, J. P. Eastwood, and J. S. Halekas (2011), A statistical study of flux ropes in the Martian magnetosphere, Planet. Space Sci., 59, 1498–1505, doi:10.1016/j.pss.2011.06.010.

Cain, J. C., B. B. Ferguson, and D. Mozzoni (2003), An n = 90 internal potential function of the Martian crustal magnetic field, *J. Geophys. Res*., 108(E2), 5008, doi:10.1029/2000JE001487.

Carlsson, E., D. Brain, J. Luhmann, S. Barabash, A. Grigoriev, H. Nilsson, and R. Lundin (2008), Influence of IMF draping direction and crustal magnetic field location on Martian ion beams, *Planet. Space Sci., 56*, 861-867, doi: 10.1016/j.pss.2007.12.016.

Carr, M. H. and Head III, J. W. (2003) Oceans of Mars: An assessment of the observational evidence and possible fate. *Journal of Geophysical Research*, v. 108(E5), 5042, doi: 10.1029/2002JE001963, 2003

Chaffin, M. S., J.-Y. Chaufray, I. Stewart, F. Montmessin, N. M. Schneider, and J.-L. Bertaux (2014), Unexpected variability of Martian hydrogen escape, Geophys. Res. Lett., 41, 314–320, doi:10.1002/2013GL058578.

Chaffin, M. S., J. Y. Chaufray, J. Deighan, N. M. Schneider, W. E. McClintock, A. I. F. Stewart, E. Thiemann, J. T. Clarke, G. M. Holsclaw, S. K. Jain, et al. (2015), Three-dimensional structure in the Mars H corona revealed by IUVS on MAVEN, Geophys. Res. Lett., 42, 9001–9008, doi:10.1002/2015GL065287.

Chassefiere, E., and Leblanc, F. (2004) Mars atmospheric escape and evolution: Interaction with the solar wind, *Planet. Space Sci.*, **52,** 1039–1058

Collinson, G., et al. (2015), Electric Mars: The first direct measurement of an upper limit for the Martian "polar wind" electric potential, Geophys. Res. Lett., 42, doi:10.1002/2015GL065084.

Cowan, J. J., A'Hearn, M. F. (1979), Vaporization of comet nuclei – Light curves and life times, *Moon and the Planets*, vol.21, pp. 155-171

Crider, D., Brain, D. A., Acun˜a, M., Vignes, D., Mazelle, C., and Bertucci, C.: 2004, Mars Global Surveyor Observations of Magnetic Field Draping Around Mars, *Space Sci. Rev.* 111, 203.

Crider, D. H., et. al., *(*2003*),* A proxy for determining solar wind dynamic pressure at Mars using Mars Global Surveyor data, *J. Geophys. Res*., 108, *1461, doi:*10.1029/2003JA009875, A12.

Curry, S. M., M. W. Liemohn, X. Fang, Y. Ma, A. F. Nagy, and J. Espley (2013a), The influence of production mechanisms on pickup ion loss at Mars, *J. Geophys. Res. Space Physics, 118,* doi: 10.1029/2012JA017665.

Curry, S. M., M. Liemohn, X. Fang, D. Brain, and Y. Ma (2013b), Simulated kinetic effects of the corona and solar cycle on high altitude ion transport at Mars, J. Geophys. Res. Space Physics, 118, 3700–3711, doi:10.1002/jgra.50358.

Curry, S. M., J. G. Luhmann, Y. J. Ma, C. F. Dong, D. Brain, F. Leblanc, R. Modolo, Y. Dong, J. McFadden, J. Halekas, et al. (2015), Response of Mars O^+ pickup ions to the 8 March 2015 ICME: Inferences from MAVEN data-based models, Geophys. Res. Lett., 42, 9095–9102, doi:10.1002/2015GL065304.

Dieval, C., D. D. Morgan, F. Nemec, and D. A. Gurnett (2014), MARSIS observations of the Martian nightside ionosphere dependence on solar wind conditions, *J. Geophys. Res. Space Physics*, *119*, 2077-2093, doi: 10.1002/2014JA019788.

Dohm, J. M. et al (2009), GRS evidence and the possibility of paleooceans on Mars, *Planetary and Space Science*, volume 57, issues 5-6, pp 664-684, doi:10.1016/j.pss.2008.10.008

Donahue, T. M., and C. T. Russell (n.d.), The Venus Atmosphere and Ionosphere and their interaction with the Solar Wind: an Overview. 1997. [online] Available from: https://docs.google.com/a/umich.edu/viewer?a=v&q=cache:HdD1ycBh9mYJ:www-spc.igpp.ucla.edu/personnel/russell/papers/Venus_Overview.pdf+&hl=en&gl=us&pid=bl&srcid=ADGEESjU87EHMKcqEDlMj0PzXLvpkaGnS2GFKDrEE5B38o4rpC3xaNK9NQF4-eoV6-E2L7iIPqV-s7qnzH40Eo2GIHX-WPDlYF_ZNEJdNoH8KvRJnng1uFwgOfkBN3xSDIj9mQ2VUGJH&sig=AHIEtbT1MxxbO6pW8hGkuA5bkab7Bxfu5w

Dong, C., Lingam, M., Ma, Y., Cohen, O. (2017), Is Proxima Centauri b Habitable? A Study of Atmospheric Loss, Astrophysical Journal, Vol.837, 2, doi: 10.3847/2041-8213/aa6438

Dong, C. F., Y. Ma, S. W. Bougher, et al. Multifluid MHD Study of the Solar Wind Interaction with Mars' Upper Atmosphere During the 2015 March 8th ICME Event, Geophys. Res. Lett., 42, 9103-9112, doi:10.1002/2015GL065944, (2015).

Dong, C., S. W. Bougher, Y. Ma, G. Toth, Y. Lee, A. F. Nagy, V. Tenishev, D. J. Pawlowski, M. R. Combi, and D. Najib (2015), Solar wind interaction with the Martian upper atmosphere: Crustal field orientation, solar cycle, and seasonal variations, J. Geophys. Res. Space Physics, 120, 7857–7872, doi:10.1002/2015JA020990.

Dong, C., S. W. Bougher, Y. Ma, G. Toth, A. F. Nagy, and D. Najib (2014), Solar wind interaction with Mars upper atmosphere: Results from the one-way coupling between the multifluid MHD model and the MTGCM model, Geophys. Res. Lett., 41, 2708–2715, doi:10.1002/2014GL059515.

Dong, Y., X. Fang, D. A. Brain, J. P. McFadden, J. S. Halekas, J. E. Connerney, S. M. Curry, Y. Harada, J. G. Luhmann, and B. M. Jakosky (2015), Strong plume fluxes at Mars observed by MAVEN: An important planetary ion escape channel,Geophys. Res. Lett.,42 , doi:10.1002/ 2015GL065346.

Dong, Y., X. Fang, D. A. Brain, J. P. McFadden, J. S. Halekas, J. E. P. Connerney, F. Eparvier, L. Andersson, D. Mitchell, and B. M. Jakosky (2017), Seasonal variability of Martian ion

escape through the plume and tail from MAVEN observations, J. Geophys. Res. Space Physics, 122, doi:10.1002/2016JA023517.

Dubinin, E., Fraenz, M., Woch, J., Zhang, T.L., Wei, Y., Fedorov, S., Barabash, S., Lundin, R., (2013), Toroidal and poloidal magnetic fields at Venus Express observations, *Planetary and Space Science*, vol.87, pp.19-29, doi: 10.1016/j.pss.2012.12.003

Dubinin, E. M., K. Sauer, R. Lundin, K. Baumgärtel, and A. Bogdanov (1996), Structuring of the transition region (plasma mantle) of the Martian magnetosphere, *Geophys. Res. Lett., 23*, 785, 1996.

Dubinin, E., Fränz, M., Woch, J., Roussos, E., Barabash, S., Lundin, R., … Acuña, M. (2006). Plasma Morphology at Mars. Aspera-3 Observations. *Space Science Reviews*, *126*(1-4), 209–238. doi:10.1007/s11214-006-9039-4

Dubinin, E., M. Fraenz, A. Fedorov, R. Lundin, N. Edberg, F. Duru, and O. Vaisberg (2011), Ion energization and escape on Mars and Venus, *Space Sci. Rev., 162*, 173-211, doi: 10.1007/s11214-011-9831-7.

Dubinin, E., M. Fränz, J. Woch, E. Roussos, S. Barabash, R. Lundin, J. D. Winningham, R. A. Frahm, and M. Acuña (2008), Plasma morphology at Mars: ASPERA-3 observations, *Space Sci., Rev., 126*, 209-238, doi: 10.1007/s11214-006-9039-4.

Edberg, N. J. T, et al. (2009), Rosetta and Mars Express observations of the influence of high solar wind pressure on the Martian plasma environment, *Ann. Geophys., 27*, 4533–4545, doi: 10.5194/angeo-27-4533-2009.

Edberg, N. J. T., D. A. Brain, M. Lester, S. W. H. Cowley, R. Modolo, M. Fränz, and S. Barabash (2009), Plasma boundary variability at Mars as observed by Mars Global Surveyor and Mars Express, *Ann. Geophys*., 27, 3537–3550, doi:10.5194/angeo-27-3537-2009.

Fang, X., M. W. Liemohn, A. F. Nagy, Y. Ma, D. L. De Zeeuw, J. U. Kozyra, and T. Zurbuchen (2008), Pickup oxygen ion distribution around Mars, *J. Geophys. Res., 113*, A02210, doi: 10.1029/2007JA012736.

Fang, X., M. W. Liemohn, A. F. Nagy, J. G. Luhmann, and Y. Ma (2010), On the effect of the Martian crustal magnetic field on atmospheric erosion, Icarus, 206, 130, doi:10.1016/j.icarus.2009.01.012.

Fedorov, A., et al. (2006), Structure of the Martian wake, *Icarus, 182*, 329– 336, doi:10.1016/j.icarus.2005.09.021.

Fedorov, a., Ferrier, C., Sauvaud, J. a., Barabash, S., Zhang, T. L., Mazelle, C., … Bochsler, P. (2008). Comparative analysis of Venus and Mars magnetotails. *Planetary and Space Science*, *56*(6), 812–817. doi:10.1016/j.pss.2007.12.012

Fraenz, M., E. Dubinin, D. Andrews, S. Barabash, H. Nilsson, A. Fedorov (2015), Cold ion escape from the Martian ionosphere, *Planet. Space Sci., 119*, 92-102, doi: 10.1016/j.pss.2015.07.012

Frahm, R. A., J. R. Sharber, J. D. Winningham, S. J. Jeffers, R. Link, M. W. Liemohn, J. U. Kozyra, A. J. Coates, D. R. Linder, S. Barabash, R. Lundin, and A. Fedorov, Estimation of escape of photoelectrons from Mars in 2004 liberated by the ionization of carbon dioxide and atomic oxygen, *Icarus*, 206, 50, doi:10.1016/j.icarus.2009.03.024, 2010.

Frey, H. V. (2006). Impact constraints on, and a chronology for, major events in early Mars history. *Journal of Geophysical Research*, *111*(E8), E08S91. doi:10.1029/2005JE002449

Halekas, *J.S.*, D. A. Brain, S. Ruhunusiri, J. P. McFadden, D. L. Mitchell, C. Mazelle, J. E. P. Connerney, Y. Harada, T. Hara, J. R. Espley, G.A. DiBraccio, B. M. Jakosky, Plasma clouds and snowplows: Bulk plasma escape from Mars observed by MAVEN, *Geophysical Research Letters, 2016, 43, 4, 1426*

Halekas, J. S., et al. (2017), Structure, dynamics, and seasonal variability of the Mars-solar wind interaction: MAVEN Solar Wind Ion Analyzer in-flight performance and science results, *J. Geophys. Res. Space Physics*, 122, 547–578, doi:10.1002/2016JA023167.

Halekas, J. S., Brain, D. A., Lillis, R. J., Fillingim, M. O., Mitchell, D. L., & Lin, R. P. (2006). Current sheets at low altitudes in the Martian magnetotail. *Geophysical Research Letters*. http://doi.org/10.1029/2006GL026229

Hara, T., et al. *(*2017*)*, MAVEN observations on a hemispheric asymmetry of precipitating ions toward the Martian upper atmosphere according to the upstream solar wind electric field, *J. Geophys. Res. Space Physics*, 122, 1083–1101, *doi:*10.1002/2016JA023348.

Harnett, E. M., *and* R. M. Winglee (2006), Three-dimensional multifluid simulations of ionospheric loss at Mars from nominal solar wind conditions to magnetic cloud events, *J. Geophys. Res., 111,* A09213, doi: 10.1029/2006JA011724.

Hoilijoki, S., V. M. Souza, B. M. Walsh, P. Janhunen, and M. Palmroth (2014), Magnetopause reconnection and energy conversion as influenced by the dipole tilt and the IMF *Bx*, J. Geophys. Res. Space Physics, 119, 4484–4494, doi:10.1002/2013JA019693.

Ivanov, M. A. and J. W. Head, III (2001) Chryse Planitia, Mars: Topographic configuration, outflow channel continuity and sequence, and tests for hypothesized ancient bodies of water using Mars Orbiter Laser Altimeter (MOLA) data, *Journal of Geophysical Research,*vol. 106, p. 3275-3295.

Jakosky et al., (2017), Mars' atmospheric history derived from upper-atmosphere measurements of $^{38}Ar/^{36}Ar$, *Science*, vol. 355, iss. 6332, pp. 1408-1410, DOI: 10.1126/science.aai7721

Jarvinen, R., Brain, D. A., & Luhmann, J. G. (2016). Dynamics of planetary ions in the induced magnetospheres of Venus and Mars. *Planetary and Space Science*. http://doi.org/10.1016/j.pss.2015.08.012

Jin, H., K. Maezawa, and T. Mukai (2008), The critical solar wind pressure for IMF penetration into the Venus ionosphere, *Journal of Geophysical Research*, *113*(A2), A02309, doi:10.1029/2007JA012725. [online] Available from: http://doi.wiley.com/10.1029/2007JA012725 (Accessed 23 April 2013)

Johnson, R. E., D. Schnellenberger, and M. C. Wong (2000), The sputtering of an oxygen thermosphere by energetic O^+, J. Geophys. Res., 105(E1), 1659–1670, doi:10.1029/1999JE001058.

Johnson, R. E., and J. G. Luhmann (1998), Sputter contribution to the atmospheric corona on Mars, J. Geophys. Res., 103(E2), 3649–3653, doi:10.1029/97JE03266.

Johnson, B. C., Liemohn, M. W., Fränz, M., Ramstad, R., Stenberg Wieser, G., & Nilsson, H. (2017). Influence of the interplanetary convective electric field on the distribution of heavy pickup ions around Mars. Journal of Geophysical Research: Space Physics, 122. https://doi.org/10.1002/2017JA024463

Kallio, E., H. Koskinen, S. Barabash, C. M. C. Nairn, and K. Schwingenschuh (1995), Oxygen outflow in the Martian magnetotail, *Geophys. Res. Lett.*, *22*, 2449–2452.

Kallio, E., and H. Koskinen (1999), A test particle simulation of the motion of oxygen ions and the solar wind protons, *J. Geophys. Res.*, *104*, 557–579.*333333*

Kallio, E., A. Fedorov, E. Budnik, S. Barabash, R. Jarvinen, and P. Janhunen (2008), On the properties of O^+ and O_2^+ ions in a hybrid model and in Mars Express IMA/ASPERA-3 data: A case study, Planet. Space Sci., 56, 1204–1213.

Kallio, E., et al. (2006b), Energisation of O+ and O2+ ions at Mars: An analysis of a 3-D quasi-neutral hybrid model simulation, *Space Sci. Rev., 126*, 39-62.

Lammer, H., J. F. Kasting, E. Chassefière, R. E. Johnson, Y. N. Kulikov, and F. Tian (2009), Atmospheric Escape and Evolution of Terrestrial Planets and Satellites, *Comparative Aeronomy*, *2*, 399, doi:10.1007/978-0-387-87825-6_11.

Law, C. C., & Cloutier, P. A. (1995). Observations of magnetic structure at the dayside ionopause of Venus. *journal of geophysical research*, *100981*(1), 973–23. http://doi.org/10.1029/95JA02756

Ledvina, S.A., Luhmann, J.G., Brecht, S.H., Cravens, T.E. (2004), Titan's induced magnetosphere, *Advances in Space Research,* vol.33 issue 11, pp. 2092-2102, doi: 10.1016/j.asr.2003.07.056

Lee, Y., M. R. Combi, V. Tenishev, S. W. Bougher, and R. J. Lillis (2015), Hot oxygen corona at Mars and the photochemical escape of oxygen - Improved description of the thermosphere, ionosphere and exosphere}, *J. Geophys. Res. Planets*, 120, 1880-1892, doi:10.1002/2015JE004890.

Liemohn, M. W., Y. Ma, R. A. Frahm, X. Fang, J. U. Kozyra, A. F. Nagy, J. D. Winningham, J. R. Sharber, S. Barabash, and R. Lundin, Mars global MHD predictions of magnetic connectivity between the dayside ionosphere and the magnetospheric flanks, *Space Sci. Rev*., *126*, 63-76, 2006

Liemohn, M. W., et al. (2014), Mars Express observations of high altitude planetary ion beams and their relation to the "energetic plume" loss channel, *J. Geophys. Res.*, 119, 9702–9713, doi:10.1002/2014JA019994.

Liemohn, M. W., Ma, Y., Frahm, R. a., Fang, X., Kozyra, J. U., Nagy, A. F., … Lundin, R. (2007). Mars Global MHD Predictions of Magnetic Connectivity Between the Dayside Ionosphere and the Magnetospheric Flanks. *Space Science Reviews*, *126*(1-4), 63–76. doi:10.1007/s11214-006-9116-8

Liemohn, M. W., S. M. Curry, X. Fang, and Y. Ma (2013), Comparison of high-altitude production and ionospheric outflow contributions to O^+ loss at Mars, *J. Geophys. Res Space Physics*, *118*, 4093-4107, doi: 10.1002/jgra.50388.

Liemohn et al. (2017), Ionospheric control of the dawn-dusk asymmetry of the Mars magnetotail current sheet. *J. Geophys. Res. Space Physics*, accepted

Lillis, R. J., et al. (2017), Photochemical escape of oxygen from Mars: First results from MAVEN in situ data, J. Geophys. Res. Space Physics, 122, 3815–3836, doi:10.1002/2016JA023525.

Liu, S. C. and Donahue, T. M. (1976), The Regulation of Hydrogen and Oxygen Escape from Mars, *Icarus*, 28, 231-246, doi: 10.1016/0019-1035(76)90035-X

Lucchitta, B. K., H. M. Ferguson, and C. Summers, Sedimentary deposits in the northern lowland plains, Mars, Proc. Lunar Planet. Sci. Conf. 17th, Part 1, J. Geophys. Res., **91**, suppl., E166–E174, 1986.

Luhmann, J. G., Ledvina, S.A., Russel, C.T. (2004), Induced Magnetospheres, Advances in Space Research, vol. 33 issue 11, pp. 1905-1912, doi: 10.1016/j.asr.2003.03.031

Luhmann, J. G. (1986), The Solar Wind Interaction with Venus, *Space Science Reviews*, *44*, 241–306.

Luhmann, J. G., and K. Schwingenschuh (1990), A model of the energetic ion environment of Mars, J. Geophys. Res., 95, 939–945, doi:10.1029/JA095iA02p00939.

Luhmann, J. G., Evolutionary impact of sputtering of the Martian atmosphere by O^+ pickup ions, *Geophysical Research Letters*, doi:10.1029/92GL02485

Luhmann, J. G., J. L. Phillips, and C. T. Russell, Studies of the configuration of the Venus ionospheric magnetic field, *Adv. Space Res*., l, 101, 1987.

Luhmann, J. G. (1988). A THREE-DIMENSIONAL DIFFUSION/CONVECTION MODEL OF THE LARGE SCALE MAGNETIC FIELD IN THE VENUS IONOSPHERE. *JOURNAL*

OF GEOPHYSICAL RESEARCH, *93*(1), 5909–5914. http://doi.org/10.1029/JA093iA06p05909

Luhmann, J. G., and K. Schwingenschuh (1990), A model of the energetic ion environment of Mars, *J. Geophys. Res.*, *95*, 939–945.

Luhmann, J. G., Y.-J. Ma, D. A. Brain, D. Ulusen, R. J. Lillis, J. S. Halekas, and J. R. Espley (2015), Solar wind interaction effects on the magnetic fields around Mars: Consequences for interplanetary and crustal field measurements, *Planet. Space Sci.*, *117*, 15-23, doi: 10.1016/j.pss.2015.05.004.

Lundin, R., Barabash, S., Holmström, M., Nilsson, H., Yamauchi, M., Fraenz, M., & Dubinin, E. M. (2008). A comet-like escape of ionospheric plasma from Mars. *Geophysical Research Letters*, *35*(18), L18203. doi:10.1029/2008GL034811

Lundin, R., and E. M. Dubinin (1992), Phobos-2 results on the ionospheric plasma escape from Mars, *Adv. Space Res*., 12, 255– 263, doi:10.1016/0273-1177(92)90338-X.

Lundin, R., Barabash, S., Yamauchi, M., Nilsson, H., & Brain, D. (2011). On the relation between plasma escape and the Martian crustal magnetic field. *Geophysical Research Letters*, *38*(2), L02102. doi:10.1029/2010GL046019

Lundin, R., et al. (2004), Solar wind-induced atmospheric erosion at Mars: First results from ASPREA-3 on Mars Express, *Science, 305*, 1993-1936.

Ma, Y. J., et al. (2009), Time-dependent global MHD simulations of Cassini T32 flyby: From magnetosphere to magnetosheath, J. Geophys. Res., 114, A03204, doi:10.1029/2008JA013676.

Malin, M. C. and K.S. Edgett, Oceans or seas in the martian northern lowlands: High resolution imaging tests of proposed coastlines, *Geophysical Research Letters*, v. 26, p. 3049-3052, 1999, doi: 10.1029/1999GL002342

Martinecz, C. et al. (2008), Location of the bow shock and ion composition boundaries at Venus—initial determinations from Venus Express ASPERA-4, *Planetary and Space Science*, *56*(6), 780–784, doi:10.1016/j.pss.2007.07.007. [online] Available from: http://linkinghub.elsevier.com/retrieve/pii/S0032063307003765 (Accessed 23 April 2013)

McCauley, J. F., M. H. Carr, J. A. Cutts, W. K. Hartmann, H. Masursky, D. J. Milton, R. P. Sharp, and D. E. Wilhelms, Preliminary Mariner 9 report on the geology of Mars, *Icarus*, **17**, 289–327, 1972.

McElroy, M. B., Donahue, T. M. (1972). Stability of the Martian atmosphere. *Science*, 177, 986-988.

McElroy, M. B. (1972), Mars: An evolving atmosphere, *Science*, 175, 443-445

Mitchell, D. L., R. P. Lin, C. Mazelle, H. Rème, P. A. Cloutier, J. E. P. Connerney, M. H. Acuña, and N. F. Ness *(*2001*),* Probing Mars' crustal magnetic field and ionosphere with the MGS Electron Reflectometer, J. *Geophys. Res.,* 106*(*E10*),* 23419–23427, doi*:*10.1029/2000JE001435.

Modolo, R., Chanteur, G. M., & Dubinin, E. (2012). Dynamic martian magnetosphere: Transient twist induced by a rotation of the IMF. *Geophysical Research Letters, 39*(1) doi:http://dx.doi.org.proxy.lib.umich.edu/10.1029/2011GL049895

Modolo, R., G. M. Chanteur, E. Dubinin, and A. P. Matthews (2005), Influence of the solar EUV flux on the Martian plasma environment, *Ann. Geophys., 23*, 433-444.

Mustard, J. F. et al., (2008), Hydrated silicate minerals on Mars observed by the Mars Reconnaissance Orbiter CRISM instrument, *Nature*, 454, 305–309 (17 July 2008) doi:10.1038/nature07097

Mustard, J. F. et al. (2012), Sequestration of volatiles in the martian crust through hydrated minerals: a significant planetary reservoir of water. *43rd Lunar and Planetary Science Conference*

Nagy, a. F., Winterhalter, D., Sauer, K., Cravens, T. E., Brecht, S., Mazelle, C., … Trotignon, J. G. (2004). The plasma environment of Mars. *Space Science Reviews*, *111*(1–2), 33–114. http://doi.org/10.1023/B:SPAC.0000032718.47512.92

Najib, D., A. F. Nagy, G. Toth, and Y. Ma (2011), Three-dimensional, multifluid, high spatial resolution mhd model studies of the solar wind interaction with mars, *J. Geophys. Res.*, 116(A5), doi:10.1029/2010ja016272.

Nilsson, H., N. J. T. Edberg, G. Stenberg, S. Barabash, M. Holmstrm, Y. Futaana, R. Lundin, and A. Fedorov (2011), Heavy ion escape from Mars, influence from solar wind conditions

and crustal magnetic fields, *Icarus, 215*(2), 475–484, doi: 10.1016/j.icarus.2011.08.003.

Nilsson, H., G. Stenberg, S. Futaana, M. Holmstrom, S. Barabash, R. Lundin, N. Edberg, and A. Fedorov (2012), Ion distributions in the vicinity of Mars: Signatures of heating and acceleration processes, *Earth, Planets and Space, 64*(2), 135–148, doi: 10.5047/eps.2011.04.011.

Nilsson, H., N. J. T. Edberg, G. Stenberg, S. Barabash, M. Holmstrm, Y. Futaana, R. Lundin, and A. Fedorov (2011), Heavy ion escape from Mars, influence from solar wind conditions and crustal magnetic fields, Icarus, 215(2), 475–484, doi: 10.1016/j.icarus.2011.08.003.

Parker, T. J., Gorsline, D. S., Saunders, R. S., Pieri, D. C., Schneeberger, D. M., Coastal Geomorphology of the Martian Northern Plains, *Journal of Geophysical Research*, vol. 98, no.E6, pp.11061-11078, doi: 10.1029/93JE00618

Poulet et al. 2005. Phyllosilicates on Mars and implications for an early Martian climate. *Nature.* 438, 623-627, doi:10.1038/nature04274

Rahmati, A., et al. (2017), MAVEN measured oxygen and hydrogen pickup ions: Probing the Martian exosphere and neutral escape, J. Geophys. Res. Space Physics, 122, 3689–3706, doi:10.1002/2016JA023371.

Ramstad, R., S. Barabash, Y. Futaana, H. Nilsson, X.-D. Wang, and M. Holmström (2015), The Martian atmospheric ion escape rate dependence on solar wind and solar EUV conditions: 1. Seven years of Mars Express observations, J. Geophys. Res. Planets, 120, 1298–1309, doi:10.1002/2015JE004816.

Ramstad, R., Barabash, S., Futaana, Y., Yamauchi, M., Nilsson, H., & Holmström, M. (2017). Mars under primordial solar wind conditions: Mars Express observations of the strongest CME detected at Mars under solar cycle #24 and its impact on atmospheric ion escape. Geophysical Research Letters, 44, 10,805 10,811. https://doi.org/10.1002/2017GL075446

Russell, C. T. (1979), The Interaction of The Solar Wind With Mars, Venus and Mercury, , 209–247.

Szego, K., Harri, A-M., Blanc, M (2011), The plasma environment of Venus, Bars, and Titan, an introduction, *Space Sci Rev.*, 162:1-4, doi:10.1007/s11214-011-9844-2

Squyres, S. W., Grotzinger, J. P. (2004), In Situ Evidence for an Ancient Aqueous Environment at Meridiani Planum, Mars. *Science, Vol. 306, Issue 5702, pp. 1709-1714, doi:* 10.1126/science.1104559

Tenishev, V., Combi, M., Davidsson, B. (2008), A Global Kinetic Model for Cometary Comae: The Evolution of the Coma of the Rosetta Target Comet Churyumov-Gerasimenko throughout the Mission, The Astrophysical Journal, vol.685, doi: 10.1086/590376

Trotignon, J. G., E. Dubinin, R. Grard, S. Barabash, and R. Lundin (1996), Martian planetopause as seen by the plasma wave system onboard Phobos 2, *J. Geophys. Res*., 96(A11), 24,965–24,977, doi:10.1029/96JA01898.

Ulusen, D., Luhmann, J. G., Ma, Y., & Brain, D. A. (2016). Solar control of the Martian magnetic topology: Implications from model-data comparisons. *Planetary and Space Science*. http://doi.org/10.1016/j.pss.2016.01.007

Vennerstrom, S., N. Olsen, M. Purucker, M. H. Acun˜a, and J. C. Cain, The magnetic field in the pile-up region at Mars, and its variationwith the solar wind, *Geophys. Res. Lett.*, *30*(7), 1369, doi:10.1029/2003GL016883, 2003.

Vignes, D., Mazelle, C., Rme, H., Acufia, M. H., Connerney, J. E. P., Mitchell, D. L., … Univer-, R. (2000). shapes of the Bow Shock and the Magnetic Pile-up Boundary from the observations of the MAG / ER experiment onboard Mars Global Surveyor. *Geophysical Research Letters*, *27*(1), 49–52.

Vignes, D., M. H. Acuña, J. E. P. Connerney, D. H. Crider, H. Reme, *and* C. Mazelle, Factors controlling the location of the Bow Shock at Mars, *Geophys. Res. Lett.,* 29*(*9*),* doi*:*10.1029/2001GL014513, 2002.

Wang, X. D., S. Barabash, Y. Futaana, A. Grigoriev, and P. Wurz (2013), Directionality and variability of energetic neutral hydrogen fluxes observed by Mars Express, *J. Geophys. Res. Space Physics*, *118*, 7635-7642, doi: 10.1002/2013JA018876

Wei, H. Y., C. T. Russell, T. L. Zhang, and X. Blanco-Cano (2011), Comparative study of ion cyclotron waves at Mars, Venus and Earth, *Planet. Space Sci*., 59, 1039–1047.

Xu, S., et al. (2017), Martian low-altitude magnetic topology deduced from MAVEN/SWEA observations, J. Geophys. Res. Space Physics, 122, 1831–1852, doi:10.1002/2016JA023467.

Yamauchi, M., Futaana, Y., Fedorov, a., Dubinin, E., Lundin, R., Sauvaud, J. -a., … Luhmann, J. (2007). IMF Direction Derived from Cycloid-Like Ion Distributions Observed by Mars Express. *Space Science Reviews*, *126*(1–4), 239–266. http://doi.org/10.1007/s11214-006-9090-1

Yamauchi, M., Futaana, Y., Fedorov, a., Kallio, E., Frahm, R. a., Lundin, R., … Holmström, M. (2008). Advanced method to derive the IMF direction near Mars from cycloidal proton distributions. *Planetary and Space Science*, *56*(8), 1145–1154. http://doi.org/10.1016/j.pss.2008.02.012

Zhang, T. L. et al. (2008), Induced magnetosphere and its outer boundary at Venus, *Journal of Geophysical Research*, *113*, E00B20, doi:10.1029/2008JE003215. [online] Available from: http://doi.wiley.com/10.1029/2008JE003215